

Spectroscopy on Metal-Halide Lamps under Varying Gravity Conditions

PROEFSCHRIFT

ter verkrijging van de graad van doctor aan de
Technische Universiteit Eindhoven, op gezag van de
Rector Magnificus, prof.dr.ir. C.J. van Duijn, voor een
commissie aangewezen door het College voor
Promoties in het openbaar te verdedigen
op woensdag 22 oktober 2008 om 16.00 uur

door

Adriaan Jan Flikweert

geboren te Gouda

Dit proefschrift is goedgekeurd door de promotoren:

prof.dr.ir. G.M.W. Kroesen
en
prof.dr.ir. M. Haverlag

Copromotor:
dr.ir. W.W. Stoffels

Copyright © 2008 by A.J. Flikweert

This research was financially supported by Senter-Novem (project EDI 03146) and the Dutch Space Research Organisation SRON (project MG-067).

Typeset in L^AT_EX 2_ε using the Winedt editor.
Cover design by A.J. Flikweert. Drawing of setup on the back by P.W.J.H. de Laat.
Printed by PrintPartners Ipskamp, Enschede.

A catalogue record is available from the Eindhoven University of Technology Library

Flikweert, Adriaan Jan

Spectroscopy on Metal-Halide Lamps under Varying Gravity Conditions / door Adriaan Jan Flikweert. – Eindhoven : Technische Universiteit Eindhoven, 2008. – Proefschrift.

ISBN 978-90-386-1395-6

NUR 926

Trefwoorden : plasmafysica / gasontladingen / metaalhalogenidelampen / lichtbronnen / plasmadiagnostiek / spectroscopie / microzwaartekracht / hyperzwaartekracht.

Subject headings : plasma physics / gas discharges / metal-halide lamps / light sources / plasma diagnostics / spectroscopy / micro-gravity / hyper-gravity.

Contents

1	General introduction	1
1.1	Incandescent lamps	2
1.2	Gas discharges	2
1.2.1	Low-pressure discharges	2
1.2.2	High-pressure discharges	4
1.3	Metal-halide lamp	5
1.3.1	The COST reference lamp	5
1.3.2	Axial segregation	6
1.4	Varying gravity conditions	7
1.4.1	Parabolic flights	7
1.4.2	The centrifuge	8
1.5	Diagnostics	10
1.5.1	Laser absorption spectroscopy (1D)	10
1.5.2	Imaging Laser Absorption Spectroscopy (2D)	12
1.5.3	Emission spectroscopy	13
1.6	Thesis outline	13
2	Axial segregation in HID lamps measured by laser absorption spectroscopy	17
2.1	Introduction	18
2.2	Theory	18
2.2.1	Radial segregation	18
2.2.2	Convection and axial segregation	19
2.3	Experimental setup	20
2.4	Results	24
2.4.1	Lateral and radial profile	24
2.4.2	Two-dimensional profile	26
2.4.3	Axial segregation	26
2.5	Conclusions	28

3	Axial segregation in MH lamps under varying gravity conditions	29
3.1	Introduction	30
3.2	Theory	31
3.2.1	Radial segregation	31
3.2.2	Convection and axial segregation	32
3.2.3	Convection time constants	33
3.2.4	Diffusion time constants	35
3.3	Experimental setup	36
3.3.1	The lamp	36
3.3.2	Parabolic flights	37
3.3.3	Laser absorption spectroscopy	37
3.3.4	Integrated light emission setup	39
3.4	Results	39
3.5	Conclusions	43
4	Imaging Laser Absorption Spectroscopy of the MH lamp (1–10<i>g</i>)	45
4.1	Introduction	46
4.2	The centrifuge	48
4.2.1	Acceleration	48
4.2.2	Gondola	51
4.3	Diagnostics	51
4.3.1	Emission spectroscopy	51
4.3.2	Imaging Laser Absorption Spectroscopy	52
4.4	Results	59
4.5	Conclusions	60
5	Semi-empirical model for axial segregation in MH lamps	63
5.1	Introduction	64
5.2	Transport in the MH lamp	66
5.3	Axial segregation	66
5.3.1	Fischer model	67
5.3.2	Temperature influence on atomic Dy density	68
5.3.3	Axial density inhomogeneity parameter	69
5.3.4	Corrected Fischer parameter	72
5.4	Example of fitting parameters for a measurement	73
5.5	Conclusions	74
6	Dy distribution in a MH lamp investigated by ILAS	77
6.1	Introduction	78
6.2	Theory	78
6.2.1	Axial segregation	79
6.2.2	Abel inversion	79

6.2.3	Parameters	80
6.3	Experimental setup	82
6.3.1	Lamps	82
6.3.2	Centrifuge	83
6.3.3	Measurement techniques	84
6.4	Results	85
6.4.1	2D profiles	87
6.4.2	Abel inversion	88
6.4.3	Density inhomogeneity	89
6.4.4	Corrected axial segregation parameter	90
6.5	Conclusions	92
7	Emission spectroscopy for characterizing MH lamps	95
7.1	Introduction	96
7.2	Experimental method	98
7.2.1	Lamps	98
7.2.2	Centrifuge	99
7.2.3	Emission spectroscopy setup	100
7.3	Analysis	102
7.3.1	Axial line intensity inhomogeneity	103
7.3.2	Density calculation using self-reversed lines	103
7.3.3	Temperature calculation using self-reversed lines	103
7.4	Results	106
7.4.1	Lamps with DyI ₃ filling	106
7.4.2	Lamps with CosmoWhite filling	110
7.5	Conclusions	114
8	Comparison between model and experiment	117
8.1	Introduction	118
8.2	Demixing	118
8.3	Model description	120
8.3.1	Energy balance	120
8.3.2	Bulk flow	120
8.4	Competition between convection and diffusion	122
8.5	Experiment	123
8.5.1	Measurement technique	123
8.5.2	The lamp	124
8.6	Results	124
8.6.1	Elemental pressure	125
8.6.2	Atomic dysprosium density	125
8.7	Cold spot vapour pressure	130
8.7.1	Demixing	134

8.8	Conclusions	135
8.9	2D images of the metal-halide lamp obtained by experiment and model	137
9	Conclusions	141
9.1	Introduction	141
9.2	Laser absorption spectroscopy (1D) at $1g$ and $0-2g$	141
9.2.1	Laboratory measurements at $1g$	141
9.2.2	Parabolic flights	142
9.3	Imaging Laser Absorption Spectroscopy (2D) at $1-10g$	142
9.3.1	Development of the centrifuge and ILAS	142
9.3.2	Extended axial segregation model	142
9.3.3	Analysis	143
9.4	Emission spectroscopy	143
9.4.1	Lamps with DyI_3	143
9.4.2	Commercial lamps	143
9.5	Comparison with numerical modelling	144
9.6	Overview axial segregation parameters	144
9.7	General outlook	145
	Bibliography	147
	Summary	153
	Samenvatting	157
	Dankwoord	161
	List of publications	163
	Curriculum Vitae	171

1

General introduction

Abstract.

The aim of this thesis is to characterize a well verifiable metal-halide (MH) lamp and obtain a set of reliable measurement data. The experimentally obtained data is used to validate existing numerical models of the MH lamp, which gain a better understanding of the plasma properties and transport phenomena in the MH lamp. In this thesis we study the additive distribution and the resulting light output of the lamp. Axial segregation of the additive, which is caused by the combination of the convective and diffusive phenomena in the lamp, is investigated. Convection is induced by gravity and therefore the lamp was measured under varying gravity conditions. In this thesis measurements during parabolic flights and in a centrifuge are presented. The diagnostics to investigate the lamp are laser absorption spectroscopy, the newly developed Imaging Laser Absorption Spectroscopy, and emission spectroscopy. The results are used as input for a numerical model of the same lamp.

Parts of this chapter have been submitted, in altered form, as [A.J. Flikweert, T. Nimalasuriya, G.M.W. Kroesen, M. Haverlag and W.W. Stoffels, *The metal-halide lamp under varying gravity conditions measured by emission and laser absorption spectroscopy*, Microgravity Science and Technology (2008)].

Worldwide, 20% of all electricity is used for lighting [1–3]. For this reason, efficient lamps are economically and ecologically important.

1.1 Incandescent lamps

The first practical lamp, based on a carbon filament, was made by Edison in 1876. The filament acts as a resistor, heats up and radiates light. Later on, it turned out that tungsten is the best material for the filament. Due to the good colour rendering of the incandescent lamp and the simple design, they are still widely used in domestic applications.

The efficiency and the life time were increased by the introduction of the halogen lamp. Halogen lamps are also still widely used, for instance in car headlamps and shop lighting.

The physical process behind the generation of light by incandescent lamps is black body radiation. Ideally, the power loss is dominated by this black body radiation [4], but conduction can also be important. A large part of the radiation is in the infrared and not in the visible. This results in efficiencies of about 4% for incandescent lamps, which is one of the worst of all lamps. A more efficient way to generate light is by using a plasma.

1.2 Gas discharges

In gas discharge lamps, plasma is created by the electrical current flowing through the gas. Plasma can be seen as the fourth state of matter, besides solid, liquid and gas. In the universe, about 99% of the visible material is plasma.

A plasma is an ionized gas. It contains free electrons, ions and sometimes charged clusters or dust particles. Because of the charged particles, a plasma conducts electricity and particles can be excited and radiate light. A plasma usually has a temperature of several thousands or ten thousands of degrees. Therefore, plasma is not abundant on earth. In the universe, plasma is abundant in the form of stars and interstellar nebulae. On earth, examples of plasmas are (ball) lightning, the aurora and a candle flame.

Plasmas are created by men for several purposes. In this section, some applications of low- and high-pressure discharges are given.

1.2.1 Low-pressure discharges

In low-pressure discharges (pressure below 1 bar), the collision frequency between electrons and heavy particles is low, so electrons can remain at a high temperature, whereas the heavy particles remain relatively cool due to contact with the wall. This means that the plasma is not in local thermodynamical equilibrium (LTE). Due to the high

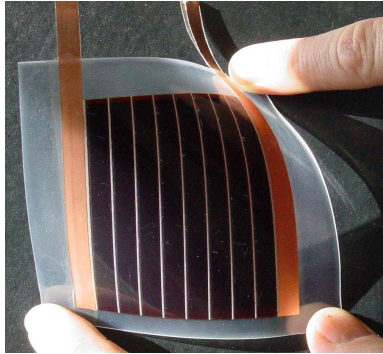


Figure 1.1: Example of a plasma produced flexible solar cell, made by Akzo Nobel [6].

electron temperature, the plasma is chemically active. Many applications are based on the reactive plasmas, like plasma deposition, etching and surface modification.

An example of plasma deposition is the production of thin-film solar cells within the Helianthos project [5, 6]. For the production of flexible, thin-film solar cells, a roll-to-roll machine is used. The technique for deposition of the various layers on the film is plasma-enhanced chemical vapour deposition. The plasma is a silane (SiH_4) plasma; dopants are added to obtain the various active layers of the solar cell. Figure 1.1 shows a picture of a plasma produced flexible solar cell.

Another application of a low-pressure discharge is a thruster based on plasma. A thruster is used as engine in space, for instance for interplanetary travel and altitude control of satellites. The requirements for a thruster are a low propellant consumption and a high energy efficiency. The Helicon Double Layer Thruster is developed at the Australian National University (ANU) [7–15] and meets these requirements. The thruster accelerates the propellant to about 15 km s^{-1} , gaining momentum in the mN range. The propellant in this thruster is argon. The argon plasma is created using a helicon system. A current-free double layer is created; the potential drop in this layer accelerates the argon ions. A schematic drawing of Chi Kung, a horizontal helicon system, is shown in figure 1.2.

Regarding lighting, examples of low-pressure discharge lamps are compact fluorescent lamps (also known as energy-saving lamps) and fluorescent tubes. They have better efficiencies (20%–30%) than incandescent lamps and longer lifetimes. These lamps contain mercury. Mercury is an efficient radiator, but radiates in the UV. The phosphor coating in the fluorescent tubes converts the UV to the visible, but about half of the photon energy is lost in this conversion (the so-called Stokes losses). Another example is the well-known low-pressure sodium lamp (deep orange street lighting), which has a slightly lower discharge conversion efficiency, but the 589 nm line is around the

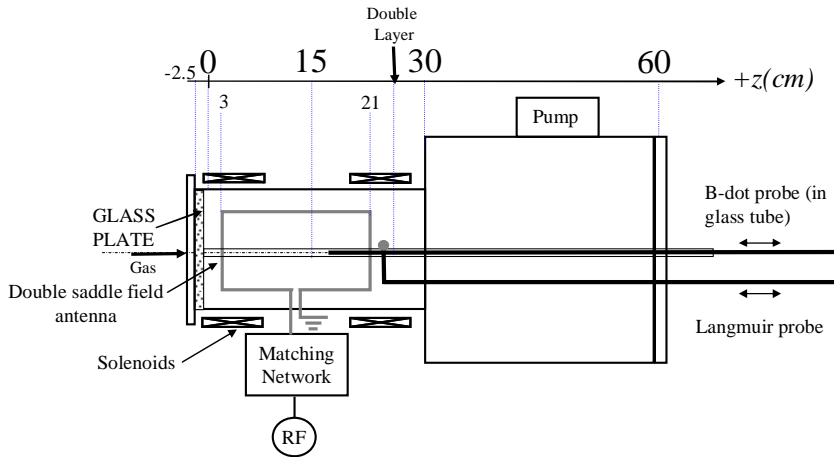


Figure 1.2: Schematic overview of Chi Kung, a horizontal helicon system at the ANU [8]. The power is inductively coupled by a double saddle antenna. The gas inlet is at the left, whereas the pump is at the right vessel. At the position of the expansion of the plasma (between the narrower launch vessel and the wider expansion vessel) a double layer is formed, where the Ar ions are accelerated. The measurement techniques to investigate the plasma are a \dot{B} probe [16] and a Langmuir probe.

maximum of the human eye's sensitivity. Therefore, no phosphor is needed, resulting in a higher efficiency. The monochromatic light limits the application of the low-pressure sodium lamp.

1.2.2 High-pressure discharges

In high-pressure discharges (atmospheric pressure, or above 1 bar), the collision frequency between electrons and heavy particles is high.

Examples of atmospheric-pressure discharges are corona discharges [17] and the plasma needle with biomedical applications [18, 19]. The plasma needle is applied directly on organic materials and living tissues [20]. Possible applications are high-precision removal of unwanted cells and use in dentistry to clean dental cavities, prior to filling. The plasma is small enough (~ 1 mm) for local surface treatment.

In lighting, High Intensity Discharge (HID) lamps are high-pressure discharges based on arc emission [3, 21–26]. HID lamps are efficient lamps with often a good colour rendering index. The first HID lamps were mercury lamps at atmospheric pressure. They also emit UV which is converted by a phosphor into visible light, but the ratio of visible to UV is greater than for the fluorescent tubes. A better white lamp is obtained when salt additives (metal halides) are added to the mercury lamp. These

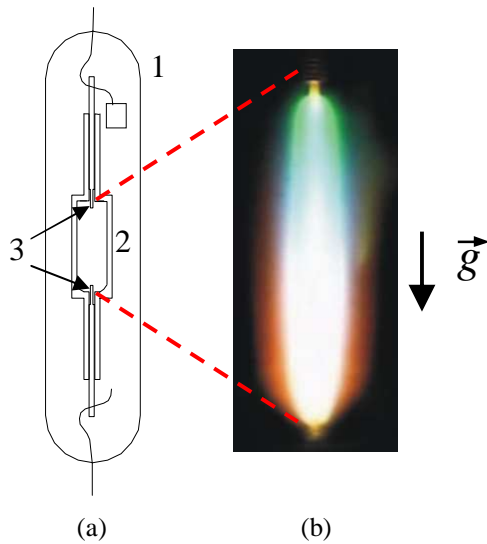


Figure 1.3: (a) Schematic picture of the COST reference lamp [27], (1) outer bulb; (2) burner (size 8 mm x 20 mm); (3) electrodes, distance between both electrodes ~ 16 mm. (b) The burner of a MH lamp (contains 10 mg Hg and 4 mg DyI_3), colour segregation is clearly visible.

lamps are known as metal-halide (MH) lamps. MH lamps have a high efficiency (up to 40%) [3] and emit white light. They are mainly used for applications where a high light output is desired; examples are shop lighting, street lighting, flood lighting of sport stadiums and city beautification.

1.3 Metal-halide lamp

1.3.1 The COST reference lamp

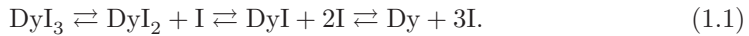
The MH lamps we use are MH reference lamps developed within the European COST action program 529 [27]. The definition of a standard laboratory MH lamp allows us to get comparable results from the worldwide available diagnostic and modelling techniques for MH lamps. A schematic drawing of the lamp is given in figure 1.3(a). The diameter of the lamp burner is 8 mm and the burner height is 14 to 20 mm. The electrode distance is 8 or 16 mm. The lamp contains Ar/Kr⁸⁵ as starting gas, Hg as buffer gas and a salt additive (we mainly use DyI_3). When the lamp is ignited, the Hg evaporates and a mercury discharge is created. The lamp heats up and the salt additive enters the arc discharge.

1.3.2 Axial segregation

When the lamp is burning vertically, segregation of the additives occurs [27, 28] and colour segregation appears. This limits the lamp design for application in, for example, shop lighting; these lamps are oriented in various direction. Figure 1.3(b) shows an image of the plasma when the lamp is burning. The bluish-white light at the bottom is caused by Dy atoms, whereas the bluish colour at the top is caused by Hg atoms. This non-uniform light output has a bad influence on the efficiency and the colour rendering of the lamp.

For the case of DyI_3 as salt additive the situation is as follows. The centre of the arc is much hotter (~ 5500 K) than the wall (~ 1200 K) [29]. First we have convection because of this large gradient. Convection is induced by gravity. The hot gas in the centre moves upward, whereas the colder gas near the wall moves downward.

Because of the large temperature gradient a multi-step process of dissociation of DyI_3 molecules near the centre and association of atoms at the wall takes place [30]:



With increasing temperature the equilibrium moves to the right-hand side. Furthermore in the centre of the burner, ionization of Dy atoms takes place because of the high temperature [31]:



Due to the different diffusion velocities of the heavier molecules and the lighter atoms and ions, the molecules move slower inward than the atoms and ions move outward. This causes a hollow radial pressure profile of atoms: radial segregation. Note that this is in addition to the ideal gas law $p = nkT$; a higher temperature gives a lower density.

While the Dy atoms are moving outward and get closer to the wall, they are dragged downward by the convection. In this way the Dy atoms stay mainly at the bottom of the lamp. The combination of convection and radial segregation thus causes axial segregation in the lamp as seen in figure 1.3(b). The representative flow lines of the atomic dysprosium are drawn in figure 1.4.

Axial segregation of Dy is thus caused by the combination of convection and diffusion. When the time scales of these effects are in the same order of magnitude, maximal axial segregation occurs. In the limiting cases, when the convection is absent or when the convection is much stronger than diffusion, good mixing is observed: no axial colour segregation is observed in the lamp. E. Fischer [28] developed a theory for an infinitely long lamp which gives the amount of segregation as a function of the amount of convection, which is depicted in figure 1.5. Because the convection is induced by gravity, measuring under different gravity conditions aids the understanding of the diffusive and convective processes.

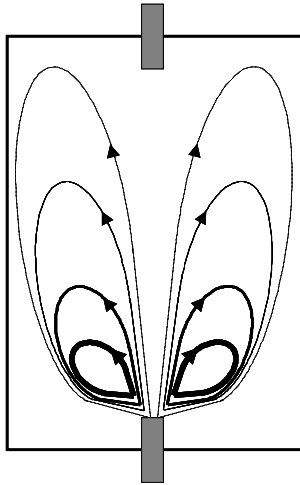


Figure 1.4: Schematic of the flow lines of atomic dysprosium in the burner. Thick lines represent a high dysprosium density whereas thin lines represent a low density [32].

1.4 Varying gravity conditions

Convection in the MH lamp is caused by gravity and to gain more insight in the flow phenomena, the lamp is investigated under varying gravity conditions. Besides laboratory experiments ($1g$, where g is the gravity at earth: 9.81 m s^{-2}) [32, 34–36], the lamp is investigated during parabolic flights. Here the lamp is measured during periods of about 20 s of micro-gravity ($0g$) and hyper-gravity ($\sim 1.8g$) [33]. Finally the lamp is placed in a centrifuge ($1\text{--}10g$) [35, 37–39]. This centrifuge is used as a tool to vary the (artificial) gravity and thus the amount of convection for a longer time than at the parabolic flights to assure stable arc conditions.

1.4.1 Parabolic flights

During the parabolic flights, the dynamic lamp behaviour is investigated to obtain a relationship between the gravity and atomic Dy density in the lamp. The lamp has been measured during the parabolic-flight campaign of the European Space Agency (ESA) in June 2004 [40]. During each flight, 31 parabolas with micro-gravity and hyper-gravity were performed. Figure 1.6 shows one parabola schematically.

For a thorough investigation of the lamp the periods are also too short. Therefore a centrifuge was built, where hyper-gravity can be prolonged.

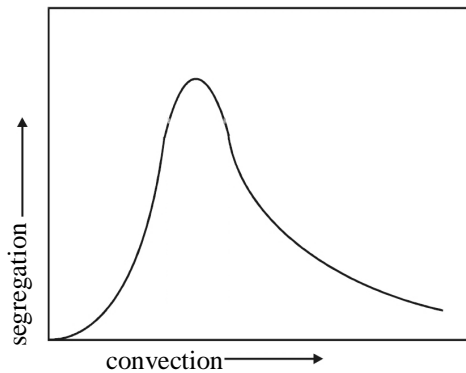


Figure 1.5: The Fischer curve [28, 33] which gives the amount of axial segregation as a function of the amount of convection. Convection is induced by gravity. At $1g$, where g is the gravity at earth (9.81 m s^{-2}), our lamps are around the maximum of the curve.

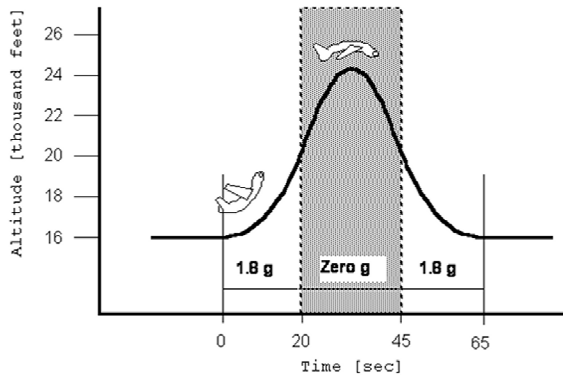


Figure 1.6: Sequence of a parabola: first hyper-gravity ($\sim 20 \text{ s}$), next micro-gravity ($\sim 25 \text{ s}$) and finally again hyper-gravity [33, 40].

1.4.2 The centrifuge

A centrifuge was built to investigate the lamp under hyper-gravity conditions [37]. The gravity that is achieved by the centrifuge ranges from $1-10g$.

A schematic representation of the centrifuge is given in figure 1.7. The centrifuge consists of a pivot, an arm and a gondola attached to the arm. The gondola contains all electrical equipment and the measurement setup (including lamp) itself. The total diameter at maximum swing-out of the gondola is about 3 m. The maximum rotation

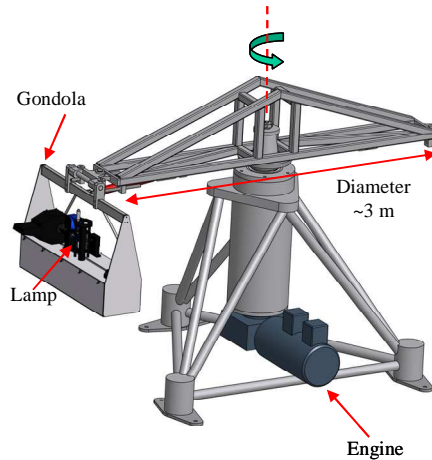


Figure 1.7: Schematic representation of the centrifuge. It consists of a pivot, an arm and the gondola that contains the lamp and diagnostics [37].

frequency is ~ 1.5 Hz which corresponds to a velocity of 50 km h^{-1} . The gondola swings out around its hinge point when spinning the centrifuge, so the artificial gravity vector is always parallel to the lamp axis.

The measurement system in the centrifuge is shown in figure 1.8. We use a control PC outside the centrifuge laboratory. This PC drives the frequency controller of the centrifuge engine. The gondola contains another (mini-) computer on which the experimental software is running. The experimental software is written in National Instruments LabWindows/CVI. In addition to this computer, the gondola contains all the equipment: the lamp power supply, a CCD camera, an ordinary webcam, the laser controller and a data acquisition system. The lamp and diagnostics are on the rail on top of the gondola. The computer inside the gondola is connected to the control PC by the wireless network. The only fixed connection (slip ring) to the outer world is the 230 V power wire. We use Windows Remote Desktop to operate the gondola PC. During the measurements, the gondola PC collects the data on its flash disks. After the measurements are finished, the data is transferred to the control PC and the data is processed off-line.

The lamp is monitored on-line by a simple webcam. From the webcam images, colour segregation can be observed clearly. Figure 1.10 shows various webcam images of a lamp with 10 mg Hg and 4 mg of DyI_3 [39]. The input power is 150 W. A picture taken at $0g$ is displayed for comparison. This picture was taken during experiments in the International Space Station (ISS) [41]. The other images are taken at the centrifuge setup. At $0g$ no axial segregation is present; we are at the origin of the Fischer curve

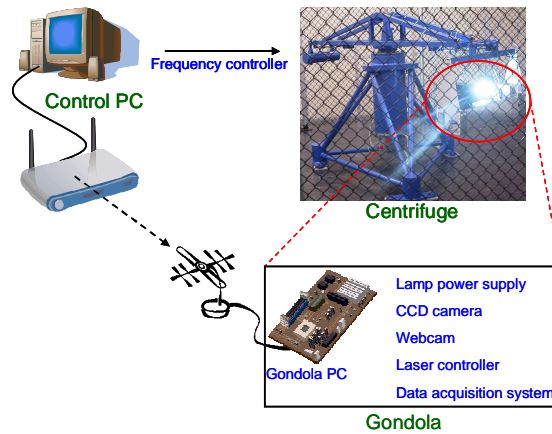


Figure 1.8: The measurement system in the centrifuge. The equipment in the centrifuge gondola is controlled by a mini-computer, which is connected via wireless network to the control PC.

(figure 1.5). At $1g$ we are in the area of the maximum of the curve. Increasing the gravity means increasing the convection and thus moving to the right on the Fischer curve. This is observed in the pictures: when gravity is increased, better mixing occurs and axial segregation is diminished.

1.5 Diagnostics

In this section the diagnostics are discussed. Laser absorption spectroscopy has been used in laboratory experiments and during parabolic flights. The Imaging Laser Absorption Spectroscopy (ILAS) technique is an extension of the laser absorption technique. The ILAS technique is used in the experiments under hyper-gravity in the centrifuge. Finally emission spectroscopy is discussed.

1.5.1 Laser absorption spectroscopy (1D)

In the measurements in the laboratory and during the parabolic flights, we use laser absorption spectroscopy. The beam of a diode laser is expanded to a sheet. When it illuminates the lamp, part of the light is absorbed by the dysprosium atoms. After the lamp and optics the laser light hits a diode array, which measures the remaining intensity of the laser light. In this way, a line-of-sight density profile of atomic ground state dysprosium is obtained at one axial position of the lamp (one-dimensional, 1D), which gives a measure for the amount of axial segregation. In the laboratory experiments,

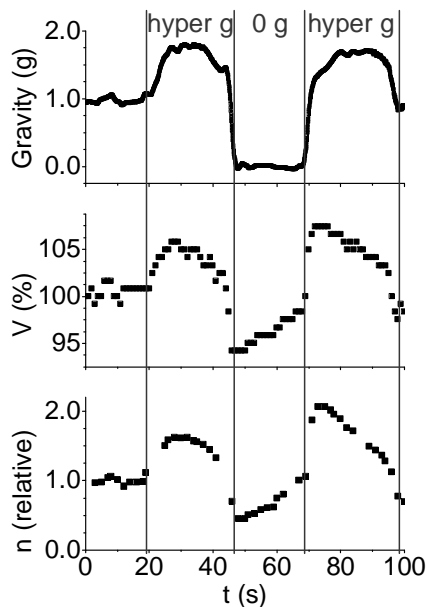


Figure 1.9: Gravity, lamp voltage and radially averaged ground state atomic Dy density for a lamp with 10 mg Hg and 4 mg DyI₃ during one parabola, as functions of time [33].

the lamp is measured at several axial positions; a 2D density profile is constructed from these 1D measurements.

During the parabolic flights, the Dy density in the lamp and the voltage over the lamp (which is proportional to the total amount of Dy in the arc) are measured during a parabola. Figure 1.9 shows an example of the density and voltage of the lamp with 4 mg DyI₃ and 10 mg Hg, at 150 W input power. The values given in this graph are relative values; the atomic ground state Dy density is in the order of 10^{21} m^{-3} and the voltage is ~ 80 V. The increase in Dy density at the first hyper-gravity phase is explained by a better mixing and thus less axial segregation above $1g$. This is because we are at the right-hand side of the Fischer curve (figure 1.5) [32, 33, 41]. However, it is seen that at the end of the micro-gravity phase, the Dy density is still not constant. This is because the diffusion time constant is larger than the 25 s of micro-gravity. This problem does not occur in the ISS, where we have micro-gravity for a period much longer than during the parabolic flights.

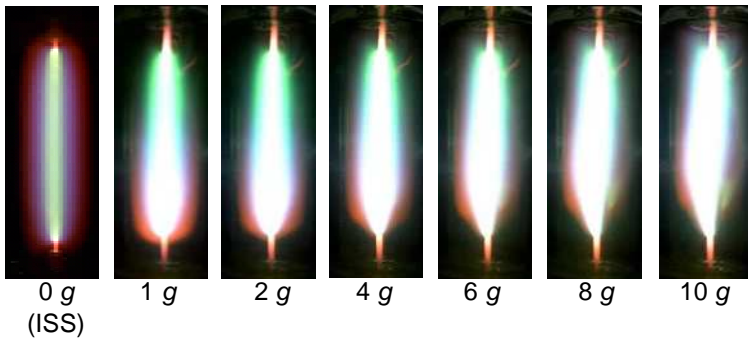


Figure 1.10: Pictures of the lamp at 0–10 g . The first image is taken in the ISS [41], the others are taken in the centrifuge setup [37, 39]. Note that the exposure time of the ISS picture is different from those at the centrifuge.

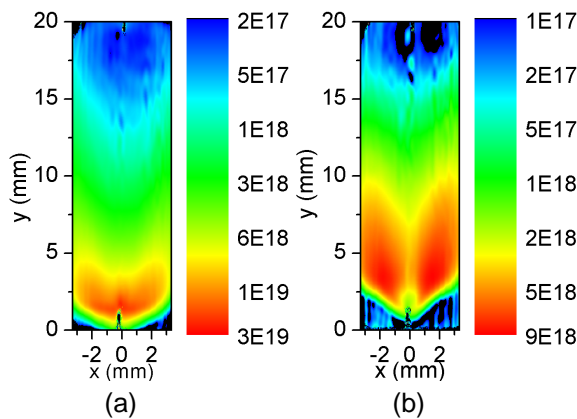


Figure 1.11: Atomic ground state Dy density measured by ILAS [37], $P = 150$ W, 5 mg Hg and 4 mg DyI₃, (a) 1 g ; (b) 10 g . Note that the flame-like pattern at the top of the lamp is an artefact caused by the data analysis.

1.5.2 Imaging Laser Absorption Spectroscopy (2D)

The Imaging Laser Absorption Spectroscopy (ILAS) technique [37] is an extension of the laser absorption technique. In contrast to the 1D laser absorption spectroscopy, ILAS yields the 2D density distribution of ground state atomic Dy. We use a diode laser and scan around an absorption line of atomic Dy (642.19 nm). The laser beam is expanded so it illuminates the whole lamp burner. While passing the lamp, the Dy atoms in the lamp absorb part of the beam. After the lamp and optics, the laser light is imaged

on a CCD camera. In this way, for each position in the lamp an absorption profile is constructed. From these profiles the atomic ground state Dy density is calculated so a 2D density plot is obtained.

The 2D density of ground state atomic Dy is shown for $1g$ and $10g$ in figure 1.11. The lamp filling is 5 mg Hg and 4 mg DyI₃; the input power is 150 W. These density profiles show that a better mixing occurs at $10g$: the amount of Dy at the top of the lamp is increased. This is consistent with the webcam images in figure 1.10, which show also a better mixing and thus less colour segregation at higher gravity.

1.5.3 Emission spectroscopy

The lamp is investigated by means of emission spectroscopy, which gives the line intensities of the different particles in the lamp. A 0.25 m spectrometer is placed in the gondola in the centrifuge. The lamp is focused on the entrance slit of the spectrometer. The entrance slit is in vertical direction; in this way an axial profile of the lamp is imaged on the spectrometer slit. After the spectrometer, the dispersed light hits a CCD camera. The image contains the wavelength in horizontal direction and the axial position in the lamp in vertical direction. In this way, we obtain axial intensity profiles of different species. These axial intensity profiles can be analyzed; in this way a measure for the axial segregation can be found.

T. Nimalasuriya *et al* [35, 41] built a more complex emission spectroscopy setup. The spectrometer used for the optical emission measurements is originally designed for the ISS: it has to be compact and lightweight. These requirements are met using a Echelle spectrometer. In this setup, the slit is in horizontal direction, yielding lateral emission profiles. By using this setup, the temperature profile of the lamp is obtained from a calibrated Hg line. After combining these temperature profiles with the calibrated Dy lines, absolute Dy densities are obtained.

The axial segregation that is observed by the webcam (figure 1.10) is also observed by emission spectroscopy. In figure 1.12 the intensity profiles of a Dy line are shown as a function of the lateral position in the lamp. These profiles are obtained at 3 axial positions in the lamp (10 mg Hg, 4 mg DyI₃, $P = 150$ W), for both normal gravity ($1g$) and $10g$. Note that the intensity profiles and webcam images were taken from different angles (90° with respect to each other) [37]. From the profiles at the bottom, we see that the amount of Dy decreases from $1g$ to $10g$. At the top we see an increase of the amount of Dy when increasing g ; Dy is mixed better over the lamp (less axial segregation).

1.6 Thesis outline

This thesis deals with various diagnostic techniques to investigate the MH lamp. Together with the thesis of T. Nimalasuriya [35], which deals with a poly-diagnostic (ex-

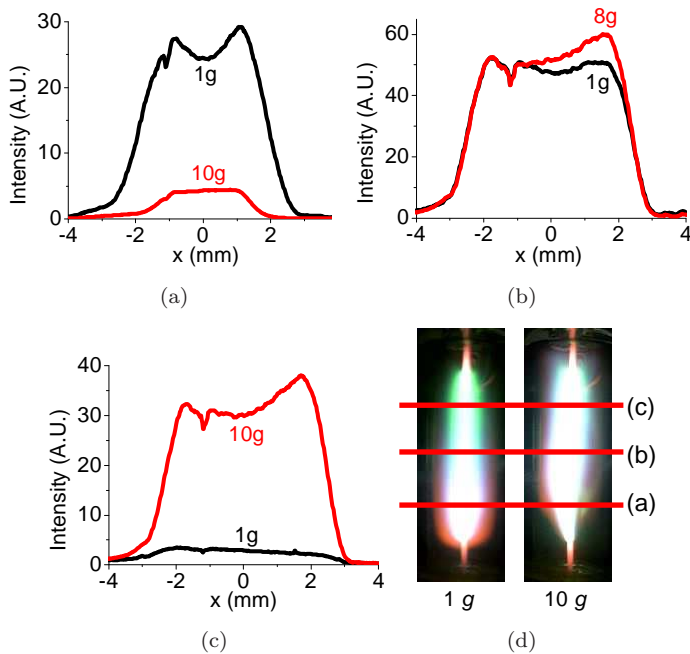


Figure 1.12: Atomic Dy line (642.19 nm) intensities at different axial positions in the lamp measured by emission spectroscopy, for normal and hyper-gravity [38]: (a) bottom; (b) centre; (c) top. In (d) the webcam images are given for comparison; the positions where the profiles were taken are indicated (printed in colour in figure 1.10).

perimental) study of the MH lamp and the thesis of M.L. Beks [42], which is about the modelling of the MH lamp, it presents a complete overview of the dominant processes which govern the segregation phenomena in MH lamps.

Chapter 2 presents laser absorption measurements on the MH lamp with DyI_3 at 1g. The 1D laser absorption spectroscopy is discussed and some results of a MH lamp with 10 mg Hg and 4 mg DyI_3 are shown.

In chapter 3 the lamp is investigated during parabolic flights (0–2g). The diagnostics are 1D laser absorption spectroscopy, lamp voltage measurements, and integrated light output measurements. Three lamps with different amounts of Hg are compared.

Chapter 4 presents the centrifuge, which yields an acceleration between 1–10g. This chapter also describes the newly developed (2D) Imaging Laser Absorption Spectroscopy setup. This setup is developed from the knowledge of the 1D setup that is presented in chapters 2 and 3.

In the first ILAS measurements, a deviation from the Fischer model is observed. This

model assumes an infinitely long lamp with a constant axis temperature. In chapter 5, the axial segregation model by Fischer is extended for our lamps; real lamps have finite length and have an axial temperature gradient. This chapter also introduces some new parameters to characterize the lamp.

Chapter 6 presents ILAS measurements on the lamps and a thorough analysis of the obtained results. The measurements are under 1–10*g*. The centrifuge and the ILAS technique used to investigate the lamp have been introduced in chapter 4.

In addition to the ILAS measurements, emission spectroscopy measurements under 1–10*g* have been carried out on the same lamps in chapter 7. After validation of the measurement technique by comparing the results with those obtained in chapter 6, also commercially available lamps are investigated.

The results obtained by ILAS are compared to results obtained by numerical modelling. This is done in chapter 8. First the model is presented and some experimental results are compared with the results obtained by modelling. The last part of the chapter presents and compares two-dimensional images obtained by experiment and model.

Finally in chapter 9 we combine the conclusions of the different chapters, draw general conclusions, give an overview of the various introduced axial segregation parameters and give an outlook for future work.

2

Axial segregation in high intensity discharge lamps measured by laser absorption spectroscopy

Abstract.

High intensity discharge lamps have a high efficiency. These lamps contain rare-earth additives (in our case dysprosium iodide) which radiate very efficiently. A problem is colour separation in the lamp because of axial segregation of the rare-earth additives, caused by diffusion and convection. Here two-dimensional atomic dysprosium density profiles are measured by means of laser absorption spectroscopy; the order of magnitude of the density is 10^{22} m^{-3} . The radially resolved atomic density measurements show a hollow density profile. In the outer parts of the lamp molecules dominate, while the centre is depleted of dysprosium atoms due to ionization. From the axial profiles the segregation parameter is determined. It is shown that the lamp operates on the right-hand side of the Fischer curve [J. Appl. Phys. **47**, 2954 (1976)]: a larger convection leads to less segregation.

This chapter has been adapted from [A.J. Flikweert, T. Nimalasuriya, C.H.J.M. Groothuis, G.M.W. Kroesen, and W.W. Stoffels, *Axial segregation in high intensity discharge lamps measured by laser absorption spectroscopy*, J. Appl. Phys. **98** (2005) 073301].

2.1 Introduction

The goal of this research is to gain a better understanding of the metal-halide lamp (MH, which is a High Intensity Discharge lamp, HID) [3] with a high efficiency (up to 40%), so that it can be improved. These lamps contain usually mercury as buffer gas and often rare-earth additives which radiate very efficiently in the visible spectrum. Ideally the lamp radiates white light, but when the lamp burns vertically, colour separation takes place because of segregation of the rare-earth additives. A picture of the colour separation is shown in figure 2.1.

The colour separation is caused by a combination of radial and axial segregations; the latter is caused by the combination of convection and diffusion [21–25]. E. Fischer [28] has formulated a simplified theory explaining the segregation based on the diffusion and convection in the lamp. Convection is caused by gravity and in order to understand its influence the lamp has recently been investigated under micro-gravity conditions so that no convection flows were present. To obtain micro-gravity, experiments during parabolic flights and at the International Space Station have been performed.

To get more insight in the flow phenomena and the segregation in the lamp, we present absorption measurements of atomic dysprosium. From this a two-dimensional density profile of the rare-earth atoms is obtained. We want to understand the theory about radial and axial segregations (depicted by E. Fischer) quantitatively by means of a model and experimental verification.

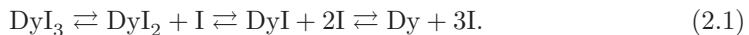
First we briefly introduce the theory of diffusion, convection, and axial segregation in the lamp. Next absorption spectroscopy is discussed and the experimental setup is presented. Finally the results of measurements on a lamp for two different input powers is given; the density profiles are shown and the segregation parameters are obtained from these profiles.

2.2 Theory

The segregation theory on MH lamps has been invented by E. Fischer [28]. It will be briefly summarized here for our specific case of a DyI_3 containing lamp (burner height 20 mm, diameter of 8 mm).

2.2.1 Radial segregation

The centre of the burner is much hotter (~ 5500 K) than the wall (~ 1200 K) [29]. Because of this large temperature gradient a multi-step process of dissociation of DyI_3 molecules near the centre and association of atoms at the wall takes place [30]:

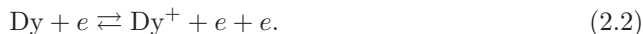


With increasing temperature the equilibrium moves to the right-hand side. Furthermore in the centre of the burner ionization of Dy atoms takes place because of the high



Figure 2.1: (printed in colour in figure 1.3) Picture of a HID lamp burner (real size 8 mm x 20 mm); colour separation is clearly visible.

temperature [31]:



The diffusion velocities of atoms, molecules and ions are different. Due to the different velocities the particles in the hotter part diffuse faster than the particles in the colder part. This results in a hollow profile of the elemental density of dysprosium; this is called radial segregation. Elemental density means that contributions from all molecules, atoms and ions of a particular element are included. Note that this is in addition to the ideal gas law $p = nkT$; a higher temperature gives a lower density.

2.2.2 Convection and axial segregation

In addition to radial segregation, the radial temperature gradient is related to convection in the lamp. The gas in the hot centre moves upwards whereas the gas at the wall moves downwards. As discussed in section 2.2.1, the maximum of the elemental Dy density lies in the part where the gas moves downward. This causes the Dy density to be higher near the bottom than near the top of the burner: axial segregation occurs [21, 22]. A picture of the diffusion and convection flows of the atoms and molecules is given in figure 2.2.

The simple axial segregation model by E. Fischer results in an exponential decrease of the axial Dy density $n_{\text{Dy}}(z)$ with increasing height in the plasma [28]:

$$n_{\text{Dy}}(z) = n_{\text{Dy},0} \exp(-\lambda z), \quad (2.3)$$

where the axial segregation is described by the segregation parameter λ and $n_{\text{Dy},0}$ is the atomic dysprosium density at the bottom of the lamp.

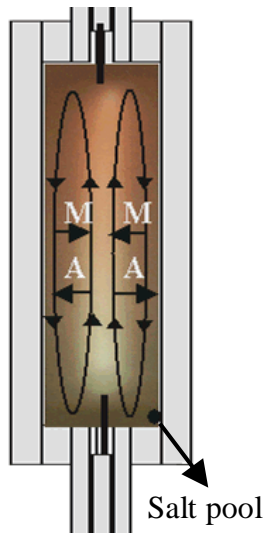


Figure 2.2: Schematic view of the burner in a HID lamp; diffusion and convection of atoms (A) and molecules (M) are indicated by arrows.

As explained, axial segregation is due to the combined effect of radial segregation and axial convection. In the absence of convection, or in the limit of extremely high convection speeds, there is no axial segregation and consequently the segregation parameter λ is zero (no axial colour separation). In the intermediate region λ has a maximum. This is depicted by the so-called Fischer curve [28], shown in figure 2.3, which gives the dependence of λ on the amount of convection inside the lamp. The amount of convection increases with the pressure in the lamp (Fischer), the input power [23, 24],¹ the gravity [43], and radius of the burner.

2.3 Experimental setup

To get insight into axial and radial segregations, the absolute number density of ground state atomic dysprosium is measured by means of laser absorption spectroscopy.

The lamp that is measured is shown schematically in figure 2.4. It contains 10 mg of mercury as buffer gas, 300 mbar Ar/Kr as starting gas and 4.2 mg DyI_3 as salt additive. The lamp driver that is used (Philips HID-DynaVision type LA 03 07)

¹Nimalasuriya *et al* [41] observed more contraction when the power is increased, leading to a higher axis temperature and a higher convection speed. In addition, the radial segregation increases with increasing power, which leads to a stronger axial segregation.

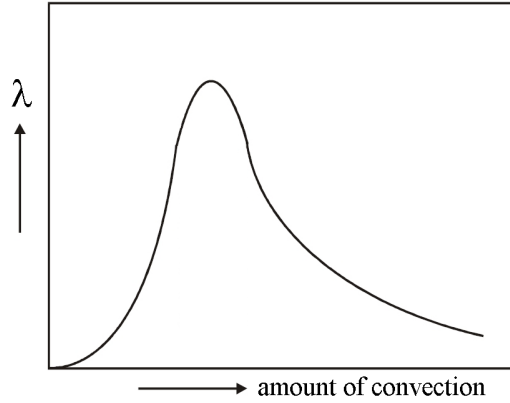


Figure 2.3: The Fischer curve, giving the dependence of the segregation parameter λ (equation (2.3)) on the convection in the lamp.

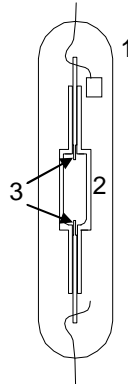


Figure 2.4: Schematic picture of the HID lamp: (1) outer bulb; (2) burner with height 20 mm and diameter 8 mm; (3) electrodes, distance between both electrodes ~ 18 mm.

delivers a square-wave current to the lamp with a frequency of 125 Hz. The lamp is measured at two different input powers (113.5 and 151 W) to see the dependence of segregation on the input power. The input power is determined by using a power analyzer (Lem Norma 3000).

A diode laser (Sacher TEC 500 645-5, typical line width ≤ 2 MHz or ≤ 3 fm) scans a small wavelength range (0.14 nm) around the absorption wavelength $\lambda = 642.19$ nm (transition from ground state $[\text{Xe}].4f^{10}6s^2\ ^5I_8$ to excited state $[\text{Xe}].4f^{10}(\ ^5I_8)6s6p(\ ^3P_0)$

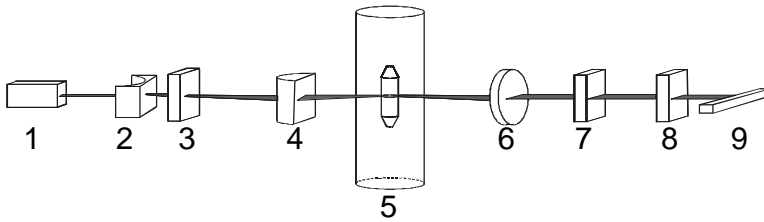


Figure 2.5: Schematic overview of the absorption setup to measure the ground state Dy density in a HID lamp: (1) diode laser; (2) cylindrical lens $f = -12.7$ mm; (3) slit; (4) cylindrical lens $f = +62.9$ mm; (5) lamp; (6) spherical lens $f = +100$ mm; (7) slit; (8) interference filter; (9) diode array.

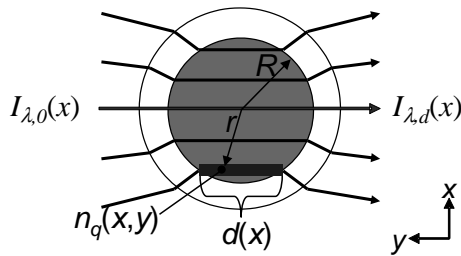


Figure 2.6: The laser beam $I_{\lambda,0}$ enters the inner bulb as a parallel beam. Inside the plasma with boundary R it is partially absorbed; $I_{\lambda,d}$ is the transmitted laser beam at the lateral position x . The local dysprosium density $n_q(x, y) = n_q(r)$ is indicated; however laser absorption samples the integrated line of sight $d(x)$ or column density.

(8,0)₈) by changing the piezo voltage of the grating. The line strength of this transition is $S = 6.65 \times 10^{-9} \text{ m}^2\text{C}^2$ [44, 45]. The line strength is related to the oscillator strength f_{qp} by $S = (3g_q h e^2 \lambda) / (8\pi^2 m_e c) \times f_{qp}$ where g_q is the allowed number of states of the ground level q . The line is pressure broadened² with an experimentally determined width of around 40 pm.

A schematic overview of the setup for laser absorption on a HID lamp is given in figure 2.5. The laser beam (beam height ~ 1 mm) passes two cylindrical lenses; in this way the laser spot is transformed to a parallel sheet inside the lamp burner. The width of the slit (no. 3 in the picture) is chosen so that exactly the whole width of the burner is illuminated. The inner and outer bulbs of the lamp act as negative cylindrical lenses. The beam passes the plasma in the burner as is shown in figure 2.6. Also indicated are the laser intensity $I_{\lambda,0}(x)$ in the absence of the plasma and the laser intensity $I_{\lambda,d}(x)$

²The mechanism is Van der Waals broadening [46] between Dy and Hg atoms, which leads to a Lorentzian line shape.

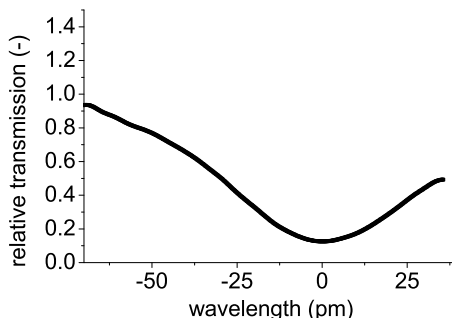


Figure 2.7: Typical relative transmission curve (lamp-on $I_{\lambda,0}(x)$ divided by lamp-off $I_{\lambda,d}(x)$) at a certain position x ; the wavelength is relative to the absorption wavelength (642.19 nm).

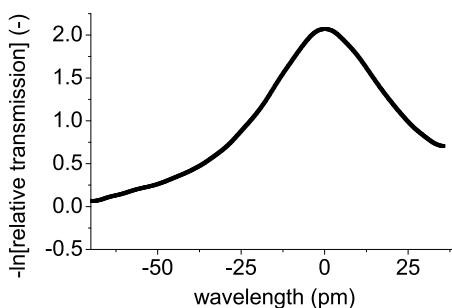


Figure 2.8: Logarithm of the relative transmission curve; the minus sign at the right-hand side of equation (2.6) is already included.

with the plasma. After the laser beam has passed through the lamp, it is converged to a parallel beam by a lens. Next it passes an interference filter and is detected by the diode array, which consists of 32 evenly spaced photodiodes. The detector channel is converted into a lateral position and corrected for nonlinearities. Each detector channel corresponds to a unique lateral position in the lamp burner. The lamp is translated in height in steps of 0.5 mm to measure the density at different axial positions. In this way a two-dimensional mapping (lateral and axial) is obtained.

To obtain the spatially dependent dysprosium density first, for every position, the spectrally resolved relative transmission curve (shown in figure 2.7) is measured by taking the ratio of the transmitted laser intensity with the lamp on (corrected for the lamp emission) and off. In order to obtain the lateral dysprosium density, the logarithm of the transmission curve is fitted assuming a Lorentzian line shape (figure 2.8). The

measurement and fit fully coincide; no difference is seen. The area under the Lorentz curve is proportional to the line-of-sight (column) density of the dysprosium [43, 47]:

$$n_{\text{col},q}(x) = \int_{-\frac{1}{2}d(x)}^{\frac{1}{2}d(x)} n_q(x, y) dy, \quad (2.4)$$

where $n_q(x, y)$ refers to the local dysprosium density of level q at position (x, y) in the plasma and $d(x) = 2\sqrt{R^2 - x^2}$ corresponds to the line-of-sight boundaries at lateral position x (see figure 2.6). The relation between the area under the Lorentz curve and the column density can be determined using the Lambert-Beer law for absorption:

$$\frac{dI_\nu(s)}{ds} = -\kappa(\nu, s)I_\nu(s), \quad (2.5)$$

where $I_\nu(s)$ is the spectral intensity of the laser beam (in $\text{W m}^{-2} \text{sr}^{-1} \text{Hz}^{-1}$) and $\kappa(\nu, s)$ the absorption coefficient (m^{-1}) at frequency ν at location s . After using the relation $\kappa(\nu, s) = Sn_q\phi(\nu, s)$ with $\phi(\nu, s)$ the line shape and integration over the frequency ν one obtains:

$$\int_0^\infty \ln\left(\frac{I_{\lambda,d}(x)}{I_{\lambda,0}(x)}\right) d\lambda = -\frac{S\lambda^2}{c} n_{\text{col},q} = -2\frac{S\lambda^2}{c} \int_x^R \frac{n_q(r)}{\sqrt{r^2 - x^2}} r dr. \quad (2.6)$$

Note that by this technique the result is independent of the actual line shape.³

Finally the measured column density data are converted into a radial density profile [29, 48, 49]. In order to minimize errors in the central region we choose to approximate the radial density profile by a polynomial series:

$$n_q(r) = a_0 + \sum_{n=2}^{\infty} a_n r^n \quad \text{for } r \geq 0. \quad (2.7)$$

The term $a_1 r$ is omitted because of the derivative of the dysprosium density at the axis of the burner should be zero. Using a least-square fitting procedure to the measured data the column values a_n are obtained and the radial profile is constructed.

Using this approach the density is independent of the actual line shape and depends linearly on the accuracy of the line strength S only.

2.4 Results

2.4.1 Lateral and radial profile

The lateral atomic dysprosium column density profile and the reconstructed radial profile 2 mm above the lower electrode of the lamp (151 W) are shown in figure 2.9. For fitting the radial profile, the terms until $n = 6$ are used (equation (2.7)).

³The width of the Lorentzian profiles may vary along the line-of-sight. After integrating over the line-of-sight we again obtain a Lorentzian profile, where the area under curve—and thus the density—might be underestimated by 10–20%.

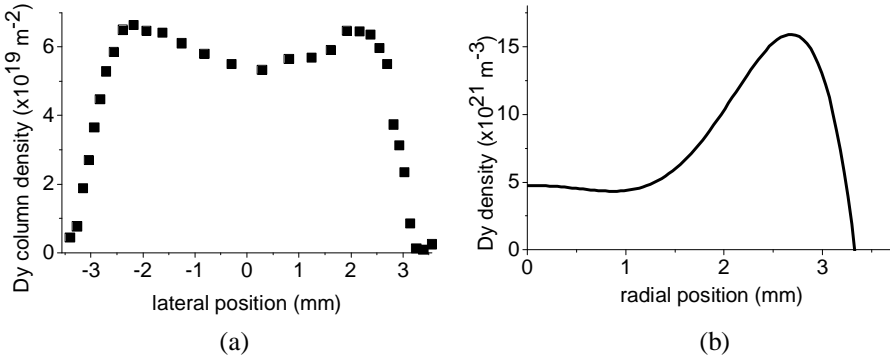


Figure 2.9: (a) Lateral dysprosium column density and (b) radial dysprosium density at 151 W; 2 mm above the lower electrode.

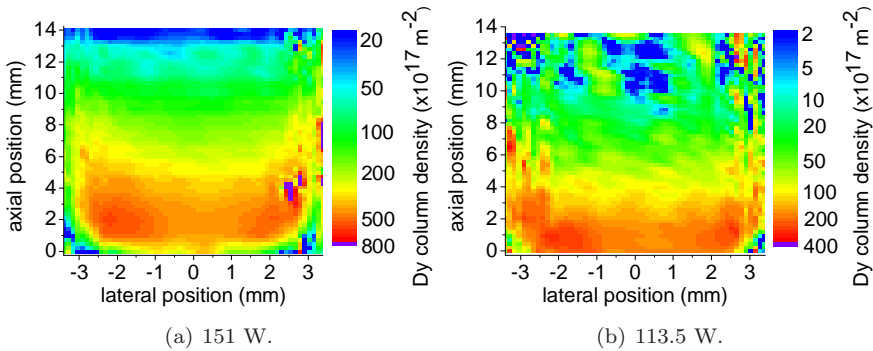


Figure 2.10: Two-dimensional profile of atomic dysprosium column density for (a) 151 W and (b) 113.5 W. The axial position of 0 mm is just above the lower electrode.

In figure 2.9(b) we see a hollow profile; this is in agreement with the theory (section 2.2.1). Atomic dysprosium is mainly present in a region around the central parts of the lamp (off-axis maximum), where the DyI_3 molecules are fully dissociated. Close to the centre the temperature is even higher than at the off-axis maximum, resulting in lower overall densities and a partial ionization of the atomic dysprosium.

Around $r = 1$ mm a small minimum is seen; this is an artifact caused by the limited number of lateral data points and the resulting incomplete reconstruction of the radial profile.

The order of magnitude of the dysprosium density (10^{22} m^{-3}) corresponds with expected values based on the cold spot temperature of DyI_3 of ~ 1100 K [29, 43].

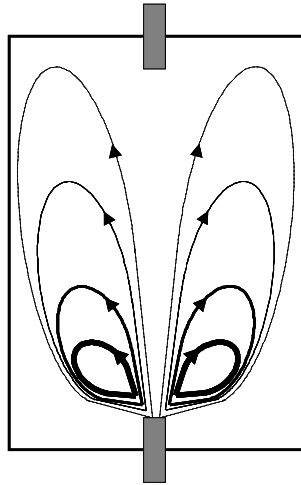


Figure 2.11: Representative flow lines of atomic dysprosium of what is believed to exist in the burner. The thick lines give a high dysprosium density whereas thin lines give a low density.

2.4.2 Two-dimensional profile

The two-dimensional profiles of the dysprosium column density of the lamp at 151 W and 113.5 W are given in figure 2.10. The curve in figure 2.9(a) corresponds to the horizontal line located at axial position 2 mm in figure 2.10(a).

The detection limit of the absorption measurement is around $2 \times 10^{18} \text{ m}^{-2}$ as is seen in the top of figure 2.10(b). Near the bottom one sees that the column density gets low towards the wall. This is because of the arc contraction at the electrode. Furthermore the burner is not exactly cylindrical; the bottom area of the burner is somewhat curved (see figure 2.4).

The structure of the two-dimensional dysprosium column density in figure 2.10 is also remarkable. The dysprosium column density right at the centre is lower than the dysprosium column density close to the centre. When convection (upward in the centre; downward near the wall) and diffusion (direction towards the wall) are combined, the flow lines of atomic dysprosium look like figure 2.11, which qualitatively explains the observed structure.

2.4.3 Axial segregation

To obtain the axial segregation parameter λ , the measurements shown in figure 2.10 are converted into a radially averaged profile.

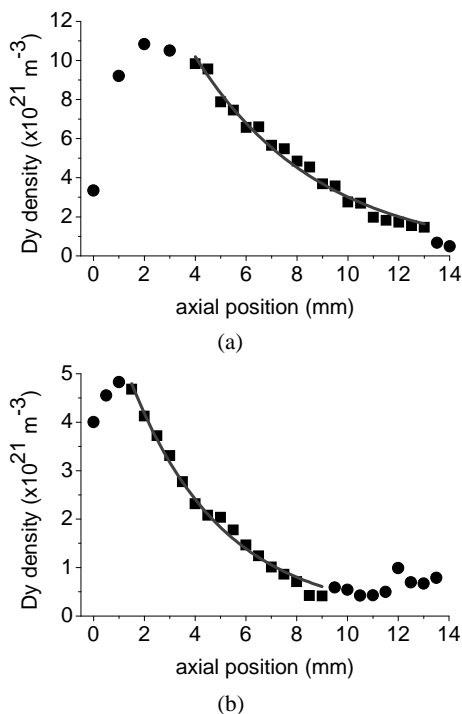


Figure 2.12: Dysprosium density as a function of axial position in the lamp (0 mm is just above the lower electrode). For the radial fit only a_0 (equation (2.7)) is taken into account. The segregation fit (equation (2.3)) is only applied to the square dots. The segregation parameters for two different input powers are (a) 151 W: $n_{\text{Dy},0} = (2.3 \pm 0.1) \times 10^{22} \text{ m}^{-3}$; $\lambda = 0.20 \pm 0.01 \text{ mm}^{-1}$; (b) 113.5 W: $n_{\text{Dy},0} = (7.2 \pm 0.2) \times 10^{21} \text{ m}^{-3}$; $\lambda = 0.28 \pm 0.01 \text{ mm}^{-1}$.

In figure 2.12 the atomic dysprosium density is shown as a function of axial position for 151 and 113.5 W. For both curves an exponential function is fitted according to equation (2.3) and the segregation parameters λ are obtained. The fit is not applied to the round dots; here deviation is present because of the electrodes and the not fully developed arc. The radial segregation at 113.5 W is larger ($\lambda = 0.28 \pm 0.01 \text{ mm}^{-1}$) than at 151 W ($\lambda = 0.20 \pm 0.01 \text{ mm}^{-1}$).

As already mentioned in the theory, the convection speed increases with increasing power. An explanation for the decreasing value of the segregation parameter λ with increasing power is that we are at the right part of the Fischer curve (figure 2.3); this agrees with previous findings on this lamp (parabolic flights where it is observed that the segregation decreased during a quick changeover to a 1.8g hyper-gravity situation [43]).

2.5 Conclusions

The radially and axially resolved absolute number density of atomic dysprosium in a HID lamp was measured by means of laser absorption spectroscopy; this has been performed for two different input powers (113.5 and 151 W). The order of magnitude of the atomic dysprosium density is about 10^{22} m^{-3} .

The radially resolved atomic density measurements show that there is a hollow density profile with a maximum in the Dy density between the centre and the boundary of the plasma. In the outer parts of the lamp molecules dominate, while the centre is depleted due to ionization of dysprosium. Furthermore the overall density decreases towards the centre because of the higher temperature.

Due to diffusion and convection there is a strong axial segregation in the lamp. Apart from the electrode regions the average axial dysprosium density follows the theoretically predicted exponential dependence, and corresponding segregation parameters have been found: $\lambda = 0.28 \pm 0.01 \text{ mm}^{-1}$ at 113.5 W and $\lambda = 0.20 \pm 0.01 \text{ mm}^{-1}$ at 151 W. This shows that the lamp is operating at the right-hand side of the Fischer curve (more power means more convection and lower segregation). In the future a more careful analysis of the two-dimensional data will be compared to a numerical model of the lamp.

Acknowledgements

The authors are grateful to J.J.A.M. van der Mullen and M. Haverlag for the discussion about the theory of the lamps, M. van Kemenade for his contribution to developing the measurement method and Senter-Novem (project EDI 03146) for funding the research.

3

Axial segregation in metal-halide lamps under varying gravity conditions during parabolic flights

Abstract.

Metal-halide lamps have high efficiencies. These lamps often contain rare-earth additives (in our case dysprosium iodide) which radiate very efficiently in the visible spectrum. Colour separation is a problem in these lamps; this is caused by axial segregation of these additives as a result of diffusion and convection. To vary the effect of convection, parabolic flights were performed with micro-gravity ($0g$) and hyper-gravity ($\sim 1.8g$) phases. During these flights, the atomic dysprosium density was measured by means of laser absorption spectroscopy. In addition, the lamp voltage and wavelength integrated light output of the lamp, which are strongly influenced by the total amount of Dy in the lamp, were measured. The Dy density, axial segregation and light output are dependent on the gravity. The dynamic lamp behaviour during the parabolas was investigated: the dysprosium density and lamp voltage followed the gravity variations. When entering the micro-gravity phase, the axial diffusion time constant is the slowest time constant; it is proportional to the mercury pressure in the lamp.

This chapter has been adapted from [A.J. Flikweert, M. van Kemenade, T. Nimalasuriya, M. Haverlag, G.M.W. Kroesen and W.W. Stoffels, *Axial segregation in metal-halide lamps under varying gravity conditions during parabolic flights*, J. Phys. D: Appl. Phys. **39** (2006) 1599–1605].

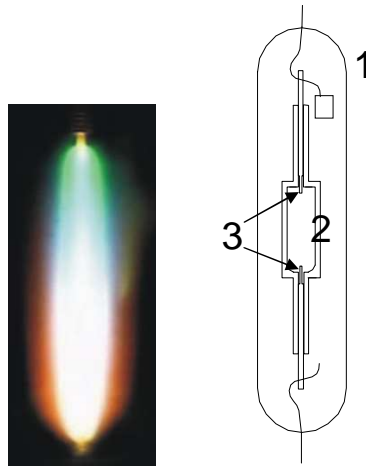


Figure 3.1: (printed in colour in figure 1.3) Left: picture of a MH lamp burner (real size 8 mm x 20 mm); colour separation is clearly visible. Right: schematic picture of the lamp: (1) outer bulb; (2) burner with height 20 mm and diameter 8 mm; (3) electrodes, distance between the both electrodes ~ 18 mm.

3.1 Introduction

Metal-halide (MH) lamps, which are high intensity discharge (HID) lamps, have a high efficiency (up to 40%) [3, 21–25]. They contain a buffer gas (mercury) and often rare-earth additives that act as the prime radiator in the visible spectrum. The rare-earth additive is dosed as a salt; the rare-earth vapour above the salt pool is saturated. When burning vertically, the lamp used by us has a non-uniform light output because of segregation of the additives. This colour separation and a schematic picture of the lamp are shown in figure 3.1 [32, 43].

The colour separation [28] is caused by the non-uniform distribution of the rare-earth additives. This distribution originates from convection and diffusion phenomena in the lamp [32, 34, 43, 50]. Convection is caused by gravity and therefore the lamp has been investigated under micro-gravity conditions during parabolic flights and at the International Space Station, where no convection is present in the lamp [41, 51, 52].

To get more insight in the flow phenomena and segregation in the lamp, absorption measurements of atomic dysprosium have been carried out during parabolic flights. During these flights, several parabolas are performed. Each parabola consists of several phases. At the start of a parabola, the gravity is changed from normal ($1g$) to hyper-gravity ($\sim 1.8g$): the airplane pulls up. The next phase is free fall: micro-gravity ($0g$). The final phase is again hyper-gravity. After this parabola, normal gravity returns when flying horizontally.

The dynamic lamp behaviour during the parabolic flights has been investigated [43], the goal being to find a qualitative relationship between the gravity and the Dy density. To understand this dynamic behaviour, one needs a model. The theory propounded by E. Fischer [28] will be used here.

The atomic dysprosium density has been measured at one axial position of the lamp; this gives a measure for axial segregation. Furthermore, the lamp voltage has been measured—this gives a measure for the conductivity of the plasma and the total amount of dysprosium in the plasma. Finally, an integrating sphere has been used to measure the integrated light output by the lamp.

First the theory behind the lamps is introduced. Next the experimental setup is discussed briefly: the lamp, the parabolic flights and the laser absorption technique. The atomic dysprosium density (at a certain axial position) and the lamp voltage are presented for three lamps with varying Hg content during the different phases (normal gravity, hyper-gravity, micro-gravity) of the parabola. Finally, the results obtained by integrated light output measurements are presented.

3.2 Theory

The theory of segregation in infinitely long MH lamps has been propounded by E. Fischer [28]. For our lamp with a limited burner height of 20 mm and diameter of 8 mm and containing DyI₃ as the rare-earth additive, the theory has been described in a prior publication [32]. For the reader's convenience it will be summarized here.

3.2.1 Radial segregation

Because of the large temperature gradient between the wall (~ 1200 K) and the centre of the burner (~ 5500 K) [29], mainly atoms are present at the centre while at the wall molecules dominate. In addition, at the very centre of the burner, where the temperature is high, Dy atoms are ionized. Due to the different diffusion velocities of atoms, molecules and ions, the light particles in the hotter centre diffuse faster than the heavy molecules near the cooler wall. This results in a hollow radial profile of the total dysprosium concentration (Dy in any chemical form): the so-called radial segregation. Note that this is in addition to the already lower gas density defined by the ideal gas law $p = nkT$. The profiles for the MH lamp have already been presented in literature [32], where the hollow radial profile is clearly seen.

Figure 3.2 shows the total Dy density as a function of the radial position for two situations with an equal amount of Dy in the lamp: in situation B the radial segregation is stronger than in situation A. Note that near the centre dysprosium is mainly present in the form of atoms and ions, whereas at the wall dysprosium is mainly present in the form of molecules. Therefore, for stronger radial segregation, the radially averaged atomic Dy density decreases.

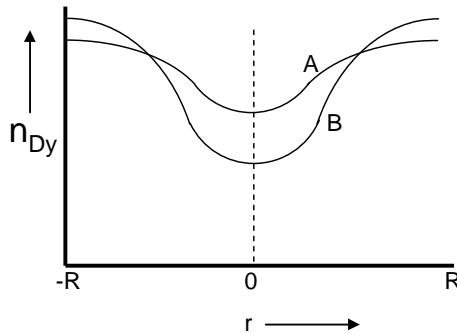


Figure 3.2: Elemental Dy density as a function of radial position. For equal total Dy amounts, in situation B the radial segregation is stronger than in situation A.

At a sufficiently high salt pool temperature, dysprosium is the prime radiator in the lamp. When the amount of Dy increases, the radiation loss is increased. The Dy atoms are responsible for the most of the radiation [41], causing radiation loss at the flanks of the discharge where most of the Dy atoms are present. This results in contraction of the arc. The region around the centre where the temperature is high enough for ionization of Dy becomes smaller. The arc channel, which is the zone where the ionization is high enough for conduction, becomes narrower. Because of the contraction, the resistance of the plasma increases. When the input power P is kept constant, the lamp input voltage depends on the resistance R of the plasma: $V = \sqrt{PR}$. Thus more Dy means a higher resistance R and means therefore a higher voltage V .

3.2.2 Convection and axial segregation

In addition to radial segregation, convection is also present in the lamp: the gas in the hotter centre moves upwards while the gas at the wall moves downwards. As discussed in section 3.2.1, the maximum of the elemental Dy density lies near the wall. Because of this, a net downward flow of Dy results in axial segregation [21, 22]: the atomic Dy density is higher near the bottom of the burner. This has also been shown by earlier measurements on the same type of lamp [32].

E. Fischer [28] predicts for an infinitely long lamp an exponential decrease of the axial atomic Dy density $n_{\text{Dy}}(z)$ with increasing height z in the plasma:

$$n_{\text{Dy}}(z) = n_{\text{Dy},0} \exp(-\lambda z), \quad (3.1)$$

where the parameter λ is a measure for the axial segregation and $n_{\text{Dy},0}$ is the atomic Dy density at the bottom of the burner.

The axial segregation (colour separation) is a result of the balance between diffusion and convection. Good mixing in the lamp occurs in two limiting cases: when there is

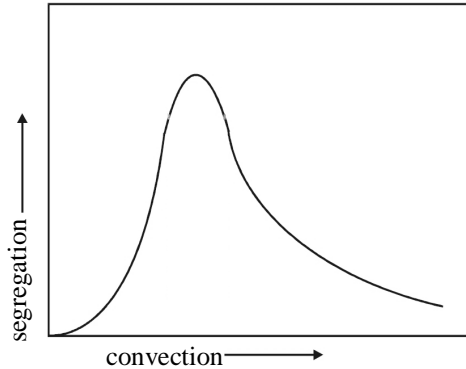


Figure 3.3: The (qualitative) Fischer curve [28]: axial segregation parameter λ of the lamp as a function of the amount of convection. The amount of convection increases with the gravity and is also dependent on the input power and the aspect ratio of the burner. The order of magnitude of λ is 0.20 mm^{-1} [32].

no convection, and when there is extremely high convection. Somewhere in between, the segregation parameter λ has a maximum. The convection increases among other things with the gravity. The Fischer curve (segregation parameter as a function of gravity) is shown in figure 3.3.

In figure 3.4 the dysprosium density distribution over the length of the lamp is shown schematically for various values of the axial segregation parameter λ . When measuring the dysprosium density at a particular axial position, the density varies with the amount of segregation. The density at the lower electrode (near the cold spot) is constant for a fixed temperature. When no axial segregation is present (situation A), one measures a higher density than when the lamp shows strong axial segregation (situation C).

3.2.3 Convection time constants

In order to understand the dynamic lamp behaviour when turning the gravity ‘off’, in our case switching from hyper-gravity to zero gravity during parabolic flights (section 3.1), we estimate several typical time constants in the lamp. The three time constants that are estimated are the convection time constant, the radial diffusion time constant and the axial diffusion time constant.

The convection in the lamp is driven by gravity. When switching to micro-gravity at $t = 0 \text{ s}$, the driving force of the convection flow disappears. The present kinetic energy of the convective flow is dissipated by viscous dissipation [53]. The kinetic energy per unit volume is equal to $\frac{1}{2}\rho v^2$, whereas the viscous dissipation per unit volume and per

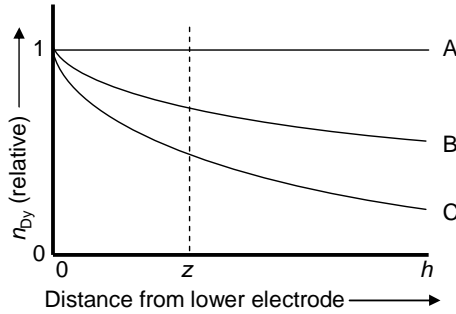


Figure 3.4: The radially integrated total Dy density (in any chemical form) as a function of the axial position in the lamp burner (bottom at 0 and top at h), for different values for the axial segregation parameter λ (infinitely long lamp). At situation A no axial segregation is present, whereas at situation C strong axial segregation is present. When the Dy density at the lower electrode is fixed (normalized to 1), the total Dy density measured at the dashed position z is a measure of the axial segregation parameter λ .

unit time is given by $\mu \cdot \left(\frac{dv}{dr}\right)^2$. In these expressions, v is the flow velocity, r is the radial position, μ is the dynamic viscosity ($\text{kg m}^{-1} \text{s}^{-1}$) and ρ is the density of the bulk gas in the burner (mercury in our case). For the total energy dissipated by viscous dissipation, one has to integrate the viscous dissipation (per unit volume and per unit time) over time.

It is assumed that the flow velocity decays exponentially from $t = 0$ s:

$$v(r, t) = \begin{cases} v_0(r) & \text{for } t < 0 \\ v_0(r) \exp\left(-\frac{t}{\tau_{\text{conv}}}\right) & \text{for } t \geq 0 \end{cases}, \quad (3.2)$$

where τ_{conv} is a measure for the time the convection flow persists after switching off the gravity. By setting the kinetic energy and the viscous dissipation (integrated over time) equal and using equation (3.2), one gets for the convection time constant τ_{conv} :

$$\frac{1}{2} \rho v_0^2(r) = \int_{t=0}^{\infty} \mu \left(\frac{dv_0(r)}{dr}\right)^2 \exp\left(-\frac{2t}{\tau_{\text{conv}}}\right) dt \Leftrightarrow \tau_{\text{conv}} = \frac{\rho v_0^2}{\mu (dv_0(r)/dr)^2}. \quad (3.3)$$

The convection speed at the axis of the lamp is about 0.20 m s^{-1} and near the wall -0.06 m s^{-1} [54]. When the ratio $v(r)/(dv/dr)$ is assumed to be constant under different conditions (gravity, pressure, input power), for our conditions (table 3.1) this results in convection time constants of less than 1 s as given in table 3.2.

Table 3.1: Values used for calculating time constants.

R_{burner}	4.0 mm
l_{burner}	20.0 mm
T_{eff}	3000 K [53]
n (5 mg Hg)	$1.50 \times 10^{25} \text{ m}^{-3}$
n (7.5 mg Hg)	$2.25 \times 10^{25} \text{ m}^{-3}$
n (10 mg Hg)	$1.50 \times 10^{25} \text{ m}^{-3}$

Table 3.2: Convection time constants for different amounts of Hg.

mg Hg	τ_{conv} (s)
5.0	0.07
7.5	0.11
10.0	0.14

3.2.4 Diffusion time constants

Two other time constants are the radial diffusion time constant and the axial diffusion time constant. For the diffusion time of a particle only the collisions with the bulk (mercury) are regarded. The diffusion time τ_{diff} is given by [55]

$$\tau_{\text{diff}} = \frac{l^2}{D}, \quad (3.4)$$

with l the typical length scale. For radial segregation this is approximately the radius ($l = R$), whereas for axial segregation the height of the burner is taken ($l = h$). The diffusion coefficient D is estimated by (hard-sphere scattering) [55]

$$D = \frac{k_b T_{\text{eff}}}{m_r \nu}. \quad (3.5)$$

Here k_b is the Boltzmann constant, T_{eff} is the effective temperature, m_r is the reduced mass (of mercury and the particle) and ν is the collision frequency of the particle and Hg.

Using the values in table 3.1 and the effective radii of the particles in table 3.3, the diffusion time constants are calculated and presented in table 3.4.

Another time constant may be the warming up of the burner when varying the gravity. The burner consists of quartz of 1 mm thickness; its heat capacity is 1.4 J K^{-1} [57]. With a rough estimate of a 100 K temperature change and taking 50% of the input power for heating the burner, one obtains a warming-up time of ~ 2 s. The real time constant is probably (much) smaller (lower temperature change), so the warming-up time constant is ignored.

Table 3.3: Effective particle radii for calculating time constants [56].

Species	Radius ($\times 10^{-10}$ m)
Dy	2.23
DyI	3.50
DyI ₂	4.25
DyI ₃	4.63
Dy ₂ I ₆	5.50
Hg	2.09

Table 3.4: Diffusion time constants along radius and axis for several particles.

	mg Hg	Dy (s)	DyI (s)	DyI ₂ (s)	DyI ₃ (s)	Dy ₂ I ₆ (s)
Along	5.0	0.34	0.68	1.00	1.22	1.80
the	7.5	0.52	1.03	1.51	1.83	2.70
radius	10	0.69	1.37	2.01	2.44	3.60
Along	5.0	8.6	17.1	25.1	30.5	45.0
the	7.5	12.9	25.6	37.7	45.8	67.5
axis	10	17.2	34.2	50.2	61.1	90.1

The convection time constants are much smaller than the axial diffusion time constants. This means that when entering the micro-gravity phase from the hyper-gravity phase, the convection flow disappears fast and the speed of stabilization of the dysprosium distribution is determined by the axial diffusion time constant. This time constant is proportional to the mercury pressure.

3.3 Experimental setup

3.3.1 The lamp

The lamp that is measured contains Hg as buffer gas, 300 mbar Ar/Kr⁸⁵ as a starting gas and 4.2 mg DyI₃ as a salt additive. A schematic picture of the lamp is shown in figure 3.1. The amount of Hg is varied; lamps with 5, 7.5 and 10 mg of Hg are measured. The ballast (Philips HID-DynaVision LA 0307, square wave of 125 Hz) delivers a constant power of 150 W. The lamp voltage is read out by the ballast.

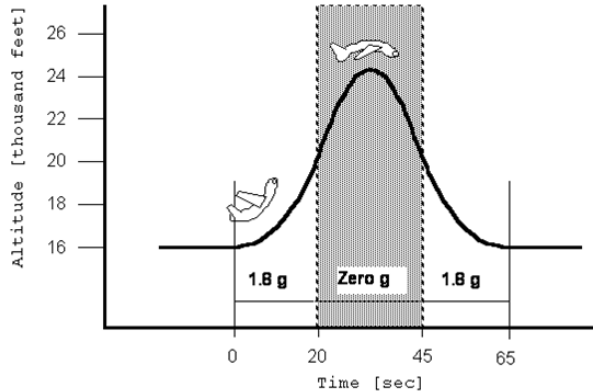


Figure 3.5: Parabolic sequence: hyper-gravity (~ 20 s), micro-gravity (the main phase, ~ 25 s) and again hyper-gravity (~ 20 s).

3.3.2 Parabolic flights

The lamp was measured under micro-gravity conditions during the parabolic-flight campaign of the European Space Agency (ESA) in June 2004 [40]. During each flight, 31 parabolas were performed. In figure 3.5 the height of the airplane and the gravity are shown schematically. Each parabola starts with hyper-gravity: the pull-up phase. The second phase is the injection phase. In this phase of about 25 s all forces are compensated: zero gravity is achieved. The last phase of the parabola is a hyper-gravity phase where the airplane pulls out of the free fall.

In figure 3.6 an example is given of the effective g forces during one parabola. As is seen in this figure, the hyper-gravity phases are not well defined. The micro-gravity phases are controlled very well; therefore we will focus on the micro-gravity phases.

3.3.3 Laser absorption spectroscopy

To get insight into the axial segregation, we measured the radially averaged density of ground state dysprosium using laser absorption spectroscopy. The measurement technique has been described in detail in section 2.3 [32].

A tunable diode laser (Sacher TEC 500 645-5, typical line width ≤ 3 fm) scans a small wavelength range (0.17 nm) around the absorption wavelength $\lambda = 642.19$ nm. The transition probability of this transition is $1.615 \times 10^5 \text{ s}^{-1}$ [44, 45]. This line is pressure broadened with a width of around 40 pm (experimentally determined).

In figure 3.7 a schematic overview of the setup for the laser absorption measurements on the lamp is given. The laser beam (height ~ 1 mm) is transformed to a parallel sheet

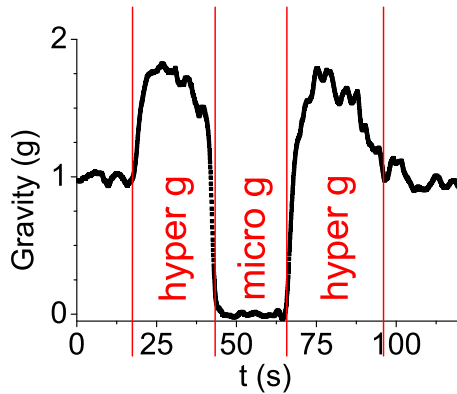


Figure 3.6: Gravity as a function of time during one parabola; the start of the time axis is chosen arbitrary. The micro-gravity and hyper-gravity phases are indicated.

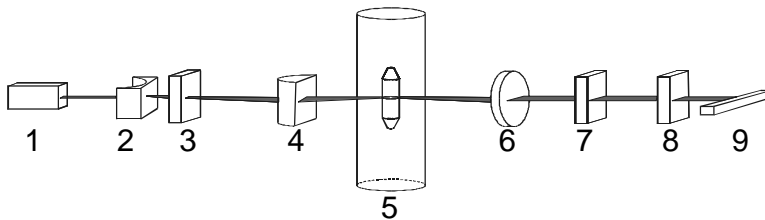


Figure 3.7: Schematic overview of the absorption setup used to measure the ground state Dy density in a MH lamp: (1) diode laser; (2) cylindrical lens, $f = -12.7$ mm; (3) cylindrical lens, $f = +62.9$ mm; (4) lamp; (5) spherical lens, $f = +100$ mm; (6) interference filter; (7) diode array.

inside the lamp burner by two cylindrical lenses. After the beam passes the plasma, it converges to a parallel beam, then passes an interference filter and hits the diode array (32 evenly spaced photodiodes). Each detector channel is converted into a lateral position x ; in this way a lateral absorption profile is obtained.

The measurement method is shown in figure 3.8. For each lateral position the laser intensity is measured for lamp-off and lamp-on (corrected for dark current). The indicated lamp emission is independent of the laser wavelength. From these curves the absorption and subsequently the line-of-sight dysprosium density are calculated. Finally the data are converted into a radially averaged dysprosium density profile n_{Dy} [29, 32, 48, 49].

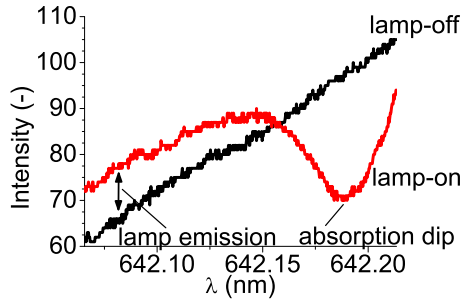


Figure 3.8: Measured laser intensity as a function of wavelength λ at a particular lateral position for lamp-on and lamp-off. The absorption dip (at 642.19 nm) and lamp emission are indicated. The intensity is given in arbitrary units.

3.3.4 Integrated light emission setup

In order to measure the total lamp emission, the lamps are placed in an integrating sphere, which collects and homogenizes the total light output of the lamp [51]. This light is then detected by a photodiode supplied with a suitable optical filter, simulating human eye sensitivity.

The integrating sphere measurements have been carried out on the same lamps as the Dy density and voltage measurements, but at a different parabolic flight campaign.

3.4 Results

Three different lamps were measured during parabolic flights. The amounts of mercury are different, 5, 7.5 and 10 mg, which correspond to 6, 9 and 12 bar, respectively, for $T_{\text{eff}} = 3000$ K (Table 3.1).¹ The radially averaged ground state atomic dysprosium density was measured at 5 mm above the lower electrode. At the same time, the lamp voltage was measured. The measurements of the Dy density and lamp voltage are presented. Next, the results of the integrated light emission measurements are presented. The time constant when entering the micro-gravity phase is presented and discussed.

The atomic Dy density, lamp voltage, gravity and wavelength integrated light output during a parabola are shown in figures 3.9–3.13; the start of the time scale was chosen arbitrary during a $1g$ phase. The Dy density and lamp voltage have been normalized: the density and voltage have been set to unity at $1g$. In the graphs, the micro-gravity phase and hyper-gravity phases are indicated. At normal gravity, the

¹When the cold zones behind the electrodes are taken into account, the pressures are around 5, 7.5 and 10 bar respectively.

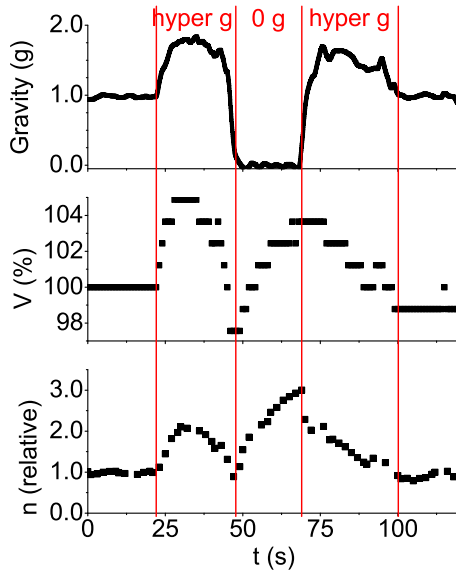


Figure 3.9: Radially averaged Dy density, lamp voltage and gravity as functions of time at 5 mg Hg (6 bar).

order of magnitude of the atomic Dy density was $\sim 10^{21} \text{ m}^{-3}$ and the lamp voltage was $\sim 80 \text{ V}$, $\sim 100 \text{ V}$ and $\sim 120 \text{ V}$ for 5 mg, 7.5 mg and 10 mg Hg, respectively.

It was observed that the Dy density varies with gravity. In the hyper-gravity phase, the measured (integrated) Dy density increased. When switching from hyper-gravity to micro-gravity the Dy density decreased rapidly ($\sim 1 \text{ s}$) followed by a slow density increase. In the second hyper-gravity phase, the density increased again.

The lamp voltage is a measure for the total amount of dysprosium in the gas phase in the lamp and thus of the degree of axial segregation in the lamp, as explained in section 3.2.1. This was also observed in figure 3.9–3.11: the lamp voltage follows the same trend as the Dy density.

The integrated light emission in figures 3.12 and 3.13 follows the trends in the radially averaged Dy density and the voltage over the lamp closely. The integrating sphere measurements have been carried out on the same lamps as the absorption and voltage measurements, but at a different parabolic flight campaign. This means that the measurements on the same lamp are reproducible.

The increase in Dy density and the increased light emission at the first hyper-gravity phase can be understood by a better mixing (right-hand side of the Fischer curve (figure 3.3) and thus less axial segregation (situation C to B in figure 3.4) and increasing the total amount of radiating Dy in the arc. The positions in the Fischer curve correspond

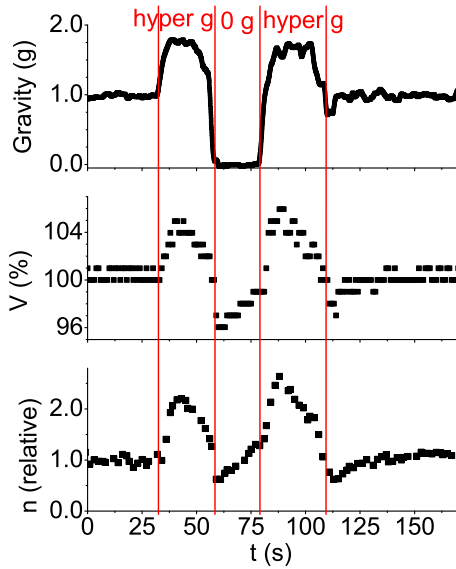


Figure 3.10: Radially averaged Dy density, lamp voltage and gravity as functions of time at 7.5 mg Hg (9 bar).

to those observed in other measurements on the same type of lamp [32, 41].

The gravity data in figures 3.9–3.11 show that only the micro-gravity phase is well defined. During the hyper-gravity phases, the gravity was not constant. Note that the Dy density and lamp voltage closely followed the gravity variations; an example is shown in figure 3.11. A higher gravity means a higher Dy density and thus less axial segregation. This means that above 1g we are at the right-hand side of the maximum in the Fischer curve (figure 3.3).

When switching from hyper-gravity to micro-gravity, one observes a steep decline in the Dy density. Several time constants play a role right after entering the micro-gravity phase (sections 3.2.3 and 3.2.4); the convection time constant is the smallest (~ 0.1 s) and the axial diffusion time constant is the largest (~ 30 s). The radial diffusion time constant is ~ 1 s. When the micro-gravity phase is entered, the radial segregation increases. The total amount of dysprosium (in any chemical form) remains more or less constant due to the fact that the axial diffusion is slow compared to the radial diffusion time constants. Atoms are mainly present around the hot centre (section 3.2.1), so more radial segregation means fewer Dy atoms around the centre and (slightly) more DyI_x molecules near the wall. Only atoms have been measured, so the radially averaged Dy density decreases.

During the micro-gravity phase, the density was increasing because the axial se-

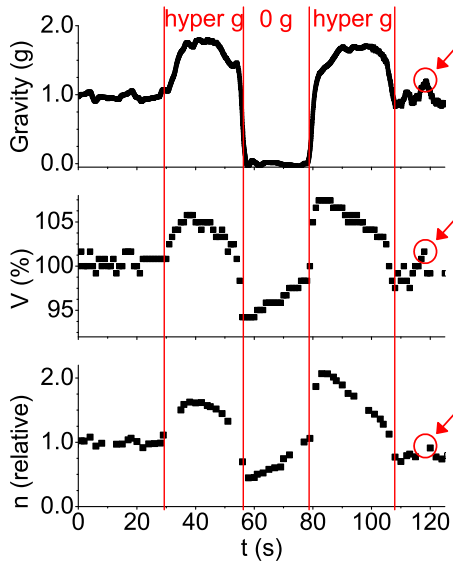


Figure 3.11: Radially averaged Dy density, lamp voltage and gravity as functions of time at 10 mg Hg (12 bar). The Dy density and lamp voltage closely follow the gravity variations; an example is indicated by the circles.

gregation tended to disappear (towards situation A in figure 3.4; left-hand side of the Fischer curve in figure 3.3). The total amount of atomic dysprosium also increases with decreasing axial segregation (the area under the curves shown in figure 3.4). This also explains the increased light output observed in figures 3.12 and 3.13.

The micro-gravity phase is the only well-defined phase of the parabola; therefore only at this part (rising Dy density) has the time constant been fitted. The time constants were determined from figures 3.9–3.11; here a linear fit was applied. In figure 3.14 the results are plotted for the three different lamps. The trend and the order of magnitude of the time constants correspond to the values presented in table 3.4.

At the end of the micro-gravity phase, the lamp was still not in equilibrium: especially for 7.5 and 10 mg Hg the time constants are greater than the duration of the micro-gravity phase (~ 20 s). Therefore the lamps have also been investigated in space in the International Space Station (ISS) [41].

When switched from the micro-gravity phase to the second hyper-gravity phase, a steep increase was observed. The atomic Dy density at the end of the micro-gravity phase is determined by the Hg pressure and the axial diffusion time constant. In the second hyper-gravity phase the new equilibrium was reached fast (convection time constant ~ 0.1 s); the Dy density was again higher than for normal gravity, due to less

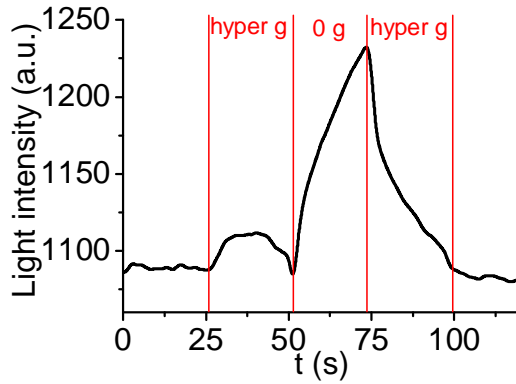


Figure 3.12: Integrated light emission of the lamp burning in vertical position with 5 mg Hg (6 bar) at 150 W as a function of time during one parabola [58]. The trend is similar to the density and voltage measurements presented in figure 3.9.

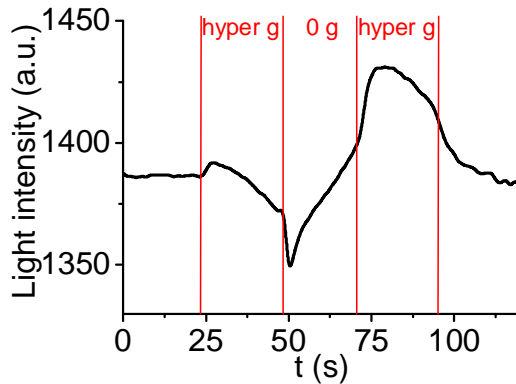


Figure 3.13: Integrated light emission of the lamp burning in vertical position with 10 mg Hg (12 bar) at 150 W as a function of time during one parabola [58]. The trend is similar to the density and voltage measurements presented in figure 3.11.

radial segregation and an overall higher Dy density in the lamp.

3.5 Conclusions

The dynamic behaviour of three lamps during parabolic flights (different amounts of mercury) was investigated. The radially averaged atomic dysprosium density was mea-

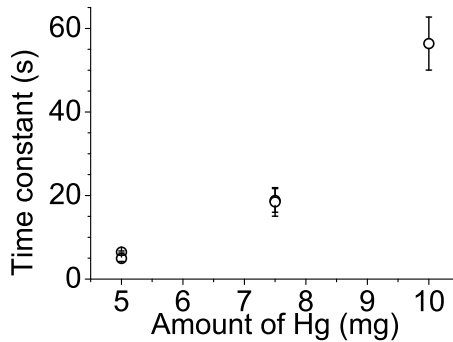


Figure 3.14: Time constants at the micro-gravity phase for different amounts of Hg; 5, 7.5 and 10 mg Hg correspond to 6, 9 and 12 bar, respectively.

sured by means of laser absorption spectroscopy. Furthermore the lamp voltage was measured, which turns out to be a measure for the total amount of dysprosium in the lamp.

By changing the gravity, the amount of convection was varied. The axial segregation is inversely proportional to the measured atomic dysprosium density. The lamps follow the qualitative description presented by E. Fischer.

Three processes with different time constants play a role when switching from hyper-gravity to micro-gravity. The axial diffusion time constant is the slowest time constant (~ 30 s), which is proportional to the amount of mercury, as predicted by the theory. As a result, at the end of the micro-gravity phase the lamp is still not in equilibrium. Therefore the lamps have also been tested in the ISS.

The total light output of a metal-halide lamp strongly depends on the gravity conditions. The light emission decreases when the axial segregation increases. The results for the integrated light emission measurements are in agreement with the Dy density measurements performed by laser absorption spectroscopy and the lamp voltage measurements.

Acknowledgments

The authors are grateful to all participants in the ARGES project for their contributions, ESA [40] and Novespace [59] for the parabolic flight campaigns and the g level data, and Senter-Novem (project EDI 03146) and the Dutch Ministries of Research and Education as well as Economic Affairs for funding the research.

4

Imaging Laser Absorption Spectroscopy of the metal-halide lamp in a centrifuge (1–10*g*)

Abstract.

Imaging Laser Absorption Spectroscopy (ILAS) was performed on a metal-halide lamp under hyper-gravity conditions in a centrifuge (acceleration ranging from 1 to 10*g*). Diffusive and convective processes in the arc discharge lamp cause an unwanted non-uniform distribution of the radiating metal additive, which results in colour separation. Convection is induced by gravity, and measuring under different apparent gravity conditions aids the understanding of the flow processes in the lamp. The centrifuge was built to investigate the lamp under varying apparent gravity conditions. The metal additive density distribution in the lamp is measured by ILAS. In this novel diagnostic technique the laser beam is expanded, so the absorption in the complete plasma volume is imaged simultaneously.

This chapter has been adapted from [A.J. Flikweert, T. Nimalasuriya, G.M.W. Kroesen and W.W. Stoffels, *Imaging Laser Absorption Spectroscopy of the metal-halide lamp in a centrifuge (1–10*g*)*, Plasma Sources Sci. Technol. **16** (2007) 606–613].

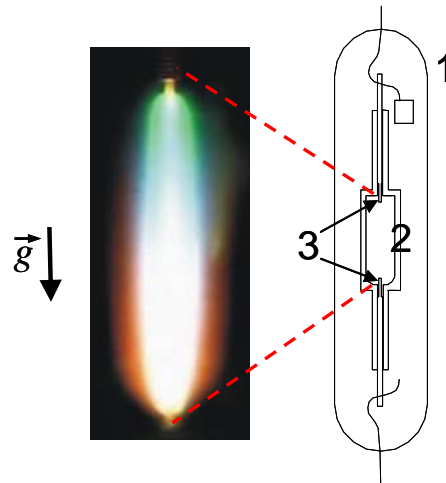


Figure 4.1: (printed in colour in figure 1.3) Left: picture of the burner of a MH lamp (real size 8 mm x 20 mm; filling 10 mg Hg and 4 mg DyI₃); colour separation is clearly visible. The exponential decay of the radiating particle (white) towards the top has a maximum when the convection and diffusion are of the same order of magnitude. Right: schematic picture of the lamp, (1) outer bulb; (2) burner with height 20 mm and diameter 8 mm; (3) electrodes, distance between both electrodes ~18 mm.

4.1 Introduction

Many plasmas have an axis of symmetry. They are cylindrical symmetric but inhomogeneous in the axial direction. A useful diagnostic tool to investigate these plasmas is Imaging Laser Absorption Spectroscopy (ILAS). Laser absorption spectroscopy has been used in earlier experiments (chapters 2 and 3) to measure the particle density distribution in a plasma [32, 33]. However, in order to image the absorption in the complete plasma volume simultaneously (2D), in the novel ILAS setup laser beam expansion is used, so every part of the laser beam samples a different part of the plasma. This chapter outlines this new technique of laser absorption spectroscopy.

The novel ILAS technique is applied on a metal-halide (MH) lamp. This lamp is a compact high-intensity light source with a high luminous efficacy and a good colour rendering index. It has a high efficiency (up to 40%) compared with present (compact) fluorescent lamps [3, 21–26]. The arc discharge lamp contains a buffer gas (mercury) and (a combination of) metal additives (for instance Na, Ce, Dy), which are dosed as metal-halide salts. After ignition of the lamp, the salt evaporates and enters the arc. The metal additives act as the prime radiator in the visible spectrum. The local density distribution of the additive is determined by convective and diffusive processes,

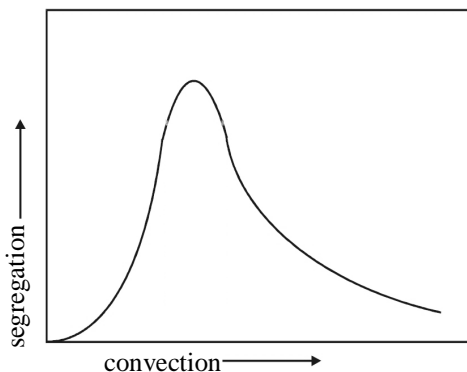


Figure 4.2: The Fischer curve [28, 33]: axial segregation (λ) of the metal additive in an infinitely long lamp as a function of the amount of convection. Convection is induced by gravity. In our experiment, the amount of convection is increased by increasing the gravity.

which cause an unwanted non-uniform distribution of the additives in the lamp. The processes result in a segregation of colours [27, 28, 32–34, 38, 41]: so-called demixing. The colour separation and a schematic picture of the lamp are shown in figure 4.1.

The large temperature gradient between the wall (~ 1200 K) and the centre of the burner (~ 5500 K) [29] leads to the situation that atoms are mainly present at the centre while molecules dominate at the wall. In addition, the metal atoms are partially ionized at the very centre of the burner because of the high temperature. The diffusion velocities of atoms, molecules and ions (ambipolar diffusion) are different. The light particles at the hot centre diffuse outwards faster than the heavy molecules near the cooler wall diffuse inwards. This difference in diffusion times results in a hollow radial profile of the elemental metal relative concentration (the metal additive in any chemical form) in addition to the already lower gas density defined by the ideal gas law $p = nkT$; this mechanism is called radial segregation. Due to radial segregation, the maximum of the elemental metal relative concentration lies near the wall. The second mechanism, convection, causes the hot gas at the centre to move upwards, whereas the gas near the cooler wall moves downwards. The combination of radial segregation and convection results in a net downward transport of the metal additive which is balanced by an axial density gradient: the so-called axial segregation [21, 22, 32].

When the convective and diffusive processes are of the same order of magnitude, axial segregation of the metal additive occurs because of the competition between these two processes. In the two limiting cases, when there is no convection, or when there is extremely high convection, good mixing and thus no axial segregation is achieved (figure 4.2).

Because the convection is induced by gravity, the lamp was investigated at micro-gravity in the International Space Station (ISS) [41] and at micro-gravity and hyper-gravity ($\sim 1.8g$) during parabolic flights [33, 43, 51, 52]. Measuring under different gravity conditions aids the understanding of the diffusive and convective processes. However, during the parabolic flights micro-gravity and hyper-gravity were obtained for a period of only about 20 s. This is not enough time for the arc to stabilize. A centrifuge was built for this purpose: to investigate the lamp in an environment where stable arc conditions are ensured. The centrifuge can go up to $10g$, thus the lamp can be investigated under even higher gravity conditions than during the parabolic flights. The measurement techniques used in the centrifuge are emission spectroscopy and ILAS.

The structure of this chapter is as follows. Section 4.2 describes the centrifuge. The diagnostics are described in section 4.3. Section 4.4 presents some first results of the ILAS measurements on the lamp in the centrifuge. Finally, section 4.5 gives conclusions and some recommendations for future work.

4.2 The centrifuge

A centrifuge was built as a tool to investigate the MH lamp [27] under hyper-gravity conditions up to $10g$. The centrifuge consists of a pivot, an arm connected to the pivot and at the end of the arm a gondola, in which the lamp is placed. Furthermore, the gondola contains the measurement techniques and electronics. In figure 4.3 the schematic representation of the centrifuge is shown; the coordinate system of the lamp in the gondola is indicated (\vec{z} is parallel to the lamp axis). The total diameter at maximum swing-out of the gondola is close to 3 m; the maximum rotation frequency is ~ 1.5 Hz. Figure 4.4 shows the dimensions of the centrifuge and the acceleration vectors at the position of the lamp.

4.2.1 Acceleration

The total acceleration vector experienced by the lamp depends on the rotation frequency of the centrifuge. When the rotation frequency increases, the distance between the lamp and the axis of the centrifuge increases. When this is taken into account, the size of the centrifugal acceleration vector \vec{a}_r (figure 4.4) is given by

$$a_r = \omega^2 \cdot (r_1 + r_2 \sin \phi). \quad (4.1)$$

Here ω is the angular frequency of the centrifuge, r_1 is the arm length of the centrifuge, r_2 is the distance between the gondola hinge point and the centre of the lamp and ϕ is the angle of swing-out of the gondola. Using the relation for the magnitude of the resultant acceleration vector

$$a_{\text{tot}} = \sqrt{a_r^2 + g_z^2}, \quad (4.2)$$

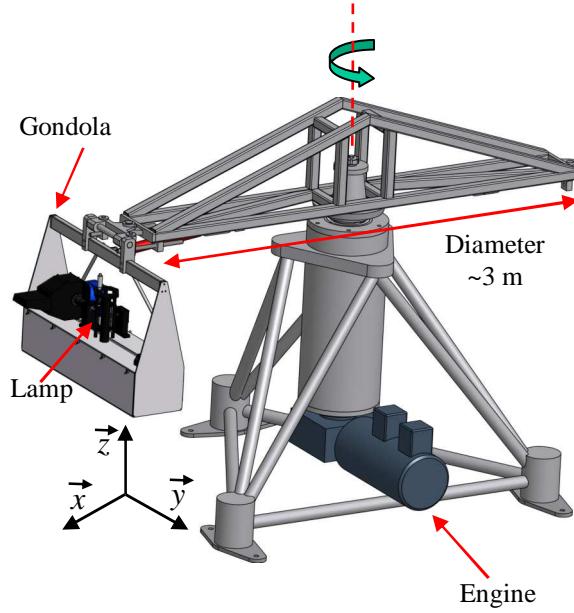


Figure 4.3: Schematic representation of the centrifuge. The setup consists of a pivot, an arm and the gondola that contains the lamp and diagnostic equipment (figures 4.8 and 4.11). The coordinate system shown is that of the lamp in the gondola; \vec{z} is parallel to the lamp axis.

where g_z is the magnitude of the gravity on earth, one gets the following relation:

$$a_{\text{tot}}^2 - g_z^2 = \omega^4 \cdot \left(r_1 + \frac{r_2}{a_{\text{tot}}} \sqrt{a_{\text{tot}}^2 - g_z^2} \right)^2. \quad (4.3)$$

Ideally \vec{a}_{tot} is parallel to the lamp axis. Therefore it is necessary that the centre point of mass of the gondola is located along the axis of the lamp. The resultant acceleration vector always acts in the right direction when the gondola swings radially outwards. Looking at figure 4.4, this means that $a_{\text{tot}} = a_z$ (\vec{a}_z is parallel to the lamp axis) and thus $a_x = a_y = 0$. The vector \vec{a}_x is along the optical path and \vec{a}_y is perpendicular to \vec{a}_x and \vec{a}_z . To verify the direction of the acceleration vector \vec{a}_{tot} , the lamp is substituted by an accelerometer (Endevco 7596A-30). The sizes of the three vectors \vec{a}_x , \vec{a}_y and \vec{a}_z are measured as functions of the rotation frequency of the centrifuge $f = \omega/2\pi$. The calibration curve for \vec{a}_z is shown in figure 4.5. Figure 4.6 shows the curves for \vec{a}_x and \vec{a}_y . In these figures the unit G is defined as 9.81 m s^{-2} . The accelerations in \vec{x} and \vec{y} direction are less than 0.13 G and 0.07 G, respectively. The maximum ratios between the accelerations in the \vec{x} and \vec{y} directions and the acceleration

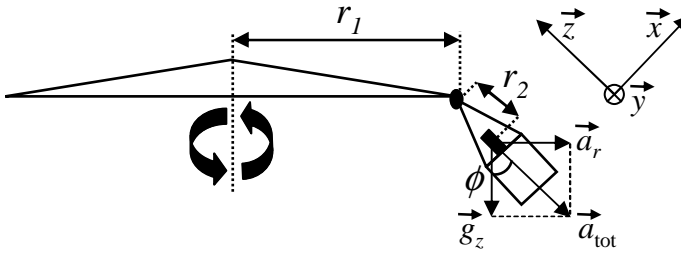


Figure 4.4: Schematic representation of the centrifuge arm with gondola. The dimensions are $r_1 = 1.0975$ m and $r_2 = 0.3485$ m. When the centrifuge is rotating, the gondola swings out with an angle ϕ . The acceleration vectors at the position of the lamp (\vec{g}_z , \vec{a}_r , \vec{a}_{tot}) are indicated; the coordinate system relative to the lamp (from figure 4.3) is also indicated.

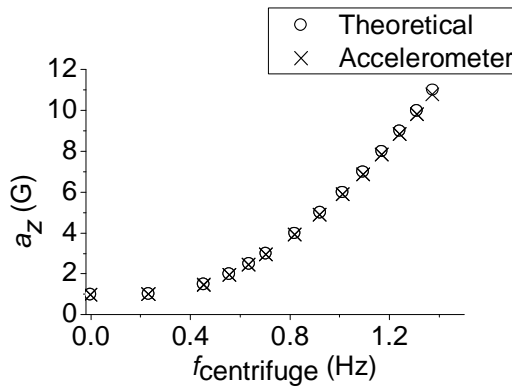


Figure 4.5: Theoretical (equation (4.3)) and measured acceleration at the position of the lamp. The acceleration a_z is measured parallel to the lamp axis, as a function of the centrifuge rotation frequency.

a_z are less than 5% below $5g$. At $10g$ the accelerations in the \vec{x} and \vec{y} directions are less than 1%. A slight variation in the acceleration occurs along the lamp axis, because the top of the lamp is closer to the centre point of the centrifuge. However, this is only a variation of 0.7% and is therefore not taken into account. Calibration with an accelerometer thus shows that the acceleration vector that acts on the lamp is always parallel to the lamp axis.

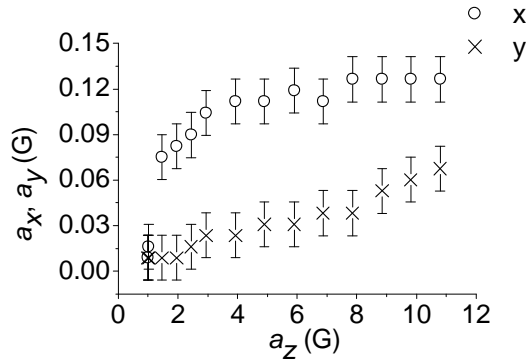


Figure 4.6: Accelerations a_x and a_y (perpendicular to the lamp axis) as a function of a_z (parallel to the lamp axis), measured at the lamp axis. The error bars show the inaccuracy of the accelerometer. Ideally the acceleration is parallel to the lamp axis and the accelerations perpendicular to the lamp axis should be zero.

4.2.2 Gondola

A gondola is attached to the end of the arm of the centrifuge. The gondola contains the setup that consists of the lamp, the electronics and the measurement techniques. A mini-computer in the gondola is used to control the lamp power and to perform the acquisition. The data from the measurements are stored locally. To improve the performance of the measurement technique, the data are transferred via the network only after the measurements have been finished.

On top of the gondola two interchangeable setups can be placed, one for emission spectroscopy and one for ILAS. Both setups contain the lamp and a webcam to monitor the lamp. Webcam images show the effect of hyper-gravity on the lamp in the centrifuge. Some webcam images of the lamp containing 5 mg of mercury are shown in figure 4.7. This figure shows that the axial segregation is strongly reduced at 10g.

4.3 Diagnostics

The two measurement techniques used to investigate the lamp, emission spectroscopy and ILAS, will be discussed in turn.

4.3.1 Emission spectroscopy

The lamp is investigated using absolute line intensity spectroscopy, yielding the laterally resolved spectrum. After the calibration of intensity and wavelength, absolute radial density distributions of several particles in excited states are obtained. Furthermore,

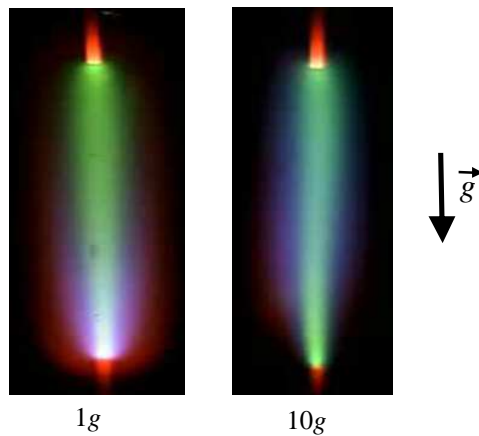


Figure 4.7: Webcam pictures of the lamp containing 4.2 mg DyI_3 and 5 mg Hg in the centrifuge [38], at $1g$ and $10g$. The input power is 130 W. Colour separation is seen at $1g$; at $10g$ the convection is dominant over diffusion and the colour separation disappears: the bluish-white light caused by the Dy atoms is more evenly distributed over the lamp.

several plasma properties can be determined, such as the temperature distribution, the ground state densities and the electron density.

Densities and plasma properties of the lamp have been measured by emission spectroscopy in experiments done previously [34, 41]. The setup used in these experiments is adjusted so it fits on top of the gondola for use in the centrifuge. In figure 4.8 a schematic overview of the emission spectroscopy setup is shown. An example of a lateral (line-of-sight) atomic dysprosium profile is shown in figure 4.9; the data are taken near the top of the lamp. Other results obtained by emission spectroscopy in the centrifuge are discussed by Nimalasuriya *et al* [38].

4.3.2 Imaging Laser Absorption Spectroscopy

The second measurement technique used in the centrifuge, ILAS, is a novel technique, with which the 2D density distribution of the radiating particles can be obtained. The theory of laser absorption spectroscopy has been described in chapters 2 and 3 [32, 33]. For clarity, the principles are summarized here.

General

In our experiment ILAS is used to obtain a 2D atomic density distribution of the metal additive in the lamp burner. A laser beam is expanded so that it illuminates the full lamp burner. When the lamp is switched on, part of the laser light is absorbed by the

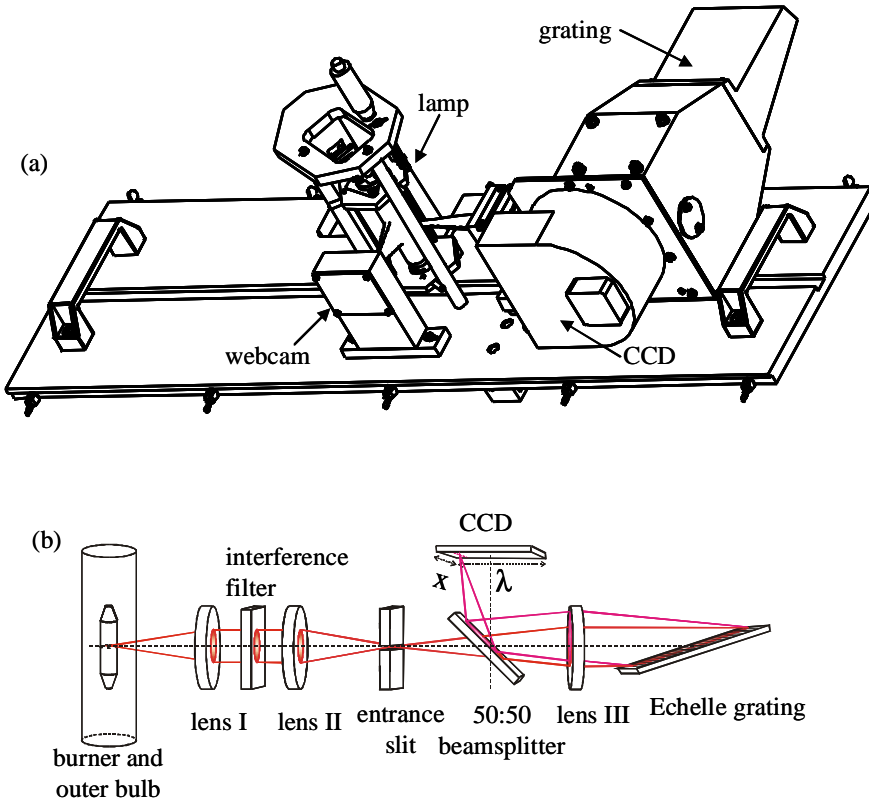


Figure 4.8: (a) Schematic drawing of the emission spectroscopy setup for the centrifuge. (b) Artist impression of the Echelle type spectrometer used in the ISS [38, 41]. In the centrifuge the beam splitter, CCD and the grating + lens III are rotated by 90° as is shown in (a).

metal additive particles. Behind the lamp, a CCD camera detects the light that passes through the lamp burner. The tunable diode laser (Sacher TEC 500 645-5) scans step by step over a wavelength range around an absorption line of the particle. At each wavelength step an image is taken by the CCD camera. The local line-of-sight atomic density n_{los} for each pixel on the CCD camera, which corresponds to a unique position in the lamp burner, is given by [32, 43–45, 47]:

$$n_{\text{los}} = -\frac{c}{S\lambda^2} \int \ln(T_\lambda) d\lambda, \quad (4.4)$$

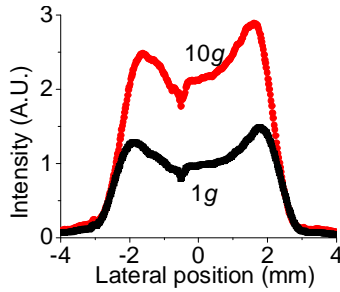


Figure 4.9: Atomic lateral profile of the atomic Dy line at 642.19 nm, measured by means of emission spectroscopy [38]. The lamp contains 4.2 mg DyI_3 and 5 mg Hg. The lamp input power is 150 W. The measurement is taken near the top of the burner ($y = 13$ mm; electrode distance in the burner is 18 mm). The intensity near the top of the lamp is higher at 10g than at 1g. The jump that is observed around -1 mm at 10g is due to a small imperfection of the slit in the spectrometer.

where c is the speed of light, S is the line strength of the transition, T_λ is the transmission (laser intensity at the CCD with absorption divided by the intensity without absorption) at wavelength λ . The integral is taken over the line width of the absorption line.

Measurement procedure

ILAS is used in our experiment to obtain the line-of-sight ground state atomic dysprosium density distribution in the lamp burner. In this section we discuss the necessary steps to obtain this density. During all these steps the lamp is turned on. The measurement by the CCD camera (SBIG ST-2000XM with 1600×1200 pixels of $7.4 \mu\text{m} \times 7.4 \mu\text{m}$ [60]) consists of a dark current measurement (shutter closed), a lamp emission measurement I_e , a reference measurement I_0 and the actual measurement I_λ : the scanning by the laser around the absorption wavelength.

The first two measurements are the dark current and lamp emission images. The next measurement is the reference measurement. The wavelength of the laser is chosen just outside the absorption dip, where no absorption takes place. Next, the actual absorption measurement starts. A tunable laser scans over a wavelength range of ~ 0.1 nm around the absorption wavelength of $\lambda = 642.19$ nm in N steps (in our experiments $N = 65$).

Data processing is as follows. First, dark current and lamp emission correction are applied to the reference and absorption images. Second, for each wavelength step n a relative transmission image is constructed by dividing the corrected absorption image

by the corrected reference image. The transmission is given by

$$T_\lambda = \frac{(I_\lambda - I_{d,\lambda}) - (I_e - I_{d,e})}{(I_0 - I_{d,0}) - (I_e - I_{d,e})} \times \frac{I_{ph,0}}{I_{ph,\lambda}}, \quad (4.5)$$

where $I_{d,e}$, $I_{d,0}$ and $I_{d,\lambda}$ are the darkcurrents in the emission, reference and measurements, respectively, and $I_{ph,0}$ and $I_{ph,\lambda}$ are the integrated laser intensities (measured by a photodiode) before entering the plasma for the reference and absorption measurements, respectively. This intensity correction is explained in section 4.3.2.

We thus obtain a 3D matrix filled with relative transmission values T ; so we get $T(\lambda(n), x, y)$: n is the wavelength step, x and y are the positions on the CCD camera. From this matrix, for each (x, y) equation (4.4) is used to calculate the line-of-sight atomic density n_{los} :

$$n_{los}(x, y) = -\frac{c}{S\lambda^2} \int \ln T(\lambda(n), x, y) d\lambda. \quad (4.6)$$

The integral is evaluated by fitting the area under the $\ln T$ curve.¹ Finally, a 2D ground state atomic Dy density distribution image is constructed from all these line-of-sight densities.

Figure 4.10 shows how the absorption curves for each pixel (x, y) of the CCD camera are constructed and an example of the relative transmission curve for an arbitrary pixel of the CCD; the reference measurement and the absorption measurements are indicated in the figure.

Setup

The ILAS setup in the centrifuge is shown in figure 4.11. Some problems were encountered during development of the ILAS technique. In contrast to the earlier laser absorption setup in chapters 2 and 3 [32, 33], the whole lamp burner is illuminated by the laser using beam expansion. Each point in the illuminated area of the lamp burner is used separately to obtain the line-of-sight density at that particular position in the lamp burner. This requires that the intensity distribution over the beam stays equal at different wavelengths.

The problems and their solutions that led to the final setup are discussed step by step.

1. *Reference measurement I_0* : The easiest way is to turn the lamp off and then make a wavelength scan (the same scan as the absorption images as described before). But when the lamp is switched on, it heats up and deforms. In this method, the

¹Ideally, one should apply Abel inversion before integrating over the wavelength, because the line shape may vary over the radius of the lamp. However, this is not practical because of noise in the measurement data. By integrating over the line-of-sight the area under curve—and thus the density—might be underestimated by 10–20% (section 2.3).

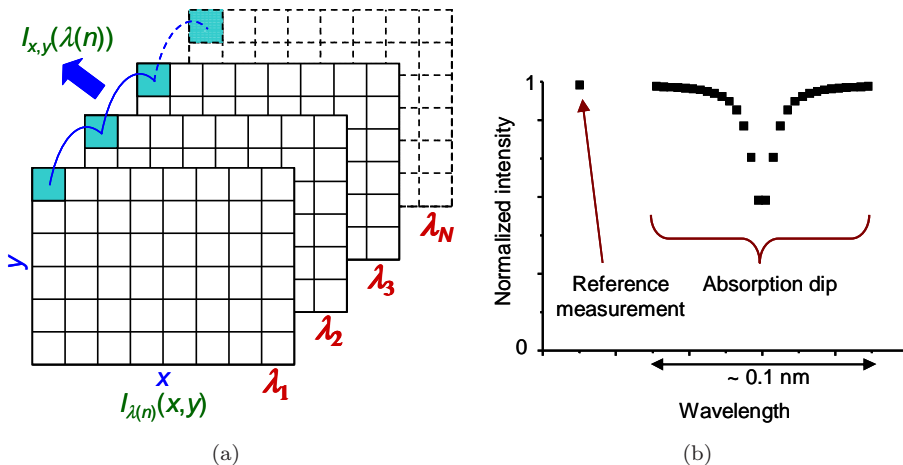


Figure 4.10: Artist impression of the ILAS measurement technique:

(a) For each wavelength λ_n an absorption image $I_{\lambda(n)}(x, y)$ is taken. Next for each pixel (x, y) the absorption dip $I_{x,y}(\lambda(n))$ is constructed.

(b) Impression of the measurement for an arbitrary pixel (x, y) of the CCD camera (not a real measurement). The intensity at the CCD is normalized by dividing the image by the intensity measured by the photodiode. First a reference measurement is taken at a wavelength where no absorption takes place. Next, the actual absorption measurement is performed.

reference measurement is not made under the same conditions as the absorption measurements. By leaving the lamp on and measuring the reference image at a wavelength outside the absorption dip, the same optical conditions as at the absorption measurement images are assured.

2. *Lamp emission I_e* : The light emitted by the lamp is much brighter than the laser light at the CCD (#17; the numbers given in this section refer to the parts in figure 4.11) and therefore it complicates the measurement. To reduce the lamp light on the CCD, an image quality colour filter (#12, LOT-Oriel D640/10m / LOT57900) is used. The transmission for the laser light is $\sim 80\%$, whereas the transmission of the lamp light intensity is reduced to $\sim 1\%$. The second tool to reduce the lamp light is a diaphragm (#14, diameter 2 mm) in the focal point between the lenses #13 and #15. Because the lamp light is out of focus as compared with the laser light, the diaphragm reduces the lamp light with another factor ~ 100 . By using both the filter and the diaphragm, the lamp emission intensity is smaller than the laser intensity. The remaining lamp light falling on the CCD is corrected for by subtracting this lamp emission from the

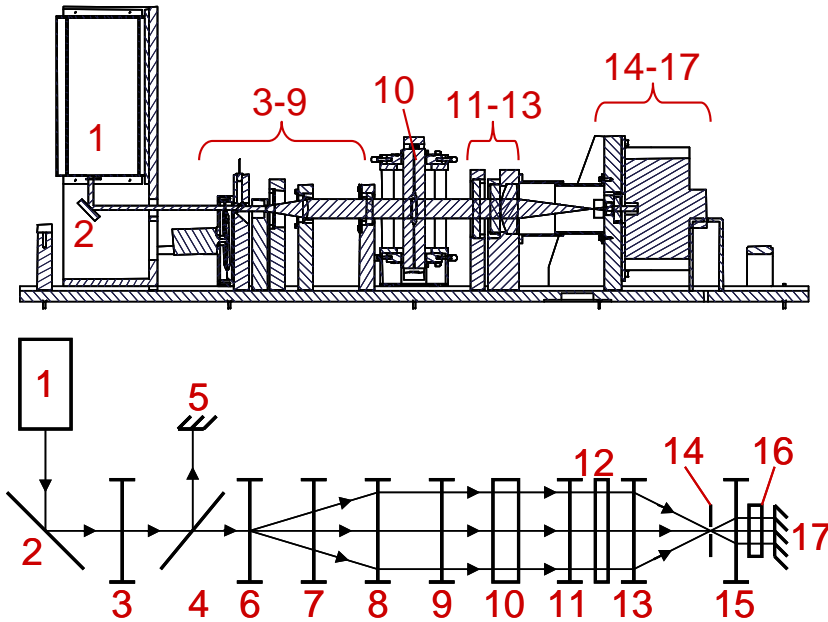


Figure 4.11: Schematic drawing of the ILAS setup: (1) tunable diode laser; (2) mirror (shutter between laser and mirror is not drawn); (3) rotating diffuser; (4) beam splitter; (5) photodiode; (6) spherical lens, $f = -6$ mm; (7) cylindrical lens, $f = -50$ mm; (8) diaphragm and cylindrical lens, $f = 50$ mm; (9) adjustable diaphragm and cylindrical lens, $f = -50$ mm; (10) lamp; (11) cylindrical lens, $f = 100$ mm; (12) colour filter; (13) spherical lens, $f = 80$ mm; (14) adjustable pinhole; (15) spherical lens, $f = 25$ mm; (16) neutral density filter; (17) CCD camera.

measurement images.

3. *Varying laser intensity:* The relative transmission is needed for equation (4.6). For this calculation, the laser intensity before entering the lamp should be independent of the wavelength. The laser intensity, however, is dependent on the wavelength. One has to correct for this effect before comparing measurement images. For this purpose, the intensity values of the images are normalized by dividing those values by the integrated laser intensity ($I_{\text{ph},0}$ and $I_{\text{ph},\lambda}$), which is measured simultaneously by a photodiode (#5). The normalized images are used in the calculations in equation (4.5). For this correction, it is assumed that the laser beam shape is independent of the wavelength and thus the laser light intensity at each position in the beam scales linearly with the total integrated laser intensity measured by the photodiode.

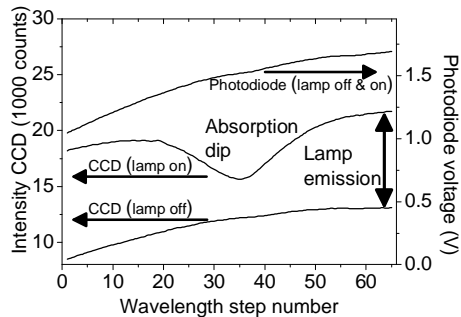


Figure 4.12: Averaged intensity on the CCD chip and photodiode voltage (\sim laser intensity) plotted as a function of the wavelength step. The measurements are performed with the lamp off and lamp on. The absorption dip and the lamp emission are indicated.

4. *Laser beam shape dependence of wavelength:* At each CCD pixel a line-of-sight absorption curve is obtained from a small part of the expanded laser beam, this makes the quality of the beam important. But when the laser beam is expanded, a diffraction pattern is observed, which moves when changing the wavelength. This pattern is probably caused by the grating in the laser head. This effect interferes with the spatially resolved absorption measurements, because the assumption that the laser beam shape is independent of the wavelength is no longer valid. To remove this diffraction pattern the laser beam passes a diffuser (#3, POC Light Shaping Diffuser, FWHM angle 0.5°) before entering the lamp. But another problem appears: after passing the diffuser, a speckle pattern shows up. To remove the speckle pattern, the diffuser rotates at 7130 rpm so that the pattern is mixed well and no speckles show up any longer. The value for the shutter time of the CCD camera should be set to at least several times (~ 10) the rotation time of the diffuser, so that the speckle pattern of the diffuser is averaged out. By using this rotating diffuser, no diffraction pattern is present in the laser beam and the requirement for the beam shape as stated in item 3 is met.
5. *Correlation between the CCD pixel and position in the burner:* The relation between the pixel position on the CCD and the spatial position inside the lamp burner is determined by the optics in the setup. The ray tracing program Zemax [61] is used to calculate the corresponding position in the lamp burner for each CCD pixel. When the corresponding height and lateral coordinates at each CCD pixel are known, a 2D mapping of the ground state atomic Dy density inside the lamp burner is obtained.

Implementing all the described solutions, the ILAS technique gives a 2D lateral particle density distribution inside the plasma volume.

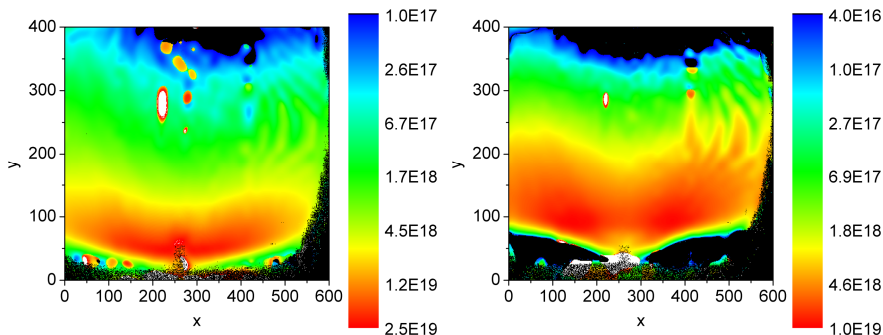


Figure 4.13: Line-of-sight 2D ground state atomic Dy density distribution at (left) 1*g* and (right) 10*g*. The coordinates are pixel numbers of the CCD; these are not yet converted to real coordinates inside the burner: $y = 0$ is the bottom and $y = 400$ is the top of the lamp; $x = -140$ and $x = 660$ are approximately the positions of the wall. The Dy density values are given in m^{-2} on a logarithmic scale. Note that the scales of both graphs are different; the density is lower for 10*g*.

4.4 Results

To prove the ILAS technique in the centrifuge, a measurement on a lamp is presented. Our lamp contains 5 mg Hg, 4 mg DyI₃ and 300 mbar Ar/Kr⁸⁵ as a starting gas. The input power is 148 W; the acceleration is 1*g* and 10*g*.

Figure 4.12 shows the laser intensity spatially averaged over the lamp (raw data); when the lamp is on and when the lamp is off. In this graph, the absorption dip is clearly seen. Furthermore, the figure shows the photodiode voltage (integrated laser intensity before entering the lamp) that is measured during the wavelength scan. This photodiode voltage is used to normalize the intensity measured by the CCD camera.

After the data (lamp-on condition) have been processed, the 2D ground state atomic Dy density is obtained; this density distribution is shown in figure 4.13. The relation between the lateral pixel number and the real lateral position x is not (completely) linear. Due to the optical system, it is not possible to measure close to the wall. However, we do not expect atomic Dy near the wall because of the lower temperature (section 4.1). The density averaged over the width of the lamp is plotted as a function of the axial position in figure 4.14. It is clearly seen that for 10*g*, axial segregation is diminished [32, 38]. These graphs show the functioning of the ILAS technique. In the future, Abel inversion will be applied to the line-of-sight 2D density distribution to obtain a 3D cylindrical symmetric ground state atomic Dy density distribution [29, 48, 62–65].

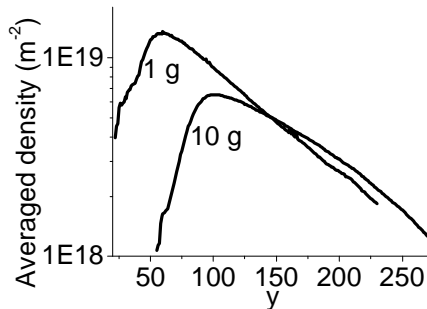


Figure 4.14: Dy density averaged over the width of the lamp (from figure 4.13), for different axial positions y ($y = 0$ is the bottom and $y = 400$ is the top of the lamp). For $10g$ the axial segregation is lower than for $1g$: the density decreases slower towards the top of the lamp for $10g$ than for $1g$. The amount of segregation is g dependent as stated in section 4.1 and figure 4.2. The lower density at the bottom of the lamp is due to electrode effects.

4.5 Conclusions

A new setup has been presented to investigate the metal-halide lamp at hyper-gravity conditions: a centrifuge that allows for the lamp to be accelerated up to $10g$. Higher gravity enhances convection and diminishes axial segregation. The acceleration at the position of the lamp was calibrated, and it was shown that the total acceleration vector was parallel to the lamp axis.

We performed both emission spectroscopy and ILAS on a MH lamp in the centrifuge. With the novel laser absorption measurement technique, a 2D particle density distribution is obtained by taking images of the laser intensity at each wavelength scan step.

First results of the Dy density in a metal-halide lamp were presented to test the ILAS technique under hyper-gravity conditions. This test clearly shows that the setup and measurement techniques are a useful tool to get more insight into the lamp; in this case by measuring the ground state atomic Dy density.

In the future the 2D particle density distribution will be converted to a 3D cylindrical symmetric profile by means of Abel inversion.

Acknowledgements

The authors are grateful to all participants in the ARGES project for their contributions, especially the General Technical Department of the Eindhoven University of Technology for building the centrifuge and M. Haverlag for the discussion about the theory of the lamps, and Senter-Novem (project EDI 03146), SRON [66] and the Dutch Ministries of Research and Education as well as Economic Affairs for funding the research.

Semi-empirical model for axial segregation in metal-halide lamps

Abstract.

Diffusive and convective processes in the metal-halide lamp cause an unwanted non-uniform distribution of the radiating metal additive (Dy in our case), which results in colour separation. The axial segregation has been described by E. Fischer [J. Appl. Phys. **47**, 2954 (1976)] for infinitely long lamps with a constant axis temperature. However, for our lamps this is not valid. We propose a semi-empirical extended model. The density inhomogeneity gives a measure for the non-uniformity of the Dy density distribution in the lamp. As an example, this parameter is calculated for some measurements obtained by imaging laser absorption spectroscopy.

This chapter has been adapted from [A.J. Flikweert, M.L. Beks, T. Nimalasuriya, G.M.W. Kroesen, M. Haverlag, J.J.A.M. van der Mullen and W.W. Stoffels, *Semi-empirical model for axial segregation in metal-halide lamps*, J. Phys. D: Appl. Phys. **41** (2008) issue 18].



Figure 5.1: (printed in colour in figure 1.3) The burner of a MH lamp (10 mg Hg, 4 mg DyI_3 , input power 150 W). Colour segregation is clearly visible [37, 67].

5.1 Introduction

High intensity discharge (HID) lamps have a high efficiency (up to 40%) and a good colour rendering index [3, 21–26, 35, 42]. They are for instance used for shop lighting, city beautification and street lighting. A commonly used HID lamp is the metal-halide (MH) lamp. These arc discharge lamps contain a buffer gas (usually mercury) and additives that act as prime radiator in the visible spectrum. In our case we use dysprosium iodide (DyI_3) as salt additive. This additive increases the efficiency and colour rendering of the lamp.

Colour segregation is observed when the lamp is burning in the vertical position. The colour segregation originates from the segregation of the additives. This limits the lamp design for application. Figure 5.1 shows the lamp when burning in the vertical position. The Dy atoms stay mainly at the bottom, where we see bluish-white light. The bluish colour at the top is caused by Hg atoms.

The convection of the buffer gas Hg in HID lamps was described by Kenty [68] and Elenbaas [53]. The segregation of additives in MH lamps was described by Zollweg [23]. His theory is based on single cell convection of the buffer gas and radial diffusion of the additives. E. Fischer [28] developed a model based on the diffusion–convection mechanism in vertically operated lamps. The diffusion is based on the chemical equilibrium between the salt molecules and the atoms. His model describes the amount of segregation as a function of the amount of convection (figure 5.2). The amount of Dy decreases exponentially with the axial position in the lamp. The amount of convection increases among others with Hg pressure, input power, aspect ratio of the burner and gravity [23, 28, 37, 69]. To vary the amount of convection, in the past several experi-

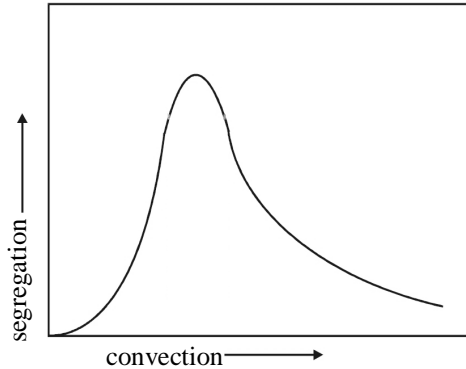


Figure 5.2: The Fischer curve shows the axial segregation as a function of the amount of convection [28, 32, 67]. The lamps we use are around the maximum of the curve.

ments under varying gravity conditions have been carried out: in the lab ($1g$, where g is the gravity at earth: 9.81 m s^{-2} ; see chapter 2 [32, 34, 35, 50]), the International Space Station ($0g$) [41], during parabolic flights ($0\text{--}2g$; chapter 3 [33]) and in a centrifuge ($1\text{--}10g$; chapters 4 and 8 [37–39]).

E. Fischer assumes an infinitely long lamp with a constant axis temperature and no end effects of the convection flow. However, our lamps have a burner length of 10–30 mm and a diameter between 4 and 8 mm [27]. For these lamps, the axis temperature is not constant. Therefore, the Fischer theory cannot be applied to our lamps.

The aim of this chapter is to propose a semi-empirical axial segregation model and to introduce a new parameter that expresses the degree of inhomogeneity in the axial direction of any plasma parameter. First, the transport phenomena in the MH lamp are summarized. The axial segregation model as described by E. Fischer is discussed briefly. This model is only valid for a constant axis temperature. Whereas Fischer predicts an exponentially decreasing Dy density as a function of the axial position, we observe that the Dy density from the bottom to the top first increases, and next decreases. The increase is explained by the non-uniform temperature over the axis, which shifts the chemical equilibrium between atoms and molecules. The temperature distribution was obtained by numerical simulations [42, 70].

We introduce a new parameter: the density inhomogeneity. This parameter can be used to determine the inhomogeneity of the additives, which is independent of the measurement technique and lamp geometry. To compare with earlier results [32, 38, 50], the segregation model of Fischer can be corrected for the temperature effect. This corrected axial segregation parameter is only valid if the temperature effect is not dominant. We give some examples of the density inhomogeneity and the corrected axial segregation parameter for our lamps.

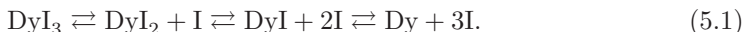
5.2 Transport in the MH lamp

The theory of the transport phenomena in the MH lamp has been described in earlier publications [28, 32, 33, 67]. For clarity, the most important part is summarized here.

After ignition of the lamp, Hg evaporates first. Next, during heat up, the salt (DyI_3) evaporates and enters the arc. Because of the temperature gradient (~ 5500 K at the centre and ~ 1200 K at the wall) in combination with gravity, we have convection. The gas in the hot centre moves upwards, whereas the gas at the cooler wall moves downwards.

Due to the large temperature gradient in the radial direction, a multi-step process of dissociation of the DyI_3 molecules takes place when moving from the wall to the centre [32, 50, 70]. In addition, in the hot centre ionization of the Dy atoms takes place [31]. The lighter atoms and ions diffuse faster outwards than the heavier molecules move inwards. This difference in diffusion velocities leads to a hollow radial profile of the elemental Dy pressure; this is called radial segregation. In addition, the density in the centre is lower due to the ideal gas law $p = nkT$.

The chemical equilibrium between DyI_3 molecules and atoms is given by



The equilibrium shifts to the right when the temperature is increased. When the temperature is increased even further, ionization of Dy atoms takes place:



The partial pressures of the different particles were calculated as a function of temperature, under assumption of local thermodynamical equilibrium (LTE) and for a fixed cold spot temperature of 1100 K [56]. These pressures are shown in figure 5.3.

While the atoms are moving outward caused by diffusion, they are dragged downward by the convection flow. As a result, the atoms stay at the bottom of the lamp. The combination of convection and diffusion causes an axial gradient in atomic Dy density: axial segregation appears. When the diffusion and convection are in the same order of magnitude, maximal axial segregation occurs. In the two limiting cases, when the convection is very small, or when the convection is much stronger than the diffusion, no axial segregation is present.

5.3 Axial segregation

An axial segregation model based on diffusion and convection has been proposed by E. Fischer [28]. This model, which is valid for an infinitely long lamp burning in the vertical position, is repeated briefly in section 5.3.1. The Fischer model assumes a constant axis temperature. However, our lamps are not infinitely long and have an

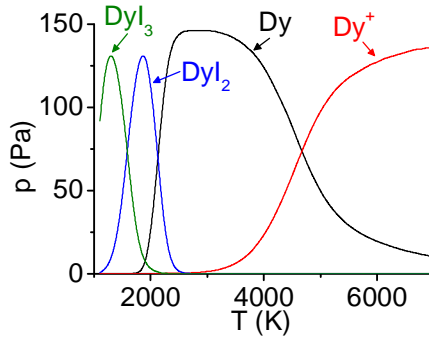


Figure 5.3: Theoretical pressures of Dy atoms, ions and molecules as a function of temperature, at a fixed cold spot temperature of 1100 K. The DyI pressure is small and has been omitted for clarity [56, 71].

axial temperature gradient. Section 5.3.2 shows that the atomic Dy density determined by Saha [31] and Guldberg–Waage (chemical equilibrium) is not constant over the axial position in the lamp, due to the temperature variation over the axis. The temperature profile was obtained by numerical simulations [42, 70].

Section 5.3.3 introduces a new parameter which describes the density inhomogeneity of additives in the lamp. This parameter is normalized and can be used for different lamp geometries and for different particles in the lamp. When the temperature effect is combined with the Fischer theory, we can define a corrected segregation parameter. This is described in section 5.3.4. When the temperature effect is more important than the segregation according to Fischer, the corrected segregation parameter is not valid anymore and only the inhomogeneity parameter can be used to characterize the lamp.

5.3.1 Fischer model

E. Fischer [28] developed a diffusion–convection axial segregation model for an infinitely long lamp, burning in the vertical position. He assumes a parabolic radial temperature profile that is independent of the axial position. The convection profile in the lamp, which is the convection profile of the buffer gas in all MH lamps [38], is calculated using the Navier–Stokes equation. The axial convection speed v_z is described by [42, 53, 70]

$$v_z \sim p_{\text{Hg}} R^2 g, \quad (5.3)$$

where p is the pressure, R the burner radius and g gravity. The convection speed v_z also increases with increasing lamp input power P since the temperature gradient increases [23].

Fischer solved the transport problem. For the Dy density $n_{\text{Dy}}(r, z)$ (m^{-3}) in the

lamp this gives

$$n_{\text{Dy}}(r, z) = n_{\text{Dy},0}(r) \exp(-\lambda z), \quad (5.4)$$

where r is the radial position in the lamp, $n_{\text{Dy},0}(r)$ is the Dy density at the bottom of the lamp at the radial position r and λ is the axial segregation parameter.

We want to average out noise in the measurement data, and therefore the Dy density is radially averaged. The radially integrated Dy density $N_{\text{Dy}}(z)$ is given by

$$N_{\text{Dy}}(z) \equiv \int_0^R n_{\text{Dy}}(r, z) \cdot 2\pi r dr, \quad (5.5)$$

where R is the radius of the burner. The density $N_{\text{Dy}}(z)$ is the amount of Dy present in the cross section of the lamp at the axial position z , per unit length (m^{-1}).

When we radially integrate equation (5.4) we obtain

$$\begin{aligned} N_{\text{Dy}}(z) &= \exp(-\lambda z) \cdot \int_0^R n_{\text{Dy},0}(r) \cdot 2\pi r dr \\ &\equiv N_{\text{Dy},0} \exp(-\lambda z). \end{aligned} \quad (5.6)$$

The Fischer curve, which gives the amount of axial segregation λ as a function of the amount of convection, is shown in figure 5.2. The segregation is maximal when the convection is in the same order of magnitude as the diffusion. In the two limiting cases, when the convection is much smaller than diffusion, or when the convection is dominant over diffusion, we have [28, 33, 37]

$$\begin{aligned} \lambda &\sim p_{\text{Hg}}^2 R^2 g && \text{for small } p_{\text{Hg}}, R \text{ or } g, \text{ and} \\ \lambda &\sim (p_{\text{Hg}}^2 R^2 g)^{-1} && \text{for large } p_{\text{Hg}}, R \text{ or } g. \end{aligned} \quad (5.7)$$

5.3.2 Temperature influence on atomic Dy density

The Fischer model of axial segregation of the elemental Dy is valid for the infinitely long vertically burning lamp only. He assumes a constant axial temperature and no electrode effects. However, in real life the lamps are finite size. Therefore, we need to take into account an axial temperature gradient. Furthermore we want to have a model that describes the axial segregation of atomic Dy, whereas the Fischer model describes elemental densities. To bridge the gap between the Fischer model and the COST reference lamps (see section 1.3.1 and [27]) used in our experiments [32, 33, 35, 37, 39, 42, 67], we develop a new semi-empirical model.

Our lamps have an axial temperature gradient. When the temperature changes, the chemical equilibrium between DyI_3 molecules and Dy and I atoms shifts. The densities of the different particles in equation (5.1) were calculated as a function of temperature, under assumption of Local Thermodynamical Equilibrium (LTE) and for a fixed cold spot temperature of 1100 K [56]. The cold spot of the lamp is located at the

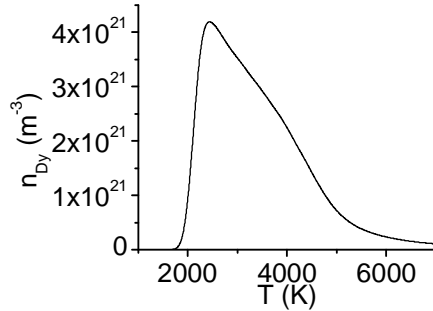


Figure 5.4: Atomic Dy density (all states) as a function of temperature T , at a fixed cold spot temperature of 1100 K. The decrease at a higher temperature is caused by the ionization of the Dy atoms.

bottom, where the salt pool is located. At low temperature we mainly have molecules, whereas at high temperature mainly ions are present. Somewhere in between we have the temperature where the atomic Dy density (and thus the radiative output) is the highest. Figure 5.4 shows the atomic Dy density as a function of temperature.

For a lamp of 20 mm height and 8 mm diameter Beks *et al* [70] carried out numerical simulations to calculate the temperature profile $T(r, z)$ in the lamp burner under various gravity conditions. The temperature profile for a lamp with 5 mg Hg, 150 W lamp input power, at $1g$ is shown in figure 5.5(a). From this temperature profile the radial atomic Dy profile $n_{\text{Dy}}(r, z)$ is calculated (figure 5.5(b)). This profile shows the density profile determined by the Saha and Guldberg–Waage equilibria; the calculated density at each position is only based on temperature, neglecting diffusion and convection effects. Taking the radially integrated atomic Dy density gives the curves shown in figure 5.6, for $1g$ and $10g$. At $10g$ the temperature varies more along the axis.

Due to the temperature influence, the Fischer parameter as discussed in section 5.3.1 is not valid anymore for our lamps. Therefore, a new parameter should be introduced to describe the axial segregation in the lamps.

5.3.3 Axial density inhomogeneity parameter

Fischer described the axial segregation by an exponential decay of the density in the axial direction. We introduce a new parameter to express the degree of inhomogeneity in the axial direction for any plasma parameter, which does not assume a particular shape for the axial profile.

In general, any lamp property can be described by $q(r, z)$. For the axial inhomogeneity of the lamp property $q(r, z)$ we first integrate over the cross section of the lamp

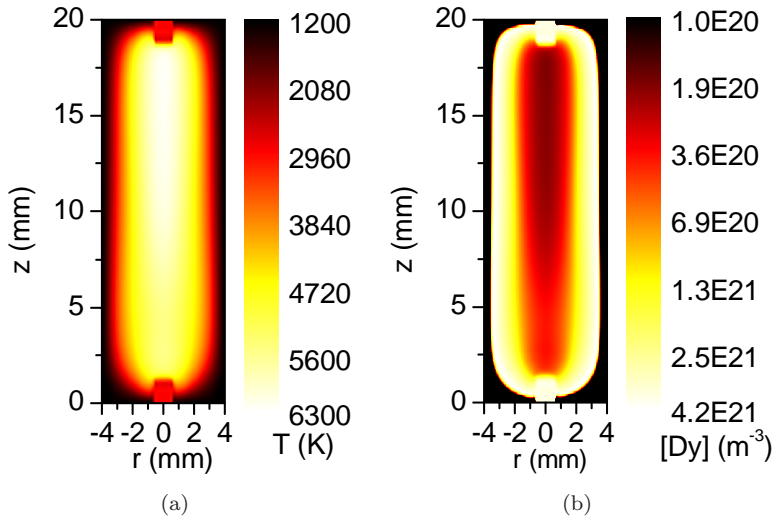


Figure 5.5: (a) Temperature profile $T(r, z)$ obtained by numerical simulations [42] for a lamp containing 5 mg Hg and 4 mg DyI₃, input power 150 W at 1g. (b) Radial atomic Dy density $n_{\text{Dy}}(r, z)$ for a fixed cold spot temperature of 1100 K. This profile is based on LTE calculations and the calculated temperature profile of (a) and neglecting diffusion and convection effects.

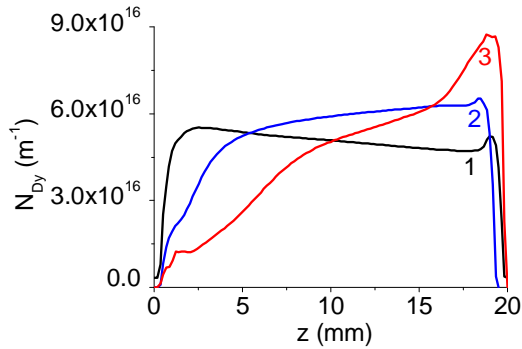


Figure 5.6: Radially integrated atomic Dy densities $N_{\text{Dy}}(z)$, calculated from figure 5.5 by equation (5.5) for different amounts of mercury and gravity: (1) 5 mg Hg, 1g; (2) 5 mg Hg, 10g; (3) 10 mg Hg, 10g. For these densities only the temperature profiles $T(r, z)$ are taken into account; segregation effects due to diffusion and convection have not been taken into account.

at axial position z :

$$Q(z) = \int_0^R q(r, z) \cdot 2\pi r dr. \quad (5.8)$$

Next we normalize this property $Q(z)$ over the height:

$$\bar{Q} = \frac{1}{H} \int_0^H Q(z) dz = \frac{1}{H} \int_0^H \left(\int_0^R q(r, z) \cdot 2\pi r dr \right) dz, \quad (5.9)$$

where H is the height of the lamp burner. Next the difference between the lamp property $Q(z)$ at position z and the average \bar{Q} is calculated and normalized. This gives the axial inhomogeneity parameter α :

$$\alpha = \sqrt{\frac{1}{H} \int_0^H \left(\frac{Q(z) - \bar{Q}}{\bar{Q}} \right)^2 dz}. \quad (5.10)$$

A value of $\alpha = 0$ means that lamp property $Q(z)$ is homogeneous over the lamp height H .

The axial inhomogeneity parameter α is generally applicable and dimensionless, in contrast to the Fischer parameter λ . Therefore, α is independent of the measurement technique and lamp geometry. This parameter can, among others, be used for imaging laser absorption spectroscopy (ILAS) measurements [72], where we can use α to describe the atomic Dy distribution over the lamp. Furthermore, it can be used for optical emission spectroscopy measurements with an axial intensity profile, where α is the intensity inhomogeneity. The parameter is normalized for the length of the burner and can be used to compare different lamp geometries of the same type (for example, we can compare different MH lamps or we can compare different ultra high pressure (UHP) lamps).

The inhomogeneity parameter α can, for example, be used to describe the density inhomogeneity of the ground state atomic Dy densities that are measured by ILAS: in equations (5.9) and (5.10), $Q(z)$ is substituted by $N_{\text{Dy}}(z)$. When the temperature influence (section 5.3.2) is negligible and the Fischer model is valid, a relation can be found between the generic density inhomogeneity α and the particular Fischer parameter λ . When $Q(z) = N_{\text{Dy}}(z)$ in equation (5.10) is substituted by the Fischer formula (equation (5.6)) we obtain:

$$\alpha(\lambda) = \sqrt{\frac{\lambda H}{2} \cdot \frac{1 + \exp(-\lambda H)}{1 - \exp(-\lambda H)} - 1}. \quad (5.11)$$

If $\lambda H \gtrsim 1$, we get $\alpha^2 \sim \lambda$ and the dependences as given in equation (5.7) are also valid for α^2 .

5.3.4 Corrected Fischer parameter

To compare with earlier measurements where Fischer parameters were obtained, we introduce a corrected Fischer parameter which takes the temperature influence into account. This corrected parameter should follow the dependence of p , g and P as given in equation (5.7).

The axial temperature profile in the lamp determines the chemical equilibrium and the shift between atoms and ions (section 5.3.2). Beks *et al* obtained the temperature profiles of the MH lamp by numerical simulations as shown in figure 5.5(a). The density $N_{\text{Dy}}(z)$ from the simulations without convection and diffusion, thus only determined by the local temperature, is given in figure 5.6. To correct the Fischer parameter, we want to introduce a correction term $T_{\text{cor}}(z)$ for equation (5.6), that follows the same trend as the N_{Dy} curves in figure 5.6. Hereto we propose the following semi-empirical equation:

$$T_{\text{cor}}(z) = \left(1 - \exp\left(-a(z-b)^2\right)\right) \cdot (1 + cz), \quad (5.12)$$

where a , b and c are fitting parameters. This correction function describes the rising part of the curve by the exponential term $(1 - \exp(-a(z-b)^2))$. This rise is caused by the increasing temperature from the bottom electrode upwards, which first increases the atomic Dy density as seen in figure 5.4. When the temperature increases further, the atomic Dy density decreases because of ionization. This is described by the second term $(1 + cz)$. The combination of these two terms that describe the rising and decreasing parts describes well the trends of the curves in figure 5.6.

When the temperature correction of equation (5.12) is taken into account, the segregation parameter λ introduced by E. Fischer (equation (5.4)) can be corrected for the temperature effect. This corrected Fischer parameter λ_c is used to compare measurements with the theory for lamps with constant axial temperature as described by Fischer.

The ground state atomic Dy density $N_{\text{Dy}}(z)$ is a product of the Fischer equation and the temperature correction $T_{\text{cor}}(z)$:

$$\begin{aligned} N_{\text{Dy}}(z) &= N_{\text{Dy},0} \cdot \exp(-\lambda_c z) \cdot T_{\text{cor}}(z) \\ &= N_{\text{Dy},0} \cdot \exp(-\lambda_c z) \cdot \left(1 - \exp\left(-a(z-b)^2\right)\right) \cdot (1 + cz). \end{aligned} \quad (5.13)$$

This equation defines the corrected segregation parameter λ_c . When the temperature correction $T_{\text{cor}}(z)$ is small, $\lambda_c \approx \lambda$. The corrected axial segregation parameter can be obtained by fitting of, for example, ILAS measurements [37]. In this case the ground state atomic Dy density $N_{\text{Dy}}(z)$ is experimentally determined and fitted by equation (5.13).

The quantitative model described in this section is valid for finite lamps, with an axial temperature gradient. The segregation parameter λ_c obtained from equation (5.13) is only applicable when the correction for the temperature (equation (5.12)) is

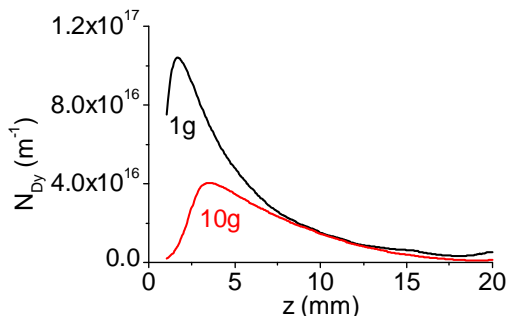


Figure 5.7: Radially integrated ground state atomic Dy for a lamp obtained by ILAS, at $1g$ and $10g$ (5 mg Hg, 4 mg DyI₃, $P = 148.4$ W) [37]. The fit according to equation (5.13) is indistinguishable from the experimental data and therefore not shown.

smaller than the segregation according to Fischer (equation (5.4)). If the temperature effect on the atomic Dy density is greater than the segregation by Fischer, the obtained λ_c is inaccurate and does not give a measure for the axial segregation in the lamp. We can check this by calculating $\alpha(\lambda_c)$ by equation (5.11) and compare this value with α obtained directly from the measurement (section 5.3.3). The larger the difference between these two values, the larger the temperature effect is.

5.4 Example of fitting parameters for a measurement

The parameters α and λ_c (sections 5.3.3 and 5.3.4) have been obtained for a COST reference lamp (section 1.3.1) [27]. The lamp contains a starting gas (300 mbar Ar/Kr⁸⁵), 5 mg Hg as buffer gas (6 bar)¹ and 4 mg DyI₃ as salt additive. The diameter of the lamp is 8 mm and the height is 20 mm. The input power is $P = 148.4$ W. The gravity is varied between $1g$ and $10g$.

In figure 5.7 the radially integrated atomic Dy density N_{Dy} of the lamp is plotted as a function of the axial position z in the lamp. The figure shows that the density maximum shifts upwards for higher g . This is in agreement with figure 5.6, which shows that the Dy density also shifts upwards caused by the shift in the temperature.

For the curves shown in figure 5.7, the values for the density inhomogeneity are $\alpha = 1.05$ ($\alpha^2 = 1.10$) and $\alpha = 0.92$ ($\alpha^2 = 0.85$) at $1g$ and $10g$ respectively. The temperature dependence causes the maximum of the ground state atomic Dy density to shift upwards. It also affects the slope of the decreasing part in figure 5.7. For these two curves, the uncorrected segregation parameters are $\lambda = 0.23$ mm⁻¹ and $\lambda = 0.16$ mm⁻¹ at $1g$ and $10g$ respectively, whereas the corrected segregation parameters

¹When the cold zones behind the electrodes are taken into account, the pressure is around 5 bar.

are $\lambda_c = 0.24 \text{ mm}^{-1}$ and $\lambda_c = 0.10 \text{ mm}^{-1}$ respectively. These values show a greater difference at $10g$ than at $1g$, because the temperature effect is also stronger at $10g$ than at $1g$. When the values of α^2 are compared with the segregation parameters λ_c , one sees that at $10g$ the segregation parameter is decreased compared to $1g$, whereas the density inhomogeneity is only decreased slightly. This difference is caused by the axial temperature gradient that is stronger at $10g$ than at $1g$ (figure 5.6), partially cancelling the lower Fischer segregation.

The influence of the temperature gradient is also seen when $\alpha(\lambda = \lambda_c)$ is calculated (equation (5.11)). We obtain 1.44 and 0.31 for $1g$ and $10g$ respectively. At $1g$ the measured density inhomogeneity (1.05) is somewhat smaller than one would expect from $\alpha(\lambda_c)$ (1.44), but at $10g$ the density inhomogeneity (0.92) is much larger than one would expect (0.31). This indicates that at $10g$ the temperature gradient along the axis has a strong influence on the density inhomogeneity.

5.5 Conclusions

We introduced the axial density inhomogeneity parameter α , which describes the axial inhomogeneity of the additive density for real lamps with an axial temperature gradient. This is an addition to the Fischer model, which describes the axial segregation of the metal additives in infinitely long lamps with a constant axial temperature profile. In our case the MH lamp, containing DyI_3 as salt additive, is not infinitely long and we have an axial temperature gradient. When the temperature changes, the chemical equilibrium between salt molecules, atoms and ions shifts. The radially integrated density of Dy atoms as a function of the axial position, determined by the Saha and Guldberg–Waage equilibria, has been obtained by temperature calculations from numerical modelling.

Two parameters have been introduced. Firstly, the density inhomogeneity α describes the inhomogeneity in the additive density. Secondly, the Fischer parameter has been corrected for the temperature influence. This gives the corrected axial segregation parameter λ_c and can only be obtained when the temperature influence is not dominant.

Finally, as an example, the parameters α and λ_c were calculated for two measurements obtained by ILAS. From these measurements, it is concluded that the temperature influence is much more pronounced for $10g$ than for $1g$. This is in agreement with the temperature calculations by the numerical simulations.

Acknowledgements

The authors are grateful to all participants in the ARGES project for their contributions, especially the General Technical Department of the Eindhoven University of Technology for building the centrifuge, and Senter-Novem (project EDI 03146), SRON [66] and the Dutch Ministries of Research and Education as well as Economic Affairs for funding the research.

6

Imaging laser absorption spectroscopy of the metal-halide lamp under hyper-gravity conditions ranging from 1 to 10g

Abstract.

The metal-halide (MH) lamp shows an unwanted non-uniform distribution of the metal additive (Dy in our case), caused by convection and diffusion phenomena. MH lamps with various Hg pressures and burner lengths have been investigated by imaging laser absorption spectroscopy under varying gravity conditions in a centrifuge (1–10g). 2D ground state Dy density profiles have been determined. From these images, the density inhomogeneity and corrected axial segregation parameters are obtained. The profiles and parameters are affected by the axial temperature gradient, which is more pronounced for higher Hg pressures and shorter burner lengths.

This chapter has been adapted from [A.J. Flikweert, A.F. Meunier, T. Nimalasuriya, G.M.W. Kroesen and W.W. Stoffels, *Imaging laser absorption spectroscopy of the metal-halide lamp under hyper-gravity conditions ranging from 1 to 10g*, J. Phys. D: Appl. Phys. **41** (2008) issue 18].

6.1 Introduction

The metal-halide (MH) lamp is a high intensity discharge lamp with a good colour rendering and a high luminous efficacy [3, 21–26, 35, 39, 42]. MH lamps are for instance used for street lighting, stadium lighting, city beautification and shop lighting.

The lamp contains a buffer gas (usually Hg) and metal additives dosed as metal-halide salts (in our case DyI_3). The additives improve the colour rendering of the lamp. When the lamp is burning in the vertical position, axial colour segregation appears. The non-uniform light output limits the applicability, because it has a negative influence on the efficiency and the colour rendering of the lamp.

The non-uniform distribution of additives is caused by the combination of convection and diffusion in the lamp. The axial segregation of the additives has been described by E. Fischer [28]. An extension of this model has been proposed for our lamps in chapter 5 [73].

Convection is induced by gravity. In the past several experiments under varying gravity conditions have been carried out. Beside lab experiments [32, 34, 35, 50], the lamp was sent to the International Space Station ($0g$, where g is the gravity at earth: 9.81 m s^{-2}) [41]. Furthermore parabolic flights were carried out ($0-2g$, for periods of about 20 s; chapter 3 [33]). More recently a centrifuge was built, which can achieve gravity conditions from 1 to $10g$ (chapter 4 [37–39]). The additive distribution in the lamp, in our case the two-dimensional column density of ground state dysprosium atoms in a COST lamp [27], is measured by means of imaging laser absorption spectroscopy (ILAS) in chapters 4 and 8 [37, 39].

The aim of this chapter is to understand the flow phenomena in the lamp by studying the additive density distributions. The competition between convection and diffusion is understood by applying the recently developed semi-empirical axial segregation model [73].

In this chapter, first the theory of the axial segregation in the lamp is described briefly. Next we propose some parameters to characterize the lamp. The ILAS setup is discussed briefly. We show some 2D ground state atomic Dy density profiles. As an example two column density profiles are inverted to radial profiles by means of Abel inversion. Further analysis is done on the lateral density profiles. The 2D density distribution in the lamp is characterized by various parameters. For different lamp configurations (different length, different amount of Hg filling) the values for the ground state atomic Dy density inhomogeneity and the corrected axial segregation parameters are calculated from the ILAS results. Finally some conclusions are drawn.

6.2 Theory

The flow phenomena of the MH lamp have been described in the previous chapters [28, 32, 33, 67, 73]. First the theory of axial segregation is repeated briefly. The Abel

inversion technique, which is used to invert column density profiles into radial density profiles, is discussed briefly. Next the parameters that are used to characterize the ground state atomic Dy density profiles in the lamps are introduced.

6.2.1 Axial segregation

The temperature gradient between the hot centre (~ 5500 K) and the cooler wall (~ 1200 K) causes convection. The hot gas in the centre moves upwards, whereas the cooler gas at the wall moves downwards. Secondly, we have diffusion. At the wall mainly DyI_3 molecules are present. From the wall to the centre the molecules dissociate into atoms and in the very centre the Dy atoms are ionized to Dy^+ . The diffusion of atoms and ions towards the wall is faster than the diffusion of the molecules towards the centre; this is called radial segregation. While the atoms are moving outwards and being associated into molecules, they are dragged downwards by convection. In this way Dy in any chemical form stays at the bottom of the lamp: the highest elemental Dy density is found at the bottom. This effect is maximal when the convection and diffusion are in the same order of magnitude: maximal axial segregation appears. In the limiting cases, when no convection is present or when the convection is very strong (e.g. hyper-gravity), good axial mixing occurs.

Besides the convection and diffusion, another process determines the atomic Dy density distribution. The temperature determines the chemical equilibrium between molecules, atoms and ions. In our lamps, we have an axial temperature gradient. The axial segregation is determined not only by convection and diffusion but also by the axial temperature profile [73]. This axial temperature gradient determines the 2D density profiles, the axial density inhomogeneity and the accuracy of the corrected Fischer parameter.

6.2.2 Abel inversion

The column density profile gives the line-integrated density at each lateral position (x, z) . Because the plasma is radially symmetric, one would like to invert the lateral profile $n_{\text{col,Dy}}(x, z)$ (m^{-2}) into a radial profile $n_{\text{Dy}}(r, z)$ (m^{-3}). The column density profile can be inverted to a radial density profile by means of Abel inversion [29, 32, 34, 41, 49, 64]. The column density at lateral position x and the axial position z is given by

$$n_{\text{col,Dy}}(x, z) = 2 \int_x^R \frac{n_{\text{Dy}}(r, z)}{\sqrt{r^2 - x^2}} r dr, \quad (6.1)$$

where $n_{\text{Dy}}(r, z)$ is the radial density and R is the radius of the burner. The radial density profile can be estimated by a polynomial series (e.g. $a_n r^n$ or Legendre polynomials). Other methods are filtered backprojection by using fast fourier transform and onion peeling [48, 63, 74, 75]. By onion peeling, first the density of a ring at the edge

of the plasma is determined. Next this is ring is subtracted, and the density in the next ring is determined, and so on until the density at the centre is determined. An accumulation of small errors at the edge is thereby translated into larger errors at the centre.

Zhu [29] performed numerical tests of the Abel inversion using polynomials. This Abel inversion method is sensitive to noise in the column density data, especially at the centre. A bit of noise gives a totally different radial profile; different radial profiles correspond to almost the same lateral profile.

These Abel inversion techniques are too complicated and are sensitive to noise. For this reason, we use a simple Abel inversion technique. We assume a simple radial profile $n_{\text{Dy}}(r, z)$. A drawing is given in figure 6.1. The profile consists of $N = 16$ concentric rings with a constant density a_i within ring i . The advantage of this profile is that all rings can be forced to be positive. The density is given by

$$n_{\text{Dy}}(r, z) = a_i \quad \text{where} \quad i = \text{floor} \left(\frac{r}{R} N + 1 \right). \quad (6.2)$$

In the lateral domain we obtain

$$n_{\text{col,Dy}}(x, z) = \sum_{i=1}^N a_i \cdot d(x, i), \quad (6.3)$$

where

$$d(x, i) = \begin{cases} 2 \left(-\sqrt{r_1^2(i) - x^2} + \sqrt{r_2^2(i) - x^2} \right) & \text{for } 0 \leq x < r_1(i) \\ 2\sqrt{r_2^2(i) - x^2} & \text{for } r_1(i) \leq x < r_2(i) \\ 0 & \text{for } x \geq r_2(i) \end{cases} \quad (6.4)$$

and

$$\begin{aligned} r_1(i) &= \frac{i-1}{N} R, \\ r_2(i) &= \frac{i}{N} R. \end{aligned}$$

Fitting the values a_i in the lateral domain (equation (6.3)) gives the radial profile $n_{\text{Dy}}(r, z)$ (equation (6.2)). The constraint is that all a_i have positive values.

6.2.3 Parameters

Various parameters describe the density distribution of Dy atoms in the lamp. The axial segregation can be described by the density inhomogeneity and the axial segregation parameter. These parameters have been described in chapter 5 [73] and are summarized here.

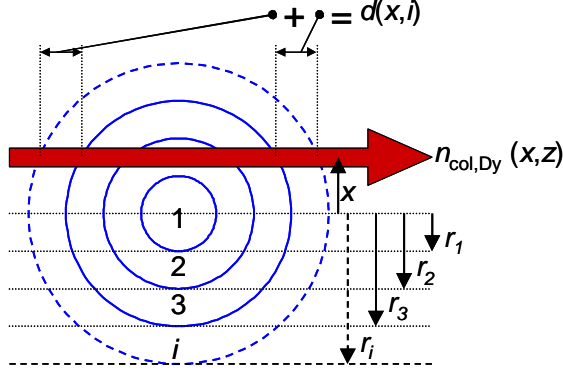


Figure 6.1: Schematic drawing of the cross-section of a cylindrical symmetric plasma at the axial position z . For Abel inversion, we assume concentric rings of constant density a_i . The radii of the rings are indicated by r_i . The column density $n_{\text{col,Dy}}(x, z)$ in this example consists of contributions from ring 2 to i . The distance $d(x, i)$ travelled through ring i is also indicated.

Density inhomogeneity

The inhomogeneity of a lamp property $Q(z)$ was introduced in equation (5.10). In this chapter the inhomogeneity of the ground state atomic Dy density integrated over the cross-section at the axial position z is derived; $Q(z) = N_{\text{Dy}}(z)$ (m^{-1}). The axial density inhomogeneity gives a measure for how non-uniform the distribution of ground state Dy atoms over the lamp height is, analogous to equation (5.10):

$$\alpha = \sqrt{\frac{1}{H} \int_0^H \left(\frac{N_{\text{Dy}}(z) - \bar{n}_{\text{Dy}}}{\bar{n}_{\text{Dy}}} \right)^2 dz}, \quad (6.5)$$

where H is the height of the lamp burner. A value of $\alpha = 0$ means that the Dy atoms are evenly distributed over the height of the lamp. The parameter is normalized for the lamp height and the average density \bar{n}_{Dy} .

The density per unit length of the lamp $N_{\text{Dy}}(z)$ can be obtained by integrating the radial density profile over the radius of the lamp. This is equal to integrating the column density profile over the width of the lamp:

$$N_{\text{Dy}}(z) = \int_0^R n_{\text{Dy}}(r, z) \cdot 2\pi r dr = \int_{-R}^R n_{\text{col,Dy}}(x, z) dx. \quad (6.6)$$

The density inhomogeneity is determined by the axial segregation (following section) and the axial temperature profile in the lamp.

Axial segregation parameter

To compare with earlier measurements where Fischer parameters were obtained, a corrected Fischer parameter has been introduced in equation (5.13) which takes the temperature influence into account. The Fischer formula of the Dy density N_{Dy} as a function of the axial position z is given by [28, 73]

$$N_{\text{Dy}}(z) = N_{\text{Dy},0} \cdot \exp(-\lambda z). \quad (6.7)$$

When we take the temperature influence into account, the radially integrated atomic Dy density is given by:

$$N_{\text{Dy}}(z) = N_{\text{Dy},0} \cdot \exp(-\lambda_c z) \cdot \left(1 - \exp\left(-a(z-b)^2\right)\right) \cdot (1 + cz). \quad (6.8)$$

In this equation, $N_{\text{Dy},0}$ is the atomic Dy density at the bottom of the lamp burner per unit length (m^{-1}), and the radially integrated atomic Dy density $N_{\text{Dy}}(z)$ is the amount of atomic Dy per unit length (m^{-1}) present in the cross-section at the axial position z [73]. Fitting this equation from the measured $N_{\text{Dy}}(z)$ yields the fitting parameters a , b and c which take the temperature variation along the axis into account, and the corrected axial segregation parameter λ_c . This parameter, λ_c , is determined by the ratio of the amount of convection and diffusion. Convection increases with Hg pressure, radius and gravity, and decreases at increasing input power [28, 33, 37].

6.3 Experimental setup

Five lamps have been investigated under hyper-gravity conditions (1–10 g). The goal of this study is to compare the various lamps, and to investigate the axial Dy distribution as a function of the amount of convection.

6.3.1 Lamps

The lamps we use are COST reference lamps (section 1.3.1) [27]. A drawing is given in figure 6.2. The diameter of the lamp burner is 8 mm and the burner height is 14–20 mm. The electrode distance is 8 or 16 mm. The lamps contain various amounts of Hg as buffer gas and contain DyI_3 as salt additive. The specifications of the lamps are given in table 6.1. For the calculation of the pressure an effective temperature of $T_{\text{eff}} = 3000$ K is assumed [33, 53].

Due to deterioration of the lamp, some deviations from the predicted values can be observed. Chemical analysis after x-ray fluorescence measurements by Nimalasuriya *et al* [38] show that during lamp operation Dy is being removed by chemical reactions at the wall, leaving an excess of free iodine. Before we started the measurements, lamps 1 and 3 had been operated for a longer time than lamp 2. Thus more deterioration is expected for these lamps 1 and 3.

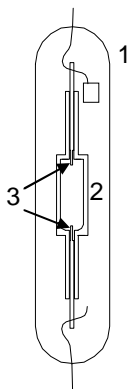


Figure 6.2: Schematic drawing of the lamp [37]: (1) outer bulb; (2) burner (diameter 8 mm, height between 14 and 20 mm); (3) electrodes (distance 8 or 16 mm).

Table 6.1: Lamp specifications. The diameter d and height h refer to the inner wall of the burner. When the cold zones behind the electrodes are taken into account, the pressures are about 20%–30% lower.

Lamp no.	d (mm)	h (mm)	Electrode dist. (mm)	Hg (mg)	DyI ₃ (mg)	p_{Hg} (\sim bar)	P (W)
#1	8	20	16	5	4	6	109.5, 129.9, 148.4
#2	8	20	16	7.5	4	9	109.5, 129.9, 148.4
#3	8	20	16	10	4	12	109.5, 129.9, 148.4
#4	8	15.5	8	6	4	10	89.5
#5	8	14	8	12	4	21	89.5

6.3.2 Centrifuge

As explained in sections 6.1 and 6.2.1, convection depends on gravity. A centrifuge was built to investigate the lamp under varying gravity conditions [37, 67]. It consists of a pivot, an arm and a gondola connected to the arm. The centrifuge has a diameter of about 3 m. The maximum rotation frequency is ~ 1.5 Hz, corresponding to $10g$ at the lamp position; g is the gravity on earth (9.81 m s^{-2}). The gravity vector at the lamp is always parallel to the lamp axis; the size of the vector parallel to the lamp axis is defined by a_z . The gondola contains the lamp and the setup. The measurement techniques are emission spectroscopy, webcam imaging and ILAS.

6.3.3 Measurement techniques

In this chapter, we present results of the ILAS measurements. ILAS yields the two-dimensional ground state atomic Dy column density. The ILAS technique has been discussed in chapter 4 and is summarized here.

A diode laser is used to scan over a wavelength range of ~ 0.1 nm around the absorption wavelength of 642.19 nm of ground state atomic Dy. The laser beam is expanded so that it illuminates the whole lamp burner. Part of the laser light is absorbed by the Dy atoms in the lamp. After passing the burner, the laser beam is imaged on a CCD camera.

The wavelength scan is performed in 65 steps. For each wavelength step the transmission is calculated for each position (x, z) in the lamp burner. In this way, we obtain a 3D matrix (wavelength, lateral position x , axial position z) with transmission data. From the wavelength dependence a transmission curve is constructed for each position. Next the density is obtained from this curve. We thus obtain the Dy density for each position (x, z) and end up with a 2D ground state atomic Dy column density profile.

Compared with emission, with ILAS this density is obtained directly and also non-radiating particles are measured. This means that also colder regions of the lamp can be measured, where emission spectroscopy cannot detect Dy atoms. Note that by using ILAS only ground state Dy atoms are measured. The ratio between Dy atoms in all states and Dy atoms in the ground state ranges from 1 to ~ 3 for 6000 K. This ratio β is given by the following semi-empirical formula based on the partition sum data of [76]:

$$\beta(T) = 0.815 + 0.0213 \exp(6.03 \times 10^{-4} \cdot (T + 2099)), \quad (6.9)$$

where the temperature T is in Kelvin.

The specifications of the ILAS technique are as follows. The spatial resolution is ~ 10 μm . The minimum detectable column density is 10^{17} m^{-2} , which in our lamps corresponds to a density of 10^{19} m^{-3} . The measurement time for one 2D profile is about 10 min. The measurement time is determined mainly by the download time of the CCD images. During the measurement, the data are stored locally on the computer in the centrifuge gondola. After the measurement is finished, the data are downloaded from the centrifuge computer and processed off-line. After the 2D ground state atomic Dy density images have been constructed, further analysis can be performed and the parameters as described in section 6.2.3 can be obtained.

By using ILAS, lamps with DyI_3 can be measured. The diameter of the lamp burner is fixed at 8 mm because of the optical system. However, the height of the lamp burner can be varied to maximum 20 mm.

Besides ILAS, the lamp is monitored by a simple webcam. From these images the colour segregation in the lamps can be observed directly.

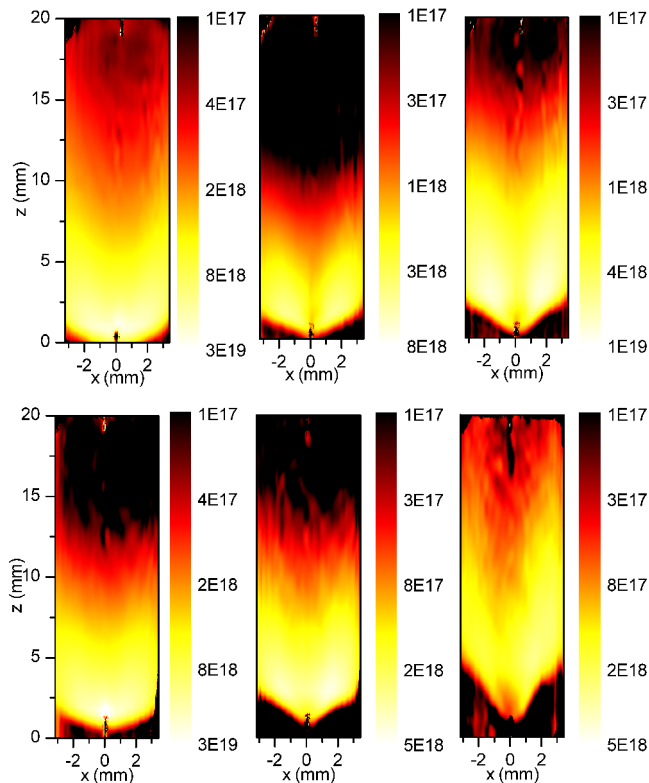


Figure 6.3: Lateral 2D ground state atomic Dy density profiles for the long lamps (20 mm burner length): lamp 1, 5 mg Hg (1g, 4g and 10g) and lamp 3, 10 mg Hg (1g, 4g and 10g), all at $P = 148.4$ W. The column densities are given in m^{-2} .

6.4 Results

Various lamps (different burner length, Hg pressure) under various input power have been investigated as a function of the amount of gravity. First, we show 2D column density profiles of ground state atomic Dy and discuss these in detail. In addition, webcam images are compared with the 2D profiles. Next two Abel inverted profiles are shown for lamp 1 (20 mm burner). The lamp numbers used in this section are given in table 6.1.

From the column 2D density profiles, several parameters are obtained as a function of gravity for the five lamps. For all lamps the values for the density inhomogeneity and the corrected axial segregation have been obtained for the power settings given in

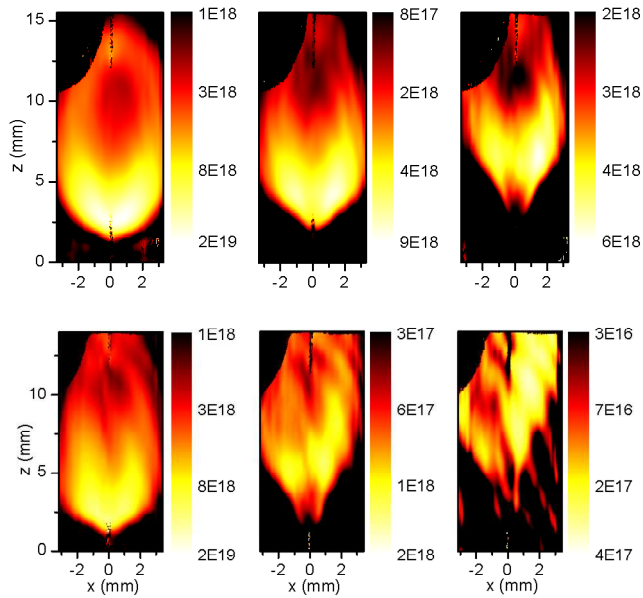


Figure 6.4: Lateral 2D ground state atomic Dy density profiles for the short lamps: lamp 4, 6 mg Hg ($1g$, $4g$ and $10g$) and lamp 5, 12 mg Hg ($1g$, $4g$ and $10g$), all at $P = 89.5$ W. The column densities are given in m^{-2} . The dark region at the top left is caused by an irregularity in the glass, which hinders the laser beam. Therefore no Dy atoms can be measured at this position.

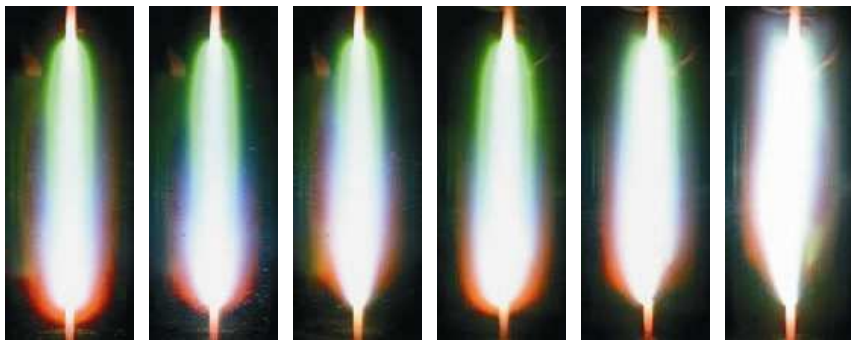


Figure 6.5: Webcam images for the long lamps: lamp 1, 5 mg Hg ($1g$, $4g$ and $10g$) and lamp 3, 10 mg Hg ($1g$, $4g$ and $10g$), all at $P = 148.4$ W.

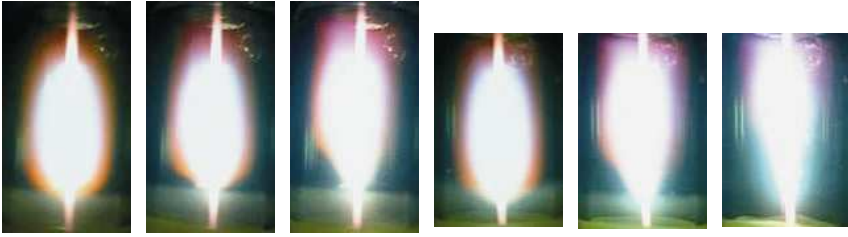


Figure 6.6: Webcam images for the short lamps: lamp 4, 6 mg Hg ($1g$, $4g$ and $10g$) and lamp 5, 12 mg Hg ($1g$, $4g$ and $10g$), all at $P = 89.5$ W. The irregularity in the glass at top right originates from the manufacturing process.

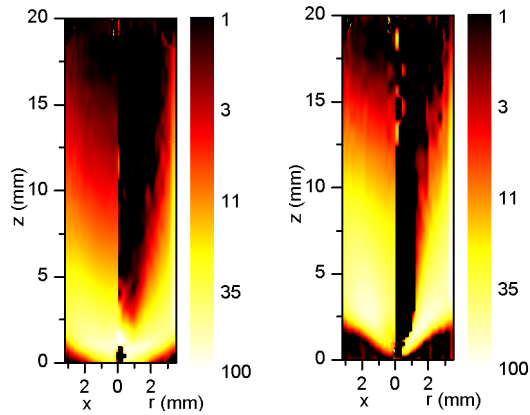


Figure 6.7: Abel inverted profiles lamp 1 (20 mm burner length), 5 mg Hg, 148.4 W: at the left side the lateral profile and at the right side the radial profile. The densities are in relative units on a logarithmic scale.

(left) $1g$, the lateral density scale ranges from 3×10^{17} to $3 \times 10^{19} \text{ m}^{-2}$ and the radial density scale from 3×10^{19} to $3 \times 10^{21} \text{ m}^{-3}$.

(right) $10g$, the lateral density scale ranges from 1×10^{17} to $1 \times 10^{19} \text{ m}^{-2}$ and the radial density scale from 1×10^{19} to $1 \times 10^{21} \text{ m}^{-3}$.

table 6.1. In this chapter, we focus on the trends of the gravity dependence of these parameters for different Hg pressures and input power.

6.4.1 2D profiles

Figures 6.3 and 6.4 show 2D profiles of ground state atomic Dy for the various lamps. Figures 6.5 and 6.6 show the webcam images for the lamps. The ground state atomic

Dy density at the top and the bottom of the lamp is too low to be measured (below the noise level). Therefore black parts are observed at the top and bottom of the lamp. The irregular flame-like pattern close to the top of the lamp is also caused by noise [37].

In the density profiles at the bottom no Dy atoms are present, caused by the low temperature. The arc angle at the bottom is defined by the angle between the visible arc and the bottom plane of the lamp burner. Because the axial temperature profile changes with gravity, the angle also changes with gravity. The arc angle is minimal at maximum axial segregation.

For lamps 1–3 (long, 20 mm burner) higher gravity means less segregation; better mixing is observed (right side of the Fischer curve [28, 73]). At $1g$ the ground state atomic Dy density is the highest at the spot around the bottom electrode. The electrode temperature is about 2800 K [70] and at this temperature the atomic Dy density is the highest [73] due to the chemical equilibrium. For lower temperatures the equilibrium shifts towards molecules, whereas at higher temperature the Dy atoms are ionized. At higher gravity the convection flow causes cooling in the region around the electrode and the local atomic Dy density is decreased. At the very bottom of the lamp the temperature is too low for Dy atoms to exist.

For lamps containing 5 mg Hg, the Dy density is higher than the lamp containing 10 mg. This is because at 10 mg the radiation loss by Hg atoms is larger, thus the temperature of the cold spot is lower than at 5 mg Hg. This causes a lower overall Dy density.

When we take a look at the short lamps 4 and 5, we see that above $3g$ the maximum white light output is observed at the top of the lamp. This is most pronounced for lamp 5. The Dy density is also the highest at the top. This is caused by the temperature effect (section 6.2.1 [73]), due to the strong convection. At the bottom the chemical equilibrium shifts from atoms to molecules, causing a smaller atomic Dy density.

For the short lamp lamp 5, the overall density at $10g$ is much lower than at $1g$ and $4g$, due to cooling by the strong convection. As stated in section 6.3.3, the detectable column density is about 10^{17} m^{-2} . The minimum value shown in the 2D profile is $3 \times 10^{16} \text{ m}^{-2}$, but the image is noisy and some artefacts are seen. Nevertheless it is clear from this image that most of the atomic Dy is observed at the top of the lamp.

6.4.2 Abel inversion

The column density profiles can be inverted into radial profiles by means of Abel inversion as explained in section 6.2.2. As an example, the Abel inverted profiles are derived for lamp 1 (20 mm burner length). These profiles consist of 16 rings. Figure 6.7 shows these radial profiles together with the lateral profiles, for $1g$ and $10g$. At $10g$ better mixing is observed and the maximum density moves outward. In the centre almost no atomic Dy is present, because the temperature is too high and mainly ions are present.

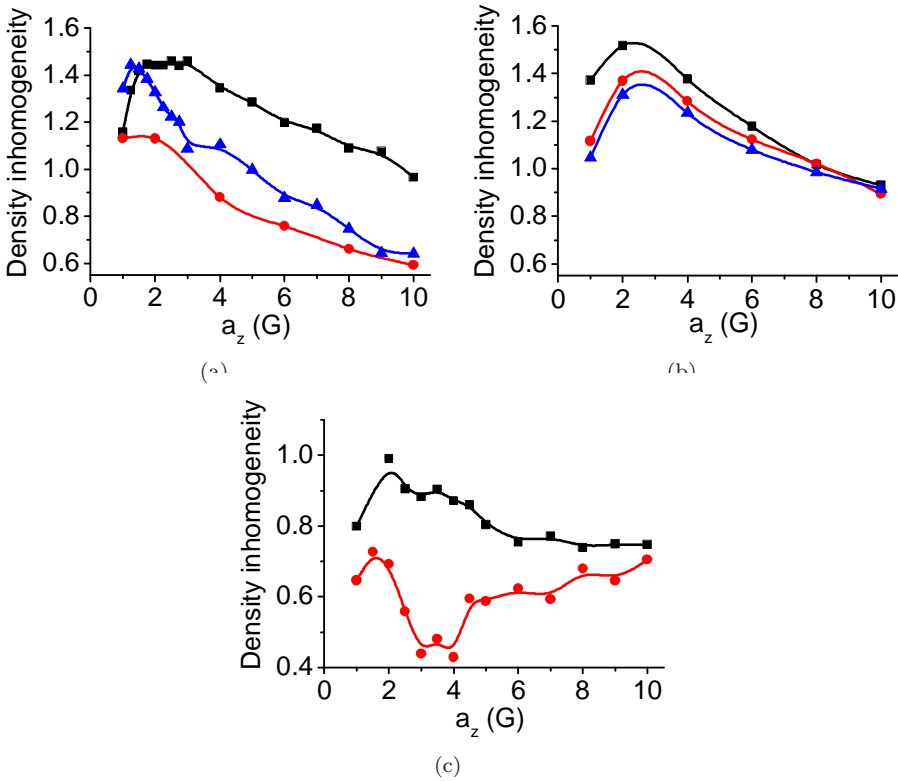


Figure 6.8: Density inhomogeneity α , as a function of the gravitational acceleration a_z . The lines are shown to guide the eye.

(a) 20 mm lamps, pressure series, 148.4 W: ■ lamp 1 (5 mg Hg); ● lamp 2 (7.5 mg Hg); ▲ lamp 3 (10 mg Hg).

(b) 20 mm lamp 1, input power series, 5 mg Hg: ■ 109.5 W; ● 129.9 W; ▲ 148.4 W.

(c) 15 mm lamps, pressure series, 89.5 W: ■ lamp 4 (6 mg Hg); ● lamp 5 (12 mg Hg).

6.4.3 Density inhomogeneity

The axial density inhomogeneity parameter is determined by the ratio between convection and diffusion and by the temperature effect (section 6.2.3). Figure 6.8 shows the density inhomogeneity α of ground state Dy atoms for various Hg pressures and for various power, as a function of gravity. The ratio between atomic Dy in the ground state and all states is given in equation (6.9). For the calculation only the part between $|x| = 0.5\text{--}3.0$ mm is taken into account, because of noise at the centre (electrodes) and close to the burner wall.

The density inhomogeneity should decrease with increasing Hg pressure, because the convection speed is proportional to the pressure. Our lamps are at the right-hand side of the Fischer curve, thus increasing the convection means decreasing the amount of axial segregation [28, 33, 37, 73]. The decrease is observed in figure 6.8(a); however, the values for the long lamps, 2 and 3 (20 mm burner length), are close to each other. The density inhomogeneity α should be smaller for lamp 3 than for lamp 2, because of the higher pressure. However, this is not the case. An explanation is that the temperature effect is more pronounced for lamp 3 than for lamp 2, increasing the density inhomogeneity for lamp 3 more than for lamp 2. Furthermore increasing the power results in increasing the convection speed [23, 73]. This causes the density inhomogeneity to decrease with increasing power; this is observed in figure 6.8(b).

The maximum density inhomogeneity shifts towards higher gravity for lower Hg pressure. The convection speed is proportional to $v \sim p_{\text{Hg}}^2 g$. The axial segregation is determined by the ratio of the rate of convection to the rate of diffusion [28, 42, 73]. For a constant convection speed, the amount of gravity g should decrease when increasing the pressure. Furthermore the density inhomogeneity decreases with increasing gravity, because we are at the right-hand side of the Fischer curve.

At $1g$, the density inhomogeneity is lower for the short lamps 4 and 5 (figure 6.8(c)) than for the long lamps 1–3. At higher gravity, axial segregation is still present. The axial segregation (λ_c in equation (6.8)) is smaller (right side of the Fischer curve), but the temperature effect becomes dominant and cancels the smaller Fischer segregation. At $3g$, α is minimal for the short lamp 5. Thus at $1g$ the highest density is found at the bottom due to the axial segregation, and at $10g$ the highest density is found at the top due to the temperature effect. Around $3g$ the lamp is in between these two situations, giving the most homogeneous Dy distribution. This is in agreement with the 2D profiles (figure 6.4) and the webcam images (figure 6.6), where we see that above $3g$ the atomic Dy density is the highest at the top of lamp 5.

6.4.4 Corrected axial segregation parameter

In the density profiles (figures 6.3 and 6.4) it is observed that no ground state Dy atoms are present at the bottom of the lamp due to the low temperature. This causes the arc angle that is observed near the bottom. For this part in the lamp, no corrected axial segregation parameter λ_c can be fitted according to equation (6.8). The same arc angle can also be observed at the top of the lamp; also at this position no fit can be performed.

The solution to use a larger region for fitting the parameter is as follows. First the density plot is straightened by subtracting the contour line (defined at one-fifth of the maximum density) from the z coordinate. For the calculation of the contour only the part between $|x| = 1.0\text{--}2.5$ mm is taken into account. Next the corrected axial segregation parameter is fitted. This gives the same value for λ_c according to equation (6.8). In conclusion, the arc angle correction yields the same axial segregation

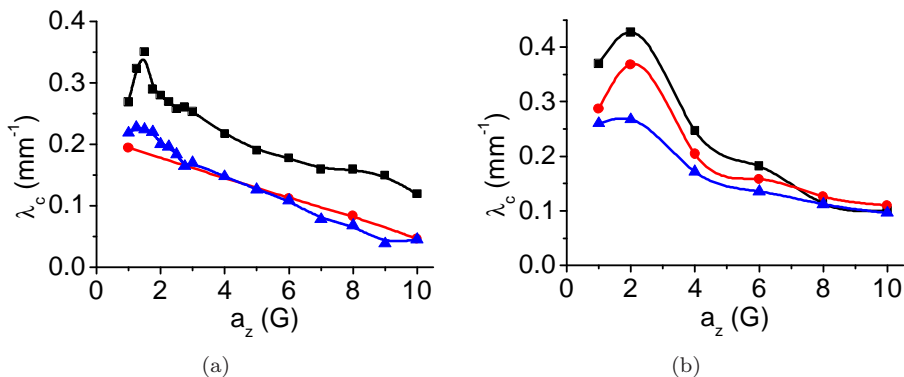


Figure 6.9: Corrected segregation parameter λ_c , as a function of the gravitational acceleration a_z . The lines are shown to guide the eye.
 (a) 20 mm lamps, pressure series, 148.4 W: ■ lamp 1 (5 mg Hg); ● lamp 2 (7.5 mg Hg); ▲ lamp 3 (10 mg Hg).
 (b) 20 mm lamp 1, input power series, 5 mg Hg: ■ 109.5 W; ● 129.9 W; ▲ 148.4 W.

parameter, but a larger z range of the lamp can be fitted.

In figure 6.9 the trends of the corrected axial segregation parameters λ_c are shown. The values differ from the uncorrected values as shown in the paper by Nimalasuriya *et al* [38], especially for higher gravity and for 10 mg Hg (lamp 3, long burner). The corrected values are at higher gravity lower than in [38] and are in closer agreement to the the $1/g$ dependence predicted by E. Fischer [28, 73]. Furthermore the segregation decreases more strongly with pressure than in the earlier publication.

The axial segregation decreases with increasing pressure (figure 6.9(a)). The curves also show a decrease in axial segregation when increasing the power (figure 6.9(b)). This is because increasing the power increases the temperature gradient and thus the convection speed. When we are at the right-hand of the Fischer curve, increasing the amount of convection means decreasing the amount of axial segregation.

In general, the corrected axial segregation and the square of the density inhomogeneity show the same dependence of pressure, gravity and input power. When the temperature effect is not dominant, λ_c and α^2 should follow the same trends. An example is given in figure 6.10, where these two parameters are compared for lamp 3 (20 mm burner length) at 148.4 W. These parameters show indeed good agreement with each other.

When figure 6.9(a) is compared with figure 6.8(a), it is observed that lamps 1–3 show a decreasing λ_c with increasing pressure, whereas for lamps 2 and 3 α increases with increasing pressure. The latter is explained by the stronger temperature effect for lamp 3, increasing the axial density inhomogeneity.

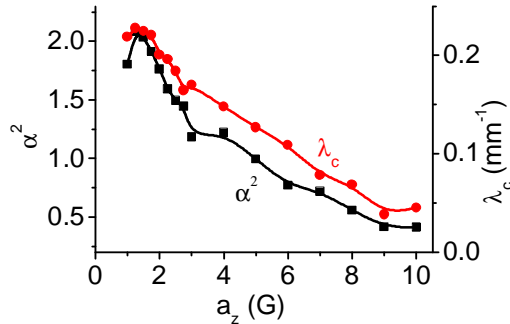


Figure 6.10: Comparison between the square of the density inhomogeneity (α^2) and the corrected segregation parameter λ_c for the long lamp 3, 10 mg Hg, 148.4 W, as a function of the gravitational acceleration a_z : ■ α^2 (left axis); ● λ_c (right axis). The lines are shown to guide the eye.

For the short lamps 4 and 5 the temperature effect is dominant. In this case, the density $N_{\text{Dy}}(z)$ is governed mainly by the temperature (second) part in equation (6.8) and the fitting of the variable λ_c is inaccurate. Therefore, λ_c is not shown for these lamps.

In conclusion, the corrected axial segregation parameter is only valid if the temperature effect does not dominate. This corrected parameter follows the behaviour predicted by E. Fischer better than the uncorrected Fischer parameter.

6.5 Conclusions

MH lamps containing DyI_3 as salt additive have been measured by ILAS. 2D ground state atomic Dy lateral density profiles have been obtained for lamps with various Hg pressures, various burner lengths (20 mm and ~ 15 mm) and various input power. The lamps have been measured in a centrifuge, which yields a gravity between 1 and 10g. The 2D density profiles have been compared with webcam images. For the shorter lamps (~ 15 mm burner length), at 10g the highest Dy density is found at the top of the lamp, caused by the strong axial temperature gradient.

As an example, two lateral density profiles have been inverted to radial profiles. The radial profiles show a dip of atomic Dy density in the centre.

From the 2D images, the density inhomogeneity and corrected axial segregation parameters have been derived. The axial segregation parameter was corrected for the temperature effect. For lamps with a burner length of 20 mm the corrected segregation parameter follows better the predicted behaviour by E. Fischer than the uncorrected parameter as used in an earlier publication. For short (height ~ 15 mm) lamps the

temperature effect is dominant. Because of this, for the short lamp with high Hg pressure (12 mg) at 10g the highest density is found at the top of the lamp. If the temperature effect is dominant, the corrected segregation parameter is not relevant to describe the axial segregation in the lamp.

Acknowledgements

The authors are grateful to all participants in the ARGES project for their contributions, especially the General Technical Department of the Eindhoven University of Technology for building the centrifuge, and Senter-Novem (project EDI 03146), SRON [66] and the Dutch Ministries of Research and Education as well as Economic Affairs for funding the research.

Emission spectroscopy for characterizing metal-halide lamps

Abstract.

The metal-halide (MH) lamp shows an unwanted axial non-uniform distribution of the metal additives when burning in the vertical position, which is caused by the interplay between convection and diffusion. Various MH lamps are investigated by means of emission spectroscopy under varying gravity conditions (1–10*g*) in a centrifuge. The method yields spectra, axial inhomogeneity parameters and axially integrated intensities. The method is easier than methods used before on the same type of lamp. Measurements on lamps with DyI₃ as salt filling are used as a calibration of the setup. After comparison with the earlier measurements, we conclude that the new emission spectroscopy is valid for characterization of MH lamps. Next, we apply the method on commercial lamps (Philips MASTER CosmoWhite). For these lamps, in addition NaI densities at the wall and axial temperature profiles are obtained by using self-reversed lines of Na and Hg, respectively.

This chapter has been adapted from [A.J. Flikweert, T. Nimalasuriya, G.M.W. Kroesen, M. Haverlag and W.W. Stoffels, *Emission spectroscopy for characterizing metal-halide lamps*, J. Phys. D: Appl. Phys. **41** (2008) issue 18].

7.1 Introduction

In this chapter we present results from emission spectroscopy measurements for characterizing MH lamps. The measurement technique is an addition to imaging laser absorption spectroscopy (ILAS) measurements (chapter 4) and absolute line intensity (ALI) measurements performed on the same type of lamp before [34, 37] and x-ray absorption spectroscopy measurements performed by Nimalasuriya *et al* [77] on commercial lamps, which derive absolute number densities and other plasma parameters. The emission spectroscopy method used in this chapter is easier than ILAS, ALI and x-ray absorption spectroscopy and can be used to characterize commercially available lamps.

The MH lamp is a high intensity discharge lamp with a good colour rendering index of ~ 80 and a high luminous efficacy of about 100 lm W^{-1} [2, 3, 21–26, 35, 39, 42]. The lamp is used in street lighting, stadium lighting, city beautification and shop lighting.

The lamp contains a buffer gas (usually Hg) and a mixture of metal additives dosed as MH salts. The additives improve the colour rendering of the lamp. Additives that we use are DyI_3 and the filling for commercial lamps (Philips MASTER CosmoWhite: iodides of Ca, Ce, Tl, Na) [78]. When the lamp is burning in the vertical position, axial segregation of the salt additives occurs. The non-uniform light output caused by axial segregation limits the application, because it has a bad influence on the efficiency and the colour rendering of the lamp. The non-uniform distribution of additives is caused by the combination of convection and diffusion in the lamp.

The axial segregation of the additives has been described by E. Fischer [28]. The model assumes an exponential decrease of the axial Dy density n_{Dy} with increasing height z in the lamp $n_{\text{Dy}}(z) \sim \exp(-\lambda z)$. The amount of axial segregation λ as a function of the ratio between the convection and diffusion speeds is shown in figure 7.1. The Fischer model is valid for infinitely long lamps with a constant axial temperature profile only. This is not the case for our lamps and therefore a semi-empirical extended model has been proposed for our lamps in chapter 5 [73]. The model takes the temperature gradient along the lamp axis into account and is valid for atomic Dy, whereas the Fischer model is valid for the elemental Dy density. Changing the temperature changes the chemical equilibrium between atoms and molecules. We use the axial inhomogeneity parameter α , which can be used to describe any axial non-uniformity in a lamp. In our case we want to describe the non-uniformity of emission and use it to describe the axial intensity inhomogeneity of several emission peaks.

Convection is induced by gravity. In the past several experiments under varying gravity conditions have been carried out. Beside lab experiments (chapter 2, [32, 34, 35, 50]), the lamp was sent to the International Space Station (micro-gravity $0g$; in this chapter the amount of acceleration is given in terms of $g = 9.81 \text{ m s}^{-2}$) [41]. Furthermore parabolic flights were carried out ($0-2g$, for periods of about 20 s; chapter 3) [33, 67]. More recently a centrifuge was built, in which we can achieve gravity conditions from $1-10g$ (chapters 4 and 8) [37–39]. The additive distribution in the

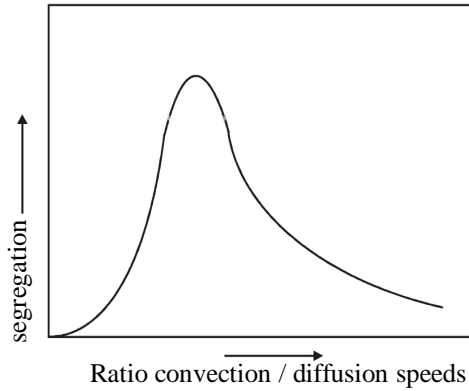


Figure 7.1: The Fischer curve shows the axial segregation as a function of the ratio between the convection and diffusion speeds [28, 32, 67, 73]. In our case the amount of convection is changed by changing the gravitational acceleration. The DyI_3 lamps we use are around the maximum of the curve.

Table 7.1: Lamp specifications. The diameter and height refer to the inner wall of the burner. The CosmoWhite salt filling consists of a mixture of Ca, Ce, Tl and Na iodides.

Lamp name	Burner material	Diameter (mm)	Height (mm)	Electrode dist. (mm)	Hg (mg)	Salt filling
Q1	Quartz	8	20	16	5	4 mg DyI_3
Q2	Quartz	8	20	16	7.5	4 mg DyI_3
Q3	Quartz	8	20	16	10	4 mg DyI_3
Q4	Quartz	8	15.5	8	6	4 mg DyI_3
Q5	Quartz	8	14	8	12	4 mg DyI_3
Q6	Quartz	4	22	16	0.7	2.5 mg DyI_3
Q7	Quartz	4	22	16	2.5	2.5 mg DyI_3
C1	PCA	5.3	26.0	23.0	2.5	CosmoWhite
C2	PCA	9.2	13.3	9.0	14.4	CosmoWhite

lamp has been measured by means of ALI measurements [34, 35, 38, 41] and ILAS (chapters 4 and 8) [37, 39, 67, 71, 72]. By using ALI absolute number densities of Dy and Hg, and temperature profiles were obtained. ILAS yields the ground state atomic Dy density distribution in the lamp. When using ALI, the setup needs to be calibrated to obtain absolute intensities. Temperatures are calculated using Boltzmann plots [31]. This method is complicated, time consuming and sensitive to errors in the transition

probabilities. The ILAS technique also yields absolute number densities, but due to the optics and the laser wavelength ILAS is limited to quartz lamps with a fixed diameter of 8 mm and DyI₃ as salt additive.

We want to have an easier, faster method to characterize MH lamps. Therefore we perform emission spectroscopy measurements on lamps that have been measured by ILAS and ALI. We validate the fast emission spectroscopy method by comparing the measurement results with the results from earlier measurements, so the emission spectroscopy can be used to characterize commercially available lamps.

In this chapter we present a method based on emission spectroscopy, which determines the axial additive inhomogeneity in the lamps in a faster way than ILAS and ALI. The setup is not only limited to the fixed diameter, the DyI₃ salt filling or the quartz burner. Lamps with different salt fillings and burner materials (quartz and poly-crystalline alumina, PCA) can be measured. This allows us to investigate also commercial lamps like the Philips MASTER CosmoWhite.

The structure of this chapter is as follows. First the setup is discussed, the lamps that are measured, the centrifuge to vary the gravity conditions, and the emission spectroscopy setup. Next, the analysis of the measurement data is discussed. We show results for the lamps with DyI₃, which are compared with results obtained by ILAS before [72]. Finally the results are shown for the commercially available Philips MASTER CosmoWhite lamp.

7.2 Experimental method

Lamps with various geometries, salt fillings and wall materials (quartz and PCA) are investigated by means of emission spectroscopy. This has been done in the centrifuge, where we can achieve gravity conditions between 1*g* and 10*g*.

7.2.1 Lamps

The specifications of the lamps are given in table 7.1. The lamps all have a fitting according to the MH reference lamp developed within the European COST action program 529 [27], which is required for use of the lamps in the centrifuge setup (see also section 1.3.1). A schematic picture of the MH reference lamp is given in figure 7.2(a).

The lamps have different Hg pressures and different salt additives: DyI₃ and the commercial Philips CosmoWhite filling (iodides of Ca, Ce, Tl, Na). Lamp C1 (see table 7.1) contains the burner of the Philips MASTER CosmoWhite 140W lamp. Lamp C2 also has the CosmoWhite filling, but has a different geometry.

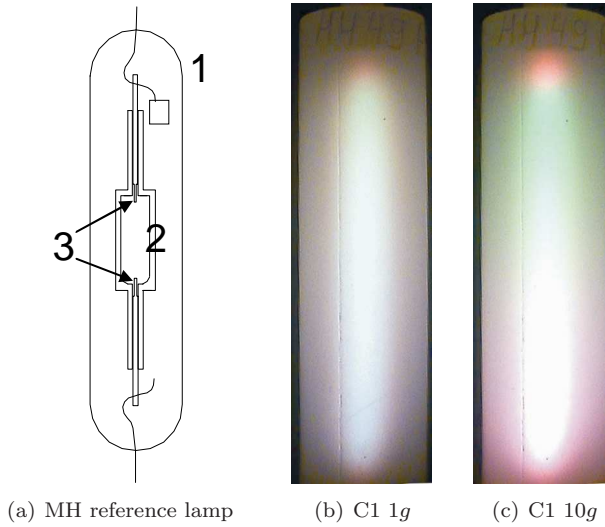


Figure 7.2: (a) Schematic drawing of the MH reference lamp [27, 37]: (1) outer bulb; (2) burner (diameter 8 mm, height between 14 and 20 mm); (3) electrodes (distance 8 or 16 mm). (b)–(c) Webcam images of the Philips CosmoWhite lamp C1, 141.6 W at $1g$ and $10g$. The axial colour segregation is clearly seen. For this lamp, increasing the gravitational acceleration thus enhances convection, and increases the axial colour segregation. This means that the lamp is at the left-hand side in the Fischer curve in figure 7.1.

7.2.2 Centrifuge

The amount of convection in the lamps depends on gravity [33, 37–39, 41, 67, 71, 72]. A centrifuge was built to investigate the lamp under varying gravitational accelerations. The centrifuge has a diameter of about 3 m. It consists of a pivot, an arm, and a gondola connected to the arm. The gondola contains the lamp and the emission spectroscopy setup. The maximum rotation speed is ~ 1.5 Hz, corresponding to $10g$ at the lamp position.

Figure 7.3 shows a drawing of the centrifuge arm with gondola. The vectors of the acceleration working on the lamp are shown; the total gravitational acceleration at the lamp \vec{a}_{tot} is the vector sum of the gravity on earth \vec{g}_z and the centrifugal acceleration \vec{a}_r . The gravity vector \vec{a}_{tot} at the lamp is always parallel to the lamp axis; the size of the vector parallel to the lamp axis is defined by $|\vec{a}_{\text{tot}}| = a_z$.

Figures 7.2(b) and (c) show the effect of the gravity conditions on the axial colour segregation, for the commercial Philips CosmoWhite lamp C1.

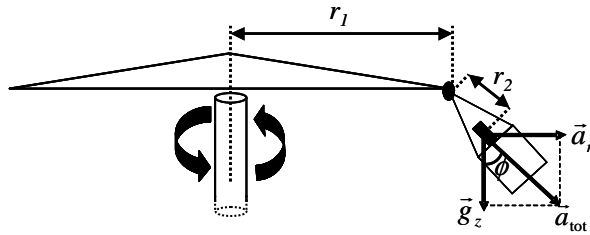


Figure 7.3: Schematic representation of the centrifuge arm with the gondola. When rotating, the gondola swings out with an angle ϕ . The acceleration vectors at the position of the lamp are indicated [37, 38, 67]. The size of the vector parallel to the lamp axis is defined by $|\vec{a}_{\text{tot}}| = a_z$, which is used in the rest of this chapter.

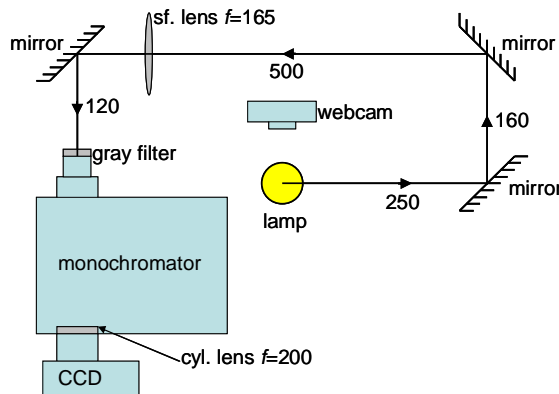


Figure 7.4: Top view of the emission setup. The lamp is focused on the entrance slit (in the vertical position) of the spectrometer. At the 2D CCD chip the wavelength is in the horizontal and the axial position of the lamp in the vertical direction. All measures are given in millimetres. The setup is mounted on the centrifuge gondola; mirrors are used to increase the path length between the lamp and entrance slit.

7.2.3 Emission spectroscopy setup

The lamps are characterized by means of emission spectroscopy. Emission spectroscopy in the centrifuge has been discussed in detail by Nimalasuriya *et al* [38]. We do not perform ALI measurements, but use the intensity of the line emission peaks (peak area) for the analyses without absolute number calibration.

The setup is shown schematically in figure 7.4. The spectrometer is a Yvon-Jobin 0.25 m monochromator. The lamp is focused on the entrance slit of the spectrometer by three mirrors and a lens. The entrance slit (width $100 \mu\text{m}$) of the spectrometer is in the

Table 7.2: Emission lines that have been investigated.

Element	λ (nm)
Dy	642.19
Hg	546.07
Ca	442.67
Ce	556.5
Tl	535.05
Na	doublet 589.0 / 589.6

vertical direction; in this way an axial profile of the lamp is imaged on the spectrometer slit. A neutral density filter (transmission 10^{-3}) is placed in front of the slit. At the exit of the spectrometer a CCD camera (SBIG ST-2000 XM) [60] is attached. The horizontal position at the CCD camera corresponds to the wavelength and the vertical position to the axial position in the lamp. The wavelength range that can be imaged on the CCD camera is ~ 30 nm. Because the spectrometer was originally not meant for imaging purposes on a 2D CCD camera, the wavelength and the axial position do not have the same focal plane at the exit of the spectrometer. To correct for this, a cylindrical lens with $f = 200$ mm is placed just before the exit of the spectrometer. In this way, the setup is aligned so the wavelength and axial focal planes are both at the position of the CCD chip. The calibration of the wavelength is done using a Hg/Ar calibration lamp. The spectral resolution of the setup is 0.02 nm per pixel and the instrumentally observed line width is ~ 0.2 nm.

A typical image obtained by the CCD camera is shown in figure 7.5. The shutter time of the camera is set between 100 and 4000 ms, depending on the maximum peak intensity in the spectrum. At the CCD image, the wavelength is in the horizontal direction and the axial position in the lamp is in the vertical direction. A spectrum can be determined for a particular axial position, as is indicated in figure 7.5. After normalization for the shutter time and correction for the spectral response of the system by a tungsten ribbon lamp, the intensities of different spectra can be compared. For one particular wavelength, an axial intensity profile is obtained. In this example, the axial intensity profile for the 642.19 nm peak of atomic Dy is shown. This can be done for each wavelength of interest.

For the lines of interest, the integrated line intensity and the maximum intensity of the peak are determined. These values are corrected for the baseline of the background radiation. For the line intensity, the area under the peak is calculated from the range where the intensity is above 10% of the peak height. The investigated emission lines for the various lamps are shown in table 7.2. The Na doublet lines are used for the density calculation from self-reversed lines as is explained in section 7.3.2.

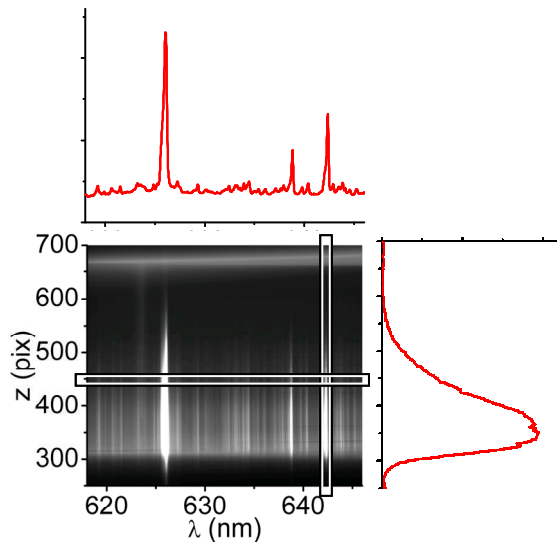


Figure 7.5: CCD image of lamp Q3 (10 mg Hg, 4 mg DyI₃), 148.4 W at 1*g*. In the CCD image, the horizontal axis is the wavelength λ and the vertical axis is the axial position z in the lamp. The spectrum (top graph) is taken around $z = 450$ and in the graph at the right the intensity of the 642.19 nm peak is plotted as a function of the axial position.

The lamps are driven by a Luxmate DimTronic ballast with a square wave voltage of 120 Hz. This frequency corresponds to a period of 8.33 ms. As mentioned, the shutter time of the CCD camera is set between 100 and 4000 ms. This time is much longer than the period of the ballast, so phase dependent fluctuations are averaged out during one camera exposure.

7.3 Analysis

From the emission spectroscopy measurements, spectra are obtained for each axial position in the lamp. From these spectra, we want to determine the non-uniformity of the emission of the various lamp species over the axial position in the lamp. Hereto we introduce the axial line intensity inhomogeneity. Next, the Na density is derived for each axial position using a self-reversed Na-D line. Finally we verify an existing method to calculate the axial temperature profile by using self-reversed lines of Hg.

7.3.1 Axial line intensity inhomogeneity

We want to have a measure for the axial non-uniformity of the light output for different particles in the lamp. In section 5.3.3 [73] the inhomogeneity parameter α has been introduced. In most cases the square of the inhomogeneity (α^2) follows the same trend as the Fischer parameter, which describes the amount of axial segregation. Figure 7.1 shows the amount of axial segregation as a function of the amount of convection.

The inhomogeneity parameter describes the axial inhomogeneity of any lamp property Q . In our case $Q(z)$ denotes the line intensity (area under the peak) of a spectral line, or the density, at the axial position z . The axial inhomogeneity, which is a measure for the axial non-uniformity of property $Q(z)$, is given by

$$\alpha = \sqrt{\frac{1}{H} \int_0^H \left(\frac{Q(z) - \bar{Q}}{\bar{Q}} \right)^2 dz}, \quad (7.1)$$

where H is the lamp height and \bar{Q} is the averaged value of $Q(z)$ over the lamp height:

$$\bar{Q} = \frac{1}{H} \int_0^H Q(z) dz. \quad (7.2)$$

7.3.2 Density calculation using self-reversed lines

From the contour of a self-reversed line of a radiating particle, the density can be calculated for that particle [79–81]. This density calculation is an empirical method.

In our case, we use the Na-D line (589.0 and 589.6 nm). The distance $\Delta\lambda_{\text{Na}}$ between the maximum left λ_1 and the maximum right λ_2 of this wavelength is a measure for the Na density. Hoek *et al* [79] obtained

$$[\text{NaI}]_{\text{w}}(z) \propto (\Delta\lambda_{\text{Na}}(z) - 0.6)^{1.43}, \quad (7.3)$$

where $[\text{NaI}]_{\text{w}}(z)$ is the NaI density at the wall for each axial position z , $\Delta\lambda_{\text{Na}}(z) = \lambda_1 - \lambda_2$ (in nm) is the distance between the two maxima at the axial position z and 0.6 nm is the distance between the two Na-D lines. In this equation the Hg density is assumed to be independent of the axial position. The axial density distribution obtained by this equation can also be analysed by means of the inhomogeneity parameter α (equation (7.1)), where $Q(z) = [\text{NaI}]_{\text{w}}(z)$. In this case, the parameter α describes the axial density inhomogeneity at the wall and not at the centre of the burner. We assume that the atomic Na density at the centre of the burner follows the same trend and then α is also a measure for the axial Na density inhomogeneity at the centre.

7.3.3 Temperature calculation using self-reversed lines

The temperature can be determined using self-reversed lines. Wesselink *et al* [82] presented a variation on Bartels' method [80, 81] for determining the temperature of

Table 7.3: Parameters of the self-reversed Hg lines used to determine the temperature [44].

Peak number	λ (nm)	E_m (eV)	E_j (eV)	MY
1	435.83	4.887	7.731	0.7062
2	546.07	5.461	7.731	0.7660

an optically thick plasma. Here we want to verify this method for our lamps and setup, and want to have at least a qualitative measure for the axial temperature profile in the CosmoWhite lamp C1.

For the temperature determination using the Wessellink method, we need two self-reversed lines with wavelengths λ_1 and λ_2 . The intensity ($\text{W m}^{-2} \text{sr}^{-1} \text{nm}^{-1}$) at the top of the first line I_{λ_1} and the intensity at the top of the second line I_{λ_2} are determined from the emission spectra. According to this method the maximum temperature T_m within the line-of-sight is given by [82]

$$T_m = \frac{hc(\lambda_1^{-1} - \lambda_2^{-1})}{k} \times \frac{1}{\ln(I_{\lambda_2}/I_{\lambda_1}) + \ln(Y_1 M_1/Y_2 M_2) + 5 \ln(\lambda_2/\lambda_1)}, \quad (7.4)$$

where h is the Planck constant, k is the Boltzmann constant, c is the speed of light, and Y_1, Y_2 and M_1, M_2 are the grayness factors of the first and second line. The values for Y and M are [80–85]

$$M_\infty = \sqrt{\frac{E_m}{E_j}} \quad (7.5)$$

and

$$Y_\infty = 0.736 + 0.264q^2, \quad (7.6)$$

where

$$q = \frac{6}{\pi} \tan^{-1} \frac{M_\infty^2}{\sqrt{1 + 2M_\infty^2}}. \quad (7.7)$$

In these equations E_m and E_j are the lower and upper energy level, respectively. Note that the factors in the denominator (e.g. the factor 5) in equation (7.4) are empirical; therefore the temperature T_m should be considered as a qualitative parameter. The obtained values for our lamp C1 should be used to indicate trends as a function of the axial position in the lamp and as a function of the gravitational acceleration.

In table 7.3 the values needed for the temperature calculations are given.

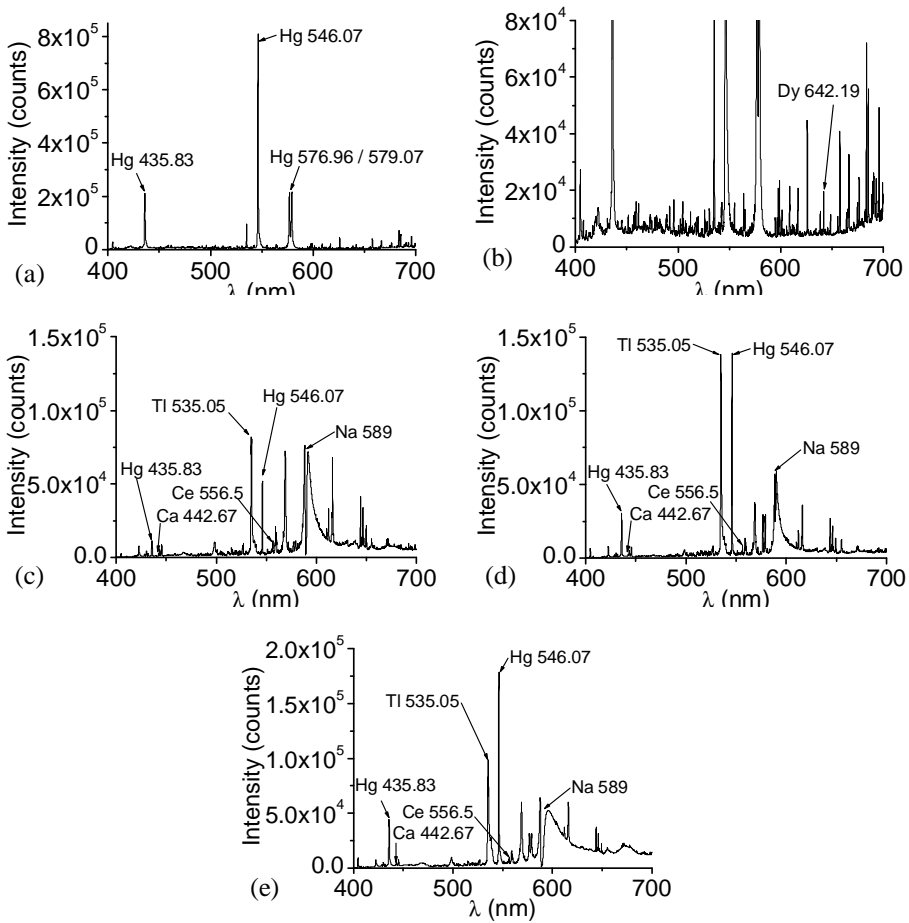


Figure 7.6: Spectra for various lamps, obtained by optical emission spectroscopy. The intensity is integrated over the lamp axis and normalized for a shutter time of 1000 ms. The main peaks are indicated (see also table 7.2). (a) 1g, lamp Q3 (10 mg Hg, 4 mg DyI₃), 148.4 W. (b) 1g, lamp Q3 (10 mg Hg, 4 mg DyI₃), 148.4 W; same spectrum as (a), with a different intensity scale to display the Dy peaks. (c) 1g, lamp C1 (MASTER CosmoWhite), 141.6 W. (d) 10g, lamp C1 (MASTER CosmoWhite), 141.6 W. (e) 1g, lamp C2 (CosmoWhite filling, short lamp), 148.4 W.

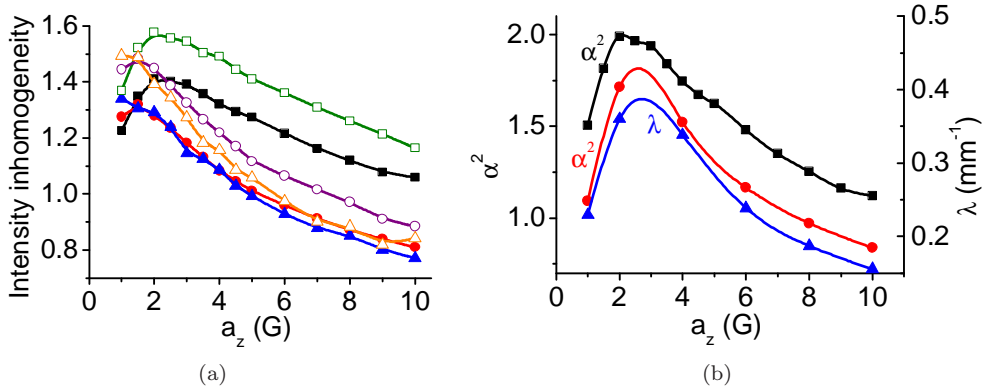


Figure 7.7: (a) Axial intensity inhomogeneity α (equation (7.1)) of Dy 642.19 nm for lamps Q1–Q3 (different Hg pressures, different input power), as a function of the gravitational acceleration a_z . The lines are shown to guide the eye: lamp Q1 (5 mg Hg) ■ 148.4 W, □ 129.9 W; lamp Q2 (7.5 mg Hg) ● 148.4 W, ○ 129.9 W; lamp Q3 (10 mg Hg) ▲ 148.4 W, △ 129.9 W. (b) Square of the axial inhomogeneity (α^2) (equation (7.1)) and the axial segregation λ of Dy 642.19 nm for lamp Q1 (5 mg Hg, 4 mg DyI₃), 148.4 W, as a function of the gravitational acceleration a_z , comparison between emission spectroscopy, ILAS and ALI. The curves for lamps Q2 and Q3 show the same trends and are not shown for clarity [72]. ■ Emission spectroscopy (square of the intensity inhomogeneity; left axis); ● ILAS (square of the density inhomogeneity; left axis); ▲ ALI (axial segregation λ ; right axis) [38].

7.4 Results

The lamps described in table 7.1 have been investigated. Some of the axially integrated spectra of these lamps, under $1g$ and $10g$, are shown in figure 7.6 and are discussed in more detail later.

First we discuss lamps with DyI₃ as salt additive. Next lamps with the commercial Philips CosmoWhite filling are discussed. In the figures a_z is the acceleration parallel to the lamp axis; the unit G is defined as 9.81 m s^{-2} .

7.4.1 Lamps with DyI₃ filling

Spectra

Various lamps with DyI₃ as salt filling have been measured. The spectrum of lamp Q3 (10 mg Hg), at $1g$, is shown in figures 7.6(a) and (b). In the second figure the intensity scale is different to display the Dy peaks. The spectra are axially integrated spectra. The Hg peaks are most pronounced in these spectra. Dy mainly stays at the bottom;

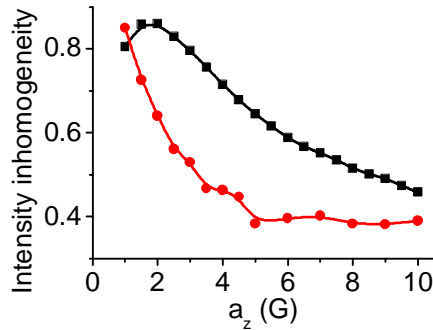


Figure 7.8: Axial intensity inhomogeneity α (equation (7.1)) of Dy 642.19 nm for lamps Q4 and Q5 (wide, short burner), as a function of the gravitational acceleration a_z : ■ lamp Q4 (6 mg Hg), 89.5 W; ● lamp Q5 (12 mg Hg), 89.5 W.

therefore the axially integrated spectra only show small Dy peaks as they appear mainly at the bottom of the lamp.

Axial intensity inhomogeneity

For the DyI₃ lamps, the values for the axial line intensity inhomogeneity α of the Dy-642 peak have been obtained (equation (7.1)) for different gravitational accelerations. The results for the lamps with quartz burner (Q1–Q3) are shown in figure 7.7(a). In all graphs, lines are shown to guide the eye. The values for the axial intensity inhomogeneity α are in agreement with the values for the density inhomogeneity obtained by ILAS in chapter 6 [72] and the results obtained by ALI [38]. This is seen in figure 7.7(b), which shows the values for the square of the axial intensity inhomogeneity (α^2) at 148.4 W for the three lamps Q1–Q3, for emission spectroscopy and ILAS, and the axial segregation λ for ALI. The shapes of the curves for the same lamp are in agreement and the positions of the maximums are found at the same gravitational acceleration. The small difference is explained by the difference in measurement technique: ILAS yields the number density of the ground state Dy atoms, whereas by emission spectroscopy the intensity of radiating Dy atoms (Dy-642) is measured. The intensity is affected by temperature stronger than the absolute number density, due to the temperature dependence of the highly excited states, causing a stronger temperature effect in the axial inhomogeneity parameter. For further explanation on the axial temperature gradient the reader is referred to chapter 5 [73].

The axial intensity inhomogeneity α of the short lamps Q4 and Q5 (containing 6 mg and 12 mg Hg, respectively) are shown in figure 7.8. For lamp Q4 (6 mg Hg) the maximum axial intensity inhomogeneity is around $2g$. Lamp Q5 contains 12 mg Hg and has therefore a higher convection speed ($v \sim p_{\text{Hg}}$) [42, 53, 73], increasing the

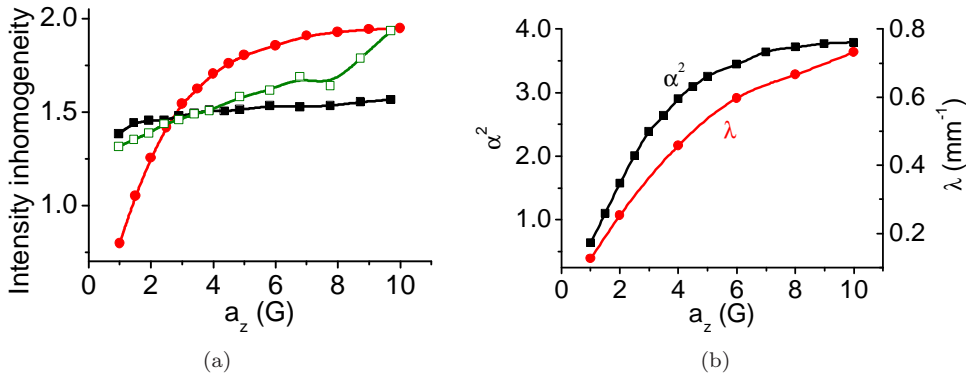


Figure 7.9: (a) Axial intensity inhomogeneity α (equation (7.1)) of Dy 642.19 nm for lamps Q6 and Q7 (thin, long burner), as a function of the gravitational acceleration a_z : ■ lamp Q6 (0.7 mg Hg) 129.9 W (values have been multiplied by 3), □ lamp Q6 101.7 W (values have been multiplied by 3), ● lamp Q7 (2.5 mg Hg) 129.9 W. (b) Square of the axial inhomogeneity (α^2) (equation (7.1)) and the axial segregation λ of Dy 642.19 nm for lamp Q6 (0.7 mg Hg), 129.9 W, as a function of the gravitational acceleration a_z , comparison between emission spectroscopy and ALI. The curve for lamp Q7 shows the same trend and is not shown for clarity [72]. ■ Emission spectroscopy (square of the intensity inhomogeneity; left axis); ● ALI (axial segregation λ ; right axis) [38].

ratio between convection and diffusion speeds. This explains that we are more at the right-hand side of the Fischer curve (figure 7.1) for this lamp Q5.

The values for α for 6 mg Hg are in agreement with the ILAS measurements [72]. Above $5g$, the axial intensity inhomogeneity α is still decreasing for emission spectroscopy, whereas α is only slightly decreasing for ILAS. For 12 mg Hg the values for α are different for emission spectroscopy and ILAS, especially above $5g$. For emission spectroscopy the axial intensity inhomogeneity is constant at $\alpha \approx 0.4$ above $5g$. For ILAS $\alpha \approx 0.4$ for $4g$, and next we observe a jump to a constant level of $\alpha \approx 0.6$ above $4g$. This difference is explained by the larger temperature effect for the 12 mg Hg lamp, compared with the 6 mg Hg lamp.

If we compare the values for α for the lamps Q4 and Q5 (figure 7.8) with those for the lamps Q1–Q3 (figure 7.7(a)), we are more at the right-hand side in the Fischer curve for lamps Q4 and Q5. This is because of the larger ratio between the radius and the height of the burner [73].

Figure 7.9(a) shows the axial intensity inhomogeneity α for the lamps with the long, thin burner Q6 and Q7. These curves show that we are at the left-hand side of the Fischer curve. The ratio between the height and radius of the burner is larger than for lamps Q1–Q5, causing a larger ratio between the convection and diffusion speeds [73]. For lamp Q6 (0.7 mg Hg) we are at the far left-hand side of the Fischer curve. We see

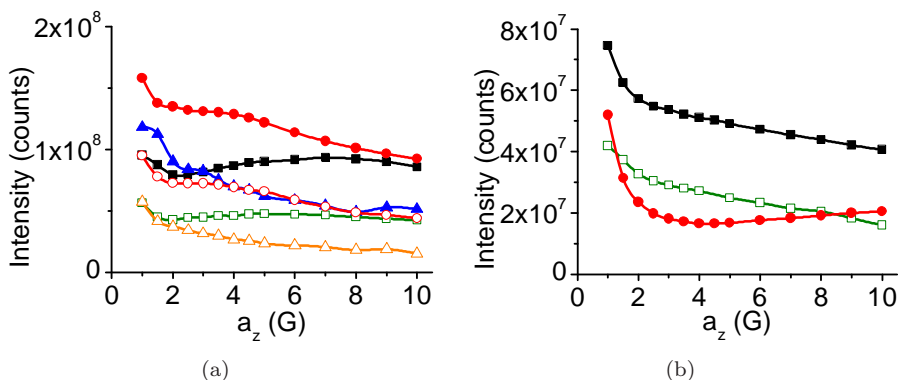


Figure 7.10: (a) Axially integrated intensity of Dy 642.19 nm, as a function of the gravitational acceleration a_z , for lamps Q1–Q3. The lamps show maximum intensity at $1g$ and are therefore optimized for $1g$. Lamp Q1 (5 mg Hg) ■ 148.4 W, □ 129.9 W; lamp Q2 (7.5 mg Hg) ● 148.4 W, ○ 129.9 W; lamp Q3 (10 mg Hg) ▲ 148.4 W, △ 129.9 W. (b) Axially integrated intensity of Dy 642.19 nm, as a function of the gravitational acceleration a_z , for lamps Q6 and Q7 (thin, long burner): ■ lamp Q6 (0.7 mg Hg) 129.9 W, □ lamp Q6 101.7 W, ● lamp Q7 (2.5 mg Hg) 129.9 W.

that the axial intensity inhomogeneity is much lower than for lamp Q7 (2.5 mg Hg) and the inhomogeneity increases with a smaller slope than lamp Q6. The values for the square of the axial intensity inhomogeneity (α^2) are in agreement with the values for the axial segregation λ obtained by ALI [38]. This is seen in figure 7.9(b), which shows these values at 129.9 W for lamp Q6 for emission spectroscopy and ALI.

The trends for the square of the axial intensity inhomogeneity parameter (α^2) for lamps Q1–Q3 and Q6 and Q7 are in agreement with the results obtained for the axial segregation parameter λ measured by ALI by Nimalasuriya *et al* [38].

From the results and the comparison with the results obtained by ILAS for lamps Q1–Q3, we conclude that the emission spectroscopy can be used to characterize MH lamps.

Axially integrated intensity

Figure 7.10(a) shows the axially integrated intensity of the atomic Dy peak at 642.19 nm as a function of the gravitational acceleration, for the quartz lamps Q1–Q3, at two different values for the input power. The maximum intensity is at $1g$, showing that the lamp was optimized for $1g$. The intensity decreases as a function of the gravitational acceleration for lamps Q2 and Q3 (7.5 and 10 mg Hg). For Q1 (5 mg Hg) the intensity first decreases. The minimum in the intensity is found at the maximum of α (figure 7.7(a)). Beyond the minimum, the intensity increases again slightly. For lower Hg

pressure a second maximum in intensity is observed.

The axially integrated intensity of Dy 642.19 nm for lamps Q6 and Q7 is shown in figure 7.10(b). The intensity for the lamps burning at 129.9 W is in the same order of magnitude as the intensity for lamps Q1–Q3 at 129.9 W. Lamps Q6 and Q7 are also optimized for $1g$. The intensity decreases rapidly when increasing the gravitational acceleration. The geometry of the lamp is important; comparing lamps Q1–Q3 with Q6 and Q7 shows different behaviour. A minimum in intensity for lamps Q6 and Q7 is found at higher Hg pressure, whereas for lamps Q1–Q3 the minimum is found at lower Hg pressure.

The comparison between ILAS and emission spectroscopy for the quartz lamps with DyI₃ shows that the intensity inhomogeneity obtained by emission is in agreement with the density inhomogeneity obtained by ILAS. Now the emission spectroscopy setup has been validated, we can also use the emission spectroscopy setup to characterize lamps with a commercial filling, which we could not investigate using ILAS.

7.4.2 Lamps with CosmoWhite filling

The burner of the commercial Philips CosmoWhite lamp (C1) has been fit into a MH reference lamp outer bulb [27], so it fits in the setup. In addition, lamp C2 has been investigated. This lamp has a shorter, wider burner than the CosmoWhite lamp, but contains the same salt mixture.

Spectra

In the spectra of lamp C1 in figures 7.6(c) and (d) we see an increase of the Tl-535 and Hg-546 peaks in comparison to the radiation from Na-589, when the gravitational acceleration is increased from $1g$ to $10g$. This is also observed by eye when looking directly at the lamp, where we see the colour of the lamp changing from orange towards yellow–green. The webcam images of lamp C1 at $1g$ and $10g$ are shown in figures 7.2(b) and (c).

The spectrum of lamp C2 is shown in figure 7.6(e). When this spectrum is compared with the spectrum of C1 (figure 7.6(c)), we see that the peaks are more broadened (especially the Na-589 line), because of the higher Hg pressure. Lamp C2 contains 12.5 mg Hg, whereas C1 contains only 2.5 mg Hg (table 7.1).

NaI density

Figure 7.11 shows spectra around the Na-D lines at 589 nm for lamp C1, for two different axial positions z , at $1g$ and $10g$. According to equation (7.3) we need $\Delta\lambda$ to calculate the NaI density at the wall. This $\Delta\lambda$ is indicated in the spectra. After calculation of these values for every axial position z in the lamp, we obtain a NaI wall density profile as a function of the axial position. Figure 7.12 shows the density profiles

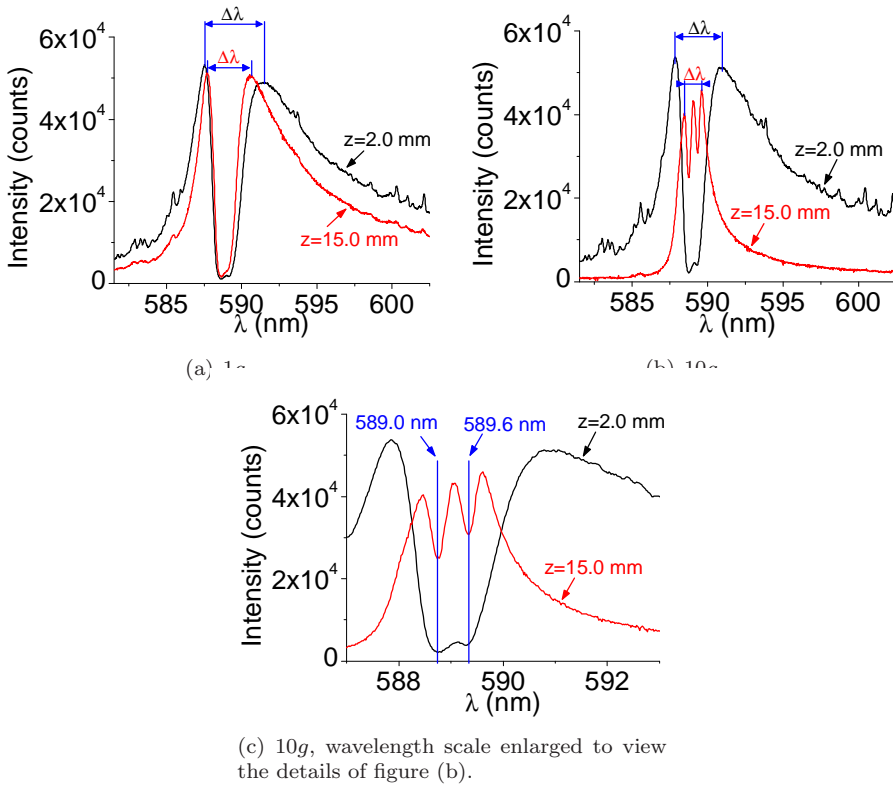


Figure 7.11: Spectra around the Na-D line (589 nm) for lamp C1 (CosmoWhite), 141.6 W, for two axial positions z , at 141.6 W. Closer to the bottom, at $z = 2.0$ mm, $\Delta\lambda$ is larger than at $z = 15.0$ mm, giving a higher NaI density at the wall.

for lamp C1 at 141.6 W, at $1g$, $2g$ and $10g$. From these profiles, we observe that the axial segregation increases when the gravitational acceleration is increased.

Axial intensity inhomogeneity

Figure 7.13 shows the axial intensity profiles for the different emission lines of table 7.2, according to the explanation in section 7.2.3 and figure 7.5. The shape of the Tl curve does not change between $1g$ and $10g$. For the other elements, the shape changes with gravity. The axial density inhomogeneity for the emission lines of different elements (table 7.2) in lamp C1 is shown in figure 7.14(a). The curve for Tl is not shown, because this curve does not change with gravity (figure 7.13). For Hg the inhomogeneity only

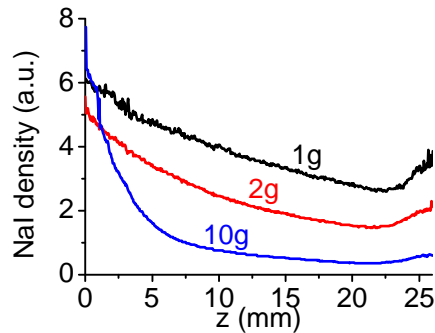


Figure 7.12: NaI density at the wall (equation (7.3)) as a function of the axial position z , for lamp C1 (CosmoWhite), 141.6 W, at $1g$, $2g$ and $10g$.

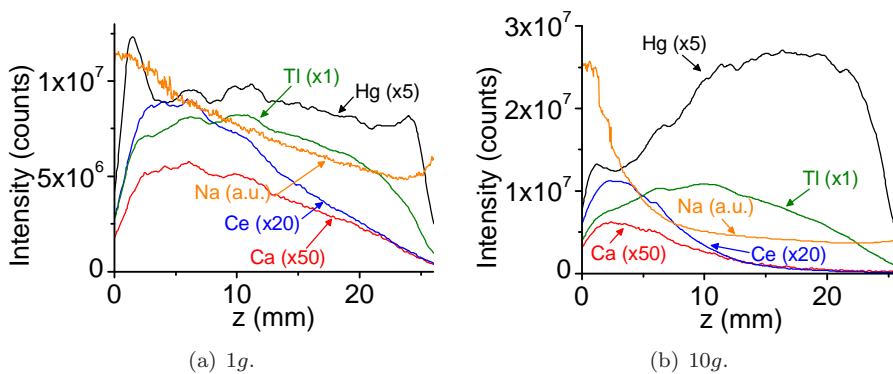


Figure 7.13: Axial profiles of Hg 546.07 nm, Ca 442.67 nm, Ce 556.5 nm and Tl 535.05 nm intensities, and NaI wall density (calculated by delta-lambda method in equation (7.3)) for lamp C1 (CosmoWhite) at 141.6 W. The axial position $z = 0$ mm is at the bottom of the lamp and $z = 26$ mm is at the top. The intensity scale is in counts; the measured number of counts for Hg, Ca and Ce have been multiplied by the factors indicated in the graphs. The NaI density is given in arbitrary units.

slightly increases with gravity. For the other elements (Ca, Ce, Na) the axial intensity inhomogeneity increases with increasing gravity. This means that we are at the left-hand side of the Fischer curve (figure 7.1), with the lowest inhomogeneity at $1g$. This confirms that commercial lamps are optimized for use under $1g$ conditions. The Ca inhomogeneity at 100.7 W shows a wiggle, because of the low intensity of this peak.

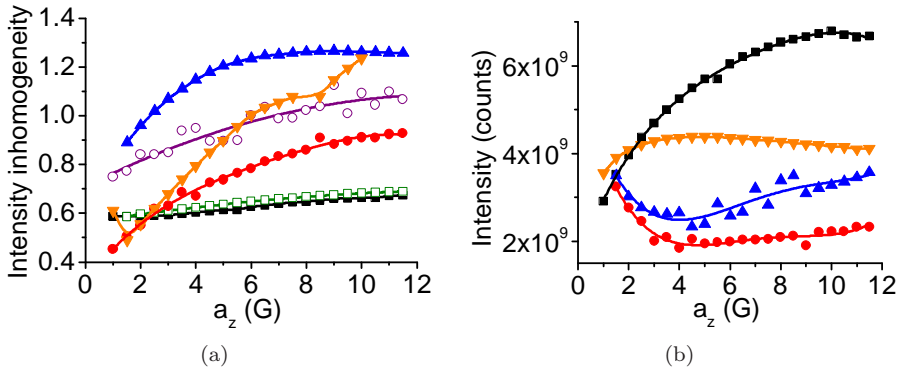


Figure 7.14: (a) Axial intensity inhomogeneity α (equation (7.1)) for different emission peaks for lamp C1 (CosmoWhite), as a function of the gravitational acceleration a_z : ■ Hg 546.07 nm, 141.6 W; □ Hg 546.07 nm, 100.7 W; ● Ca 442.67 nm, 141.6 W; ○ Ca 442.67 nm, 100.7 W; ▲ Ce 556.5 nm, 141.6 W; ▼ Na 589 nm, 141.6 W. (b) Axially integrated intensity for different peaks for lamp C1 (CosmoWhite), 141.6 W, as a function of the gravitational acceleration a_z : ■ Hg 546.07 nm (values have been multiplied by 3); ● Ca 442.67 nm (values have been multiplied by 80); ▲ Ce 556.5 nm (values have been multiplied by 30); ▼ Tl 535.05 nm (original values).

Axially integrated intensity

Figure 7.14(b) shows the peak intensities as a function of the gravitational acceleration for lamp C1, for Hg, Ca, Ce and Tl. The values for the intensity inhomogeneity of the additives of Ca, Ce and Na get larger when increasing the gravity; the additive densities decrease when going from the bottom to the top of the lamp. Towards the top the additives radiate less; this is compensated by increasing the radiation by Hg.

Temperature calculations

The temperature has been calculated for lamp C1, using the 435.83 and 546.07 nm Hg peaks, according to equation (7.4). Figure 7.15(a) shows the axial temperature profiles at 1g, 2g and 10g. The temperature observed in the graph is around 3000 K, which is lower than the ~ 6000 K one would expect for MH lamps [29, 34, 38, 41]. Therefore, the temperature calculation method as described in section 7.3.3 can be used to obtain qualitative temperature profiles only.¹ The curves show an increasing temperature T as a function of increasing axial position z . The steep increase at the first 2 mm is

¹A possible reason for the low temperature is scattering of the light by the PCA burner: not only light from the centre is observed, but also scattered light of other regions of the lamp, giving a lower temperature. A second reason is the limited spectral resolution and experimentally observed line width, which makes it hard to resolve the self-reversed Hg lines.

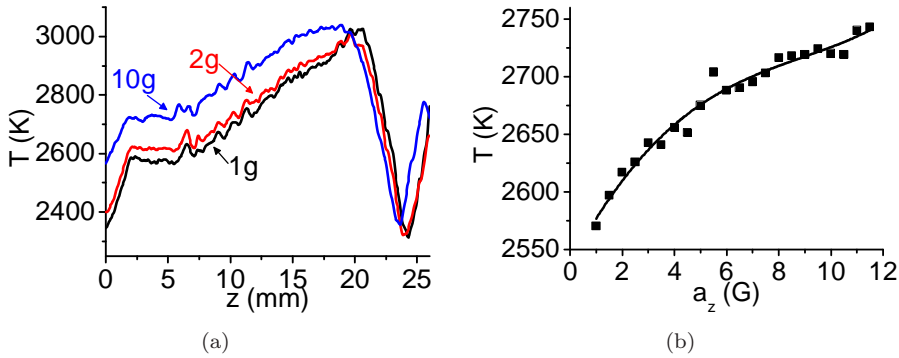


Figure 7.15: Temperature calculated from the Hg peaks at 435.83 and 546.07 nm (equation (7.4)) of lamp C1 (CosmoWhite), 141.6 W. The temperature is lower than the ~ 6000 K one would expect for MH lamps [29, 34, 38, 41]. Therefore, the temperature should be regarded in qualitative terms only.

(a) Temperature profiles for 1g, 2g and 10g, as a function of the axial position z ($z = 0$ mm is at the bottom of the lamp and $z = 26$ mm is at the top);

(b) Temperature at the axial position $z = 5.0$ mm, as a function of the gravitational acceleration a_z .

caused by electrode effects, also the part above 20 mm is influenced by the electrode. Furthermore the temperature curve moves about 1 mm downwards at 10g compared with 1g. This is caused by the lamp burner that is pulled downwards by the large gravitational acceleration.

The temperature for lamp C1 at $z = 5$ mm, as a function of the gravitational acceleration, is shown in figure 7.15(b). The temperature increases with increasing gravitational acceleration. This is explained by the larger axial intensity inhomogeneity of the additives, when increasing the gravitational acceleration. Less additives in the arc means that the radiation comes from the Hg in the lamp, and for radiation by Hg a higher temperature is needed.

The results show a non-uniform axis temperature, which was the reason to introduce the axial intensity inhomogeneity parameter α (sections 7.3.1 and 5.3.3, where the non-uniform axis temperature was obtained by numerical modelling).

7.5 Conclusions

MH lamps have been measured by means of emission spectroscopy. A centrifuge was used to vary the gravity between 1g and 10g. The emission spectroscopy presented in this chapter is an additional method to ILAS and ALI, which are accurate techniques to measure absolute number densities and temperature profiles in the lamps. The

emission spectroscopy method is a fast and easy method to determine the non-uniform axial distribution of radiating particles in the lamp.

We verified the method of emission spectroscopy. We therefore first investigated MH lamps containing Hg and DyI₃ as salt additive. The values for the axial intensity inhomogeneity of Dy are similar to those obtained by ILAS in chapter 6 [72]. ILAS is limited to a fixed salt filling (DyI₃) and geometry. Lamps with a short, wide burner and with a long, thin burner have also been measured. The short, wide lamps show that we are more at the left in the Fischer curve. This is in agreement with the ILAS measurements. For the long, thin lamps, we are at the right-hand side of the Fischer curve, which is in agreement with ALI measurements [38].

From these results obtained for lamps with DyI₃, we conclude that the emission spectroscopy method can be used to characterize MH lamps. This allows us to characterize commercial lamps, such as the Philips MASTER CosmoWhite. We presented the axial inhomogeneity of the different additives (Ca, Ce, Tl, Na). In addition, the NaI density at the wall was derived for these lamps. We also derived the temperature for these lamps. However, the obtained temperature is too low (~ 3000 K) compared with what one would expect (~ 6000 K), so the claim in literature [82] that this method derives the temperature in quantitative terms, is not valid for our lamp and setup. The discrepancy is most probably caused by the limited resolution of our setup. Therefore, we use the obtained values only for qualitative purposes.

For all lamps, the axially integrated intensities were shown. In addition, we showed some spectra of the lamps. The intensity of the additives is the highest at 1g for all lamps. Furthermore, for the CosmoWhite lamp the axial intensity inhomogeneity is the smallest at 1g, showing that this lamp is optimized for use at 1g.

In conclusion, the emission spectroscopy in this chapter is an easy and fast method to investigate MH lamps, including commercial lamps like the Philips MASTER CosmoWhite.

Acknowledgements

The authors are grateful to all participants in the ARGES project for their contributions, especially the General Technical Department of the Eindhoven University of Technology for building the centrifuge, to Philips Advanced Development Lighting, and Senter-Novem (project EDI 03146), SRON [66] and the Dutch Ministries of Research and Education as well as Economic Affairs for funding the research.

Comparison between model and experimental results obtained by imaging laser absorption spectroscopy

Abstract.

The effect of the competition between convection and diffusion on the distribution of metal-halide additives in a high pressure mercury lamp has been examined by placing COST reference lamps with mercury fillings of 5 mg and 10 mg in a centrifuge. By subjecting them to different accelerational conditions the convection speed of the mercury buffer gas is affected. The resulting distribution of the additives, in this case dysprosium iodide, has been studied by numerical simulations and measurements of the density of dysprosium atoms in the ground state using imaging laser absorption spectroscopy. The competition between axial convection and radial diffusion determines the degree of axial segregation of the dysprosium additives.

Sections 8.1–8.8 have been adapted from [M.L. Beks, A.J. Flikweert, T. Nimalasuriya, W.W. Stoffels and J.J.A.M. van der Mullen, *Competition between convection and diffusion in a metal halide lamp, investigated by numerical simulations and imaging laser absorption spectroscopy*, J. Phys. D: Appl. Phys. **41** (2008) 144025].

Section 8.9 has been adapted from [A.J. Flikweert, M.L. Beks, T. Nimalasuriya, G.M.W. Kroesen, J.J.A.M. van der Mullen and W.W. Stoffels, *2-D Images of the Metal-Halide Lamp Obtained by Experiment and Model*, IEEE Trans. on Plasma Science **36** (2008) 1174–1175].

8.1 Introduction

High intensity discharge (HID) lamps are very efficient light sources in widespread use today. They are, amongst others, in use as automotive headlight lamps and to light shops, roads, sports stadiums and large indoor spaces. HID lamps containing a mixture of mercury and metal iodide salts are known as metal-halide (MH) lamps. These devices combine high luminous output with excellent colour rendering. In earlier publications [86, 87] we examined the distribution of additives through numerical modelling. In this publication we will expand the earlier model to allow the simulation of lamps containing metals such as dysprosium. This also allows us to compare the results with experiments [50]. Additionally, we have simulated the lamp under various accelerational conditions to compare with experiments done in a centrifuge (see chapter 4) [37, 38, 51, 52].

One well-known fact [25, 28, 88] is that, when operated vertically, the metal halides in the lamp tend to demix; the concentration of metal halides in the gas phase is much greater at the bottom of the lamp. This effect is not present under all conditions, and some lamp designs are more severely affected than others. The demixing can be observed directly from the light output; a demixed lamp shows a bluish green mercury discharge at the top of the lamp and a much brighter and whiter discharge from the additives at the bottom of the lamp [23]. Demixing, or axial segregation as it is also called, has a negative impact on the efficacy of the lamp. It is currently avoided by using lamp designs with very short or very long aspect ratios. Gaining more insight into the process of demixing could possibly allow a broader range of lamp designs with still better luminous efficacies.

8.2 Demixing

Demixing is caused by a competition between convection and diffusion [28]. Under operating conditions the mercury in the lamp is completely vaporized providing a buffer gas with a pressure of several bar. The additives do not completely vaporize and form a salt pool at the bottom of the lamp. Typical vapour pressures of the additives are in the range of several millibar. The additive molecules diffuse inwards from the wall into the centre of the plasma where they dissociate to form free atoms. These are partially ionized. The atoms diffuse outwards back toward the wall more readily than the molecules diffuse inward. Under (quasi) steady state operation and in the absence of convection the net flux of elements is zero.

Let us assume, for the purpose of this discussion, that the diffusion is given by Fick's law.¹ The flux of species i $\vec{\Gamma}_i$ is then given by

$$\vec{\Gamma}_i = -D_i \nabla p_i, \tag{8.1}$$

¹Note that, in general, the diffusion of species in the plasma does not obey Fick's law and the numerical model does not assume this as discussed in the following section.

with D_i the diffusion coefficient and p_i the partial pressure of species i . In the absence of convection, the flux of atoms towards the walls must equal the flux of molecules away from the walls multiplied with the stoichiometric coefficient. Substitution of this equality into equation (8.1) results in

$$R_{\text{mol,element}} D_{\text{mol}} \nabla p_{\text{mol}} = -D_{\text{atom}} \nabla p_{\text{atom}}, \quad (8.2)$$

with $R_{\text{mol,element}}$ the stoichiometric coefficient. Rearranging the above leads to

$$\nabla p_{\text{atom}} = - \left(\frac{R D_{\text{mol}}}{D_{\text{atom}}} \right) \nabla p_{\text{mol}}. \quad (8.3)$$

Since $D_{\text{atom}} > D_{\text{mol}}$ a larger gradient of the molecular partial pressure can be supported ($\nabla p_{\text{atom}} < \nabla p_{\text{mol}}$). Thus, radial segregation occurs, with more of the additive in the form of molecules near the walls than in the form of atoms in the centre of the discharge. The stoichiometric coefficient is also of importance, however, as each DyI_3 molecule transports three iodine atoms as it diffuses towards the wall. Thus the radial iodine segregation is limited.

The large temperature gradients in the lamp drive natural convection. The convection of the buffer gas drags the additives down along the walls and up again through the centre of the discharge. Because the atoms diffuse outwards more readily than the molecules diffuse inwards the additives stay at the bottom of the discharge. This effect is known as axial segregation.

When the convective and diffusive processes are in the same order of magnitude, the axial segregation of the metal additive is maximal. In the two limiting cases, when there is no convection or when there is extremely high convection no axial segregation is present. In [86] we presented a study that describes this convection-diffusion (CD) competition in full detail. For this we used a model that was constructed by means of the grand model platform PLASIMO [89]. This model gives a self-consistent calculation of the competition between convection, diffusion, the local thermodynamic equilibrium (LTE) chemistry, the electric field and the radiation transport. In [87] we improved the model by taking the shape of the electrode into account. This model with penetrating electrodes was run for a series of mercury pressures and it was found that the electrodes influence convection patterns in the lamp. Both [86] and [87] were based on MH lamps consisting of a mixture of Hg and NaI. To compare with experiments the authors have extended the model to work with dysprosium iodide. Results comparing with experiments under micro-gravity have been examined in [71].

Because the convection is induced by gravity, varying the accelerational conditions aids the understanding of the diffusive and convective processes inside the lamp. A centrifuge, which can go up to $10g$, was built for this purpose (chapter 4) [33, 37, 41, 43, 51, 52]. The MH lamp that is investigated in the centrifuge is a COST lamp [27]. It contains 4 mg DyI_3 as salt additive, which is partially evaporated when the lamp is burning. In the centrifuge setup, the ground state Dy density distribution is measured

by means of imaging laser absorption spectroscopy (ILAS) [37]. These experimental results are compared with the model.

8.3 Model description

We will give a short overview of the basic equations solved in the model. More details are presented in [71, 86, 87]. The model assumes LTE [90].

8.3.1 Energy balance

All modules come together in the energy balance to calculate the plasma temperature. The temperature, in turn, strongly influences the transport coefficients, composition, flow and radiation. The temperature is given by

$$\nabla \cdot (C_p \vec{u} T) - \nabla \cdot (K \nabla T) = P - Q_{rad}, \quad (8.4)$$

where C_p is the heat capacity at constant pressure, \vec{u} the bulk velocity, K the thermal conductivity, Q_{rad} the net radiated power and P the Ohmic dissipation ($P = \sigma E^2$).

The term Q_{rad} is the result of 2D ray-tracing. We solve the equation for the radiation intensity I_ν [91]

$$\frac{dI_\nu}{ds} = j_\nu - \kappa I_\nu, \quad (8.5)$$

with j_ν the local emission coefficient and κ the local coefficient for absorption along rays passing through the discharge [87]. The net radiated power is given by [91]:

$$Q_{rad} = \int_\nu \left(4\pi j_\nu - \int_{4\pi} \kappa I_\nu d\Omega \right) d\nu, \quad (8.6)$$

with ν the frequency. For the precise form of Q_{rad} for a DyI₃-Hg mixture we refer to [91]. To form the boundary conditions the electrodes are assumed to have a surface temperature of 2900 K and the rest of the wall a temperature of 1200 K.

8.3.2 Bulk flow

The bulk flow follows from the Navier-Stokes equation:

$$\nabla \cdot (\rho \vec{u} \vec{u}) = -\nabla p + \nabla \cdot (\mu \nabla \vec{u}) + \rho \vec{a}_g, \quad (8.7)$$

with p the pressure, \vec{a}_g the local (gravitational) acceleration, μ the dynamic viscosity and ρ the density of the plasma.

Particle transport

Since we assume LTE, the particle densities may be described by the local temperature, pressure and elemental composition. A convenient quantity to describe the distribution of elements is the elemental pressure. It is defined as the pressure that contains all molecular, atomic and ionic contributions of a particular element. The elemental pressure p_α for the element α can be written as

$$p_\alpha = \sum_i R_{i\alpha} p_i, \quad (8.8)$$

with p_i the partial pressure of the species i , and $R_{i\alpha}$ the stoichiometric coefficient [86]. We solve a conservation equation for the elemental pressure

$$\nabla \cdot \left(\frac{D_\alpha}{kT} \nabla p_\alpha + \frac{p_\alpha}{kT} \vec{c}_\alpha \right) = 0, \quad (8.9)$$

with an effective diffusion coefficient D_α [86]

$$D_\alpha = p_\alpha^{-1} \sum_i R_{i\alpha} D_i p_i \quad (8.10)$$

and a pseudo convective velocity c_α [86].

To fix the boundary conditions we assume the existence of a cold spot at the bottom corner of the lamp, where the elemental pressure is derived from the x-ray induced fluorescence measurements at 1g of the elemental density of Dy and I at the cold spot [50]. Everywhere else the flux through the wall is zero.

Direct measurements of the elemental pressure at the walls are not possible for the lamps in the centrifuge, therefore we assume a Dy elemental pressure at the wall of 517 Pa and an I elemental pressure of 4268 Pa. These vapour pressures were determined with x-ray induced fluorescence measurements at 1g [50]. These are assumed to give a good estimation of the vapour pressure at the walls and are used to fix the boundary conditions. Note that there is an excess of iodine in the cold spot. This excess occurs because dysprosium is absorbed by the walls of the lamp.

Ohmic heating

The power to the plasma is supplied by Ohmic heating. We solve the Poisson equation in the form

$$\nabla \cdot (\sigma_{el} \nabla \Phi) = 0, \quad (8.11)$$

with Φ the potential. From the potential Φ we can derive the electric field $\vec{E} = -\nabla \Phi$ and the current density $\vec{J} = \sigma_{el} \vec{E} = -\sigma_{el} \nabla \Phi$. The following boundary conditions are employed:

1. There is no current through the walls, resulting in a homogeneous Neumann boundary condition ($(\partial\Phi/\partial n) = 0$).
2. One electrode is kept at zero potential, which leads to a Dirichlet condition $\Phi = 0$ at that electrode.
3. The potential of the other electrode is initially set at 100 V. This value is adjusted during the iteration process and determined by the fact that the power dissipated in the discharge equals 135 W. This is equivalent to the actual lamp power of 150 W of which 15 W is consumed by electrode losses and 135 W by ohmic dissipation of the discharge.

The selection of cross-sections

In the basic equations, summarized in the previous section, important roles are played by various transport coefficients, such as the diffusion coefficients D_i , the thermal conductivity K and the electrical conductivity σ_{el} . These transport properties are calculated from collision integrals that are based on differential cross-sections [92]. More information on the cross-sections used can be found in [71].

8.4 Competition between convection and diffusion

The competition between convection and diffusion drives axial segregation in the lamps. For a quantitative description we use the Peclet number, well known from the field of fluid dynamics [93, page 85] which describes the competition between convection and diffusion in a dimensionless number. In this chapter we define the Peclet number as the ratio of the typical axial convection and radial diffusion rates. In terms of the typical axial convection velocity V_z , the height of the lamp burner H , the radius of the burner R and the effective elemental diffusion coefficient introduced earlier the Peclet number is defined as

$$Pe = \frac{R^2 V_z}{H D_\alpha}. \quad (8.12)$$

A high Peclet number ($Pe \gg 1$) corresponds to the situation where the additive does not have time to diffuse radially outwards towards the walls when transported up with the hot mercury atoms in the centre of the lamp. In this case axial segregation cannot occur. For low Peclet numbers ($Pe \ll 1$) the rate of diffusion towards the walls is much greater than the rate of convection, and axial segregation is also absent. Axial segregation is most pronounced at intermediate values ($Pe \approx 1$), as will be shown in the results.

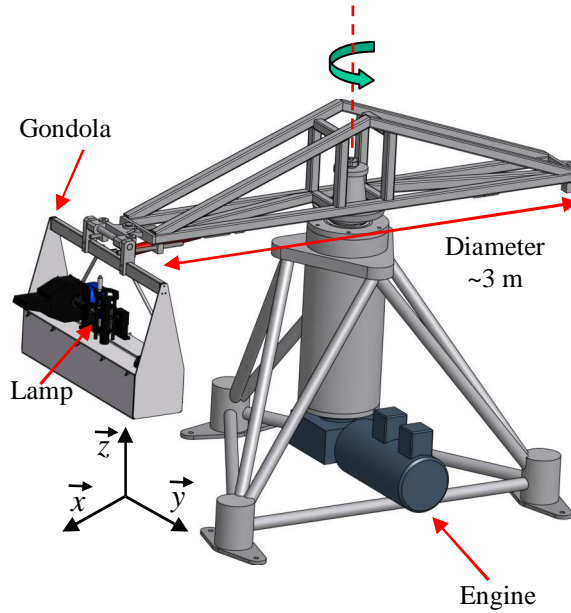


Figure 8.1: Schematic representation of the centrifuge. The coordinate system shown is that of the lamp in the gondola; this is a co-moving system such that \vec{z} is always parallel to the lamp axis [37].

8.5 Experiment

A centrifuge was built as a tool to investigate MH lamps [27] under hyper-gravity conditions up to $10g$ and vary the convection speed in this way. In the following section the results will be compared with the results from the model.

8.5.1 Measurement technique

The experiment has been described in chapter 4 [37]; a summary will be given for clarity. The centrifuge shown in figure 8.1 consists of a pivot, an arm connected to the pivot and at the end of the arm a gondola that contains the lamp and diagnostic equipment. The total diameter at maximum swing-out of the gondola is close to 3 m. The total acceleration vector is always parallel to the lamp axis.

The measurement technique that is used in the centrifuge is ILAS. By using this technique, the 2D density distribution of the ground state Dy atom can be obtained. The principle is as follows. A laser beam is expanded so that it illuminates the full lamp burner. When the lamp is switched on, part of the laser light is absorbed by

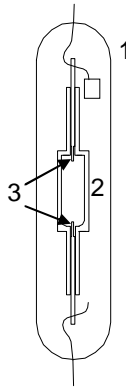


Figure 8.2: Schematic picture of the lamp, (1) outer bulb; (2) burner with height 20 mm and diameter 8 mm; (3) electrodes, distance between both electrodes ~ 18 mm [27].

Dy atoms in the ground state. Behind the lamp, the light that is transmitted by the lamp burner is detected. By comparing the detected laser intensity with and without absorption, the line-of-sight ground state atomic dysprosium density is obtained for each position in the lamp burner.

8.5.2 The lamp

The investigated lamps are COST reference lamps (section 1.3.1) [27], see figure 8.2. The lamps are 20 mm in height (18 mm electrode distance) and 8 mm in diameter. They contain either 5 or 10 mg Hg. Furthermore they contain 4 mg DyI_3 as salt additive and 300 mbar Ar/Kr⁸⁵ as a starting gas. The input power is 148 W; the acceleration a_z is varied from $1g$ to $10g$.

8.6 Results

The model was run for a set power P_S of 135 W and compared with experimental results using a 148 W ballast. The difference of 13 W is an estimation of the electrode losses which are not accounted for in the model. Experiments were done with lamp fillings of 5 and 10 mg Hg. The model was run with lamp fillings ranging from 3 to 20 mg Hg. To fix the boundary conditions for the elemental pressure we assume the existence of a cold spot at the bottom corner of the lamp, where the elemental pressure is derived from the x-ray induced fluorescence measurements at $1g$ of the elemental density of Dy and I at the cold spot [50]. Everywhere else the flux through the wall is zero.

Direct measurements of the elemental pressure at the walls are not possible for the lamps in the centrifuge, therefore we assume a Dy elemental pressure at the wall of 517 Pa and an I elemental pressure of 4268 Pa. These vapour pressures were determined with x-ray induced fluorescence measurements at $1g$ [50]. These are assumed to give a good estimation of the vapour pressure at the walls and are used to fix the boundary conditions. Note that there is an excess of iodine in the cold spot. This excess occurs because dysprosium is absorbed by the walls of the lamp.

The density of dysprosium atoms was measured with the ILAS technique described in the previous section. The lamp underwent centripetal acceleration in the centrifuge from $1g$ to $10g$. The measurement technique yields the column density of dysprosium atoms in the ground state along the line of sight. The model yields many more results, of which only a minor part can be directly correlated with the experiment. We present some of the model results separately for further insight into the mechanisms behind what is observed experimentally.

The model solves differential equations for the total pressure, the velocity, the temperature, the electric potential and the elemental pressures. From these a number of derived quantities are obtained, notably the species densities and the radiation intensity. We will first present the elemental pressures at different lamp pressures and under different accelerational conditions.

8.6.1 Elemental pressure

The elemental dysprosium pressure at $1g$ and $2g$ with 10 mg of mercury given in figure 8.3(a) clearly shows both axial and radial segregation. The amount of dysprosium in the top of the lamp increases with increasing centripetal acceleration.

When one examines figure 8.3(a) carefully, local minima and maxima can be seen in the elemental dysprosium pressure. These are shown more clearly in the profiles for a total mercury content of 5 mg shown in figure 8.4. These local minima and maxima are not present if convection is switched off in the model, as is shown in figure 8.5. For more results comparing this model with micro-gravity experiments we refer to [71]. In figure 8.6 the axial convection speed is plotted. The axial speed is greater in the centre of the lamp than at the edges, due to the lower density and the smaller cross-sectional area in the centre. Consequently, the elemental dysprosium concentration in the centre rises as the acceleration increases. The radial position where the axial velocity crosses through zero does not show the same increase in elemental dysprosium. The result is that with the increase in convection more dysprosium enters the discharge and that the step like radial profile is disturbed.

8.6.2 Atomic dysprosium density

The experiment measures the column density of dysprosium atoms in the ground state. The model calculates the dysprosium atom density from the elemental pressure, total

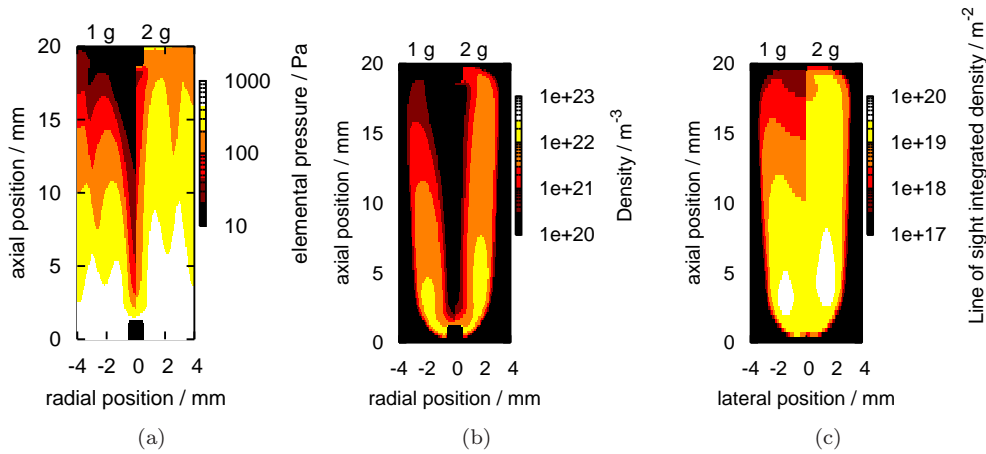


Figure 8.3: (a) Simulated elemental dysprosium pressure for a lamp with a 10 mg mercury filling at $1g$ (left) and $2g$ (right). (b) Simulated atomic dysprosium density for a lamp containing 10 mg of mercury at $1g$ and $2g$ simulated accelerational conditions. The $1g$ result is shown mirrored (negative radial positions) and the $2g$ result is shown on the right half of the graph. (c) Simulated column densities of dysprosium atoms for a lamp containing 10 mg of mercury at $1g$ and $2g$ simulated accelerational conditions. As in the previous graphs, the $1g$ results are shown mirrored with negative lateral positions.

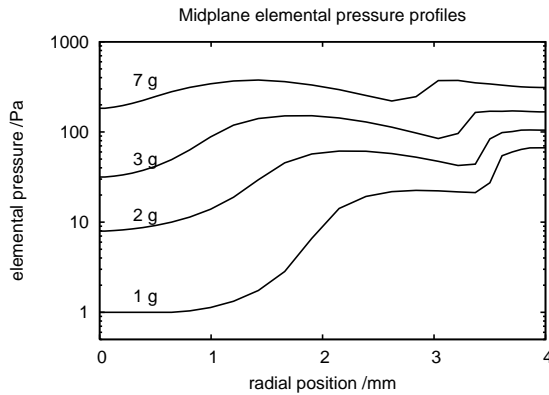


Figure 8.4: Simulated midplane elemental dysprosium pressure profiles for accelerational conditions ranging from $1g$ to $7g$ for a lamp with 5 mg of mercury filling. At low convection speeds the radial profiles have a shape comparable with the micro-gravity situation.

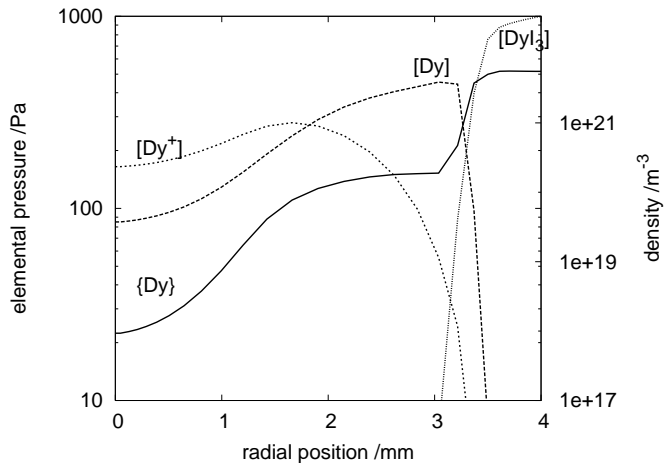


Figure 8.5: Simulated elemental dysprosium pressure (Dy in the figure) with convection switched off (corresponding to micro-gravity). The discharge shows no axial segregation in this case. For comparison, the densities of the dysprosium ions, atoms and DyI_3 molecules are plotted (denoted with square brackets).

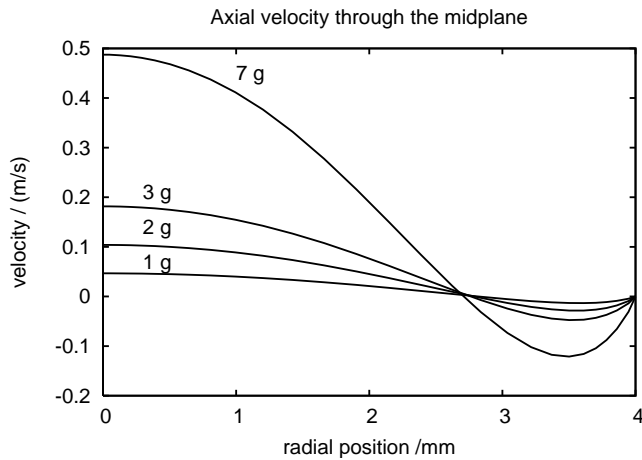


Figure 8.6: Simulated axial velocity through the midplane for accelerational conditions ranging from $1g$ to $7g$ in a lamp with 5 mg of mercury filling.

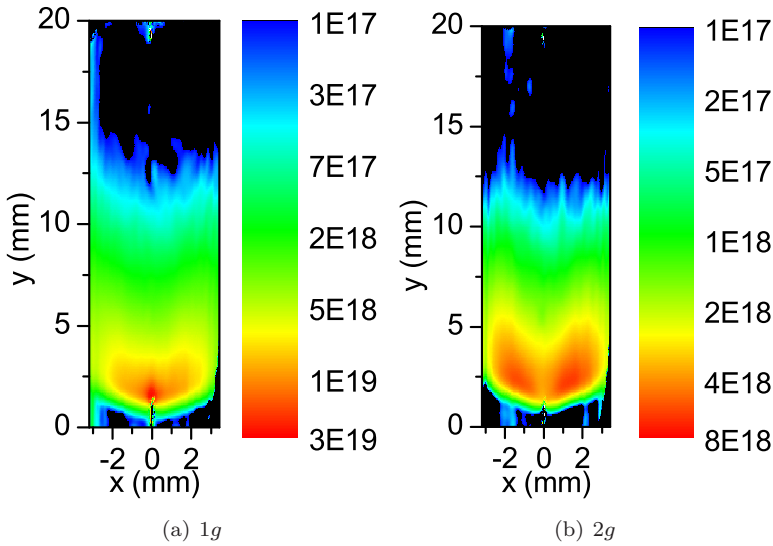
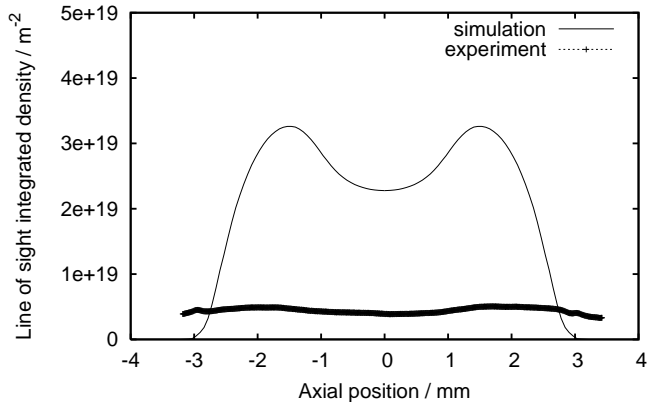


Figure 8.7: Experimental results for the ground state column densities of dysprosium atoms at (a) $1g$ and (b) $2g$ for a lamp containing 10 mg of mercury. Note that negative and positive lateral positions correspond to the left and the right side of the lamp, respectively.

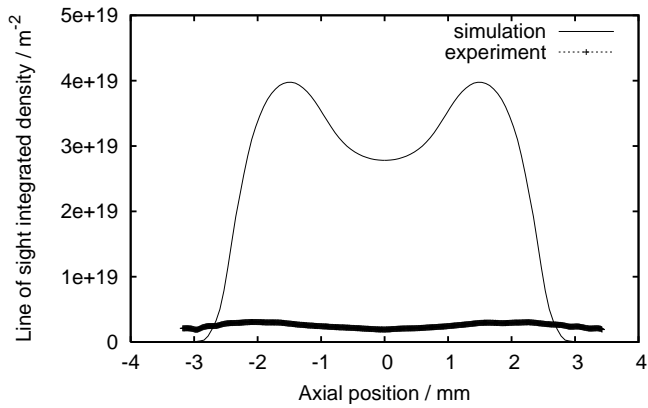
pressure and temperature. An example of the calculated dysprosium density is shown in figure 8.3(b). As is evident in this figure, the dysprosium atom density decreases towards the top of the lamp. Increasing the convection speed by increasing the acceleration causes better mixing.

To compare with the experiments column densities have been calculated. These are shown in figure 8.3(c). For comparison, figure 8.7 shows the measured column densities of dysprosium atoms in the ground state. A qualitative comparison of these graphs shows a number of features present in both model and experiment. Most notable are the heart-shaped regions near the bottom of the lamp, where the dysprosium atoms are concentrated. Under higher accelerational conditions these regions move up slightly and become more elongated; this feature is present in both the model and the experiment.

For a more quantitative comparison, cross-sections of the results from both the model and the experiment at an axial position of 5 mm from the bottom of the lamp are shown in figure 8.8. As before, the results are for a lamp containing 10 mg of mercury under $1g$ and $2g$ acceleration in the centrifuge. The position of the maximum atom density in the simulations corresponds well to the maximum absorption in the experiment. The absolute values, however, do not agree. Figure 8.9 compares the measured atomic ground state density with the simulated atomic densities along the



(a) 1g



(b) 2g

Figure 8.8: Experimental results for the ground state column densities of dysprosium atoms at (a) 1g and (b) 2g for a lamp containing 10 mg of mercury compared with the simulations. Results shown are at an axial position of 5 mm from the bottom of the lamp.

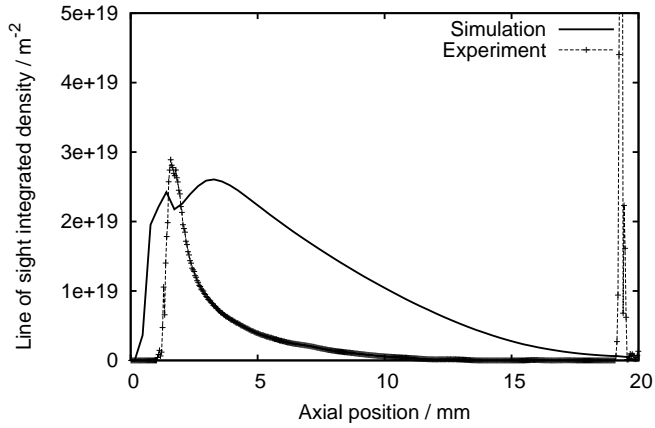
axis, and 2 mm off-axis. These results show good qualitative agreement between the simulation and the experiment. In particular, the position of the maximum density shows good agreement. The densities in the simulation are generally much larger. A possible reason might be the assumed cold spot vapour pressure. The cold spot vapour pressure depends exponentially on the temperature, as shown in figure 8.10. During the lifetime of the lamp, however, dysprosium migrates into the quartz walls. The individual lamps also differ. A change in the temperature of just 10 K leads to a 30 % increase in the vapour pressure just above the cold spot.

8.7 Cold spot vapour pressure

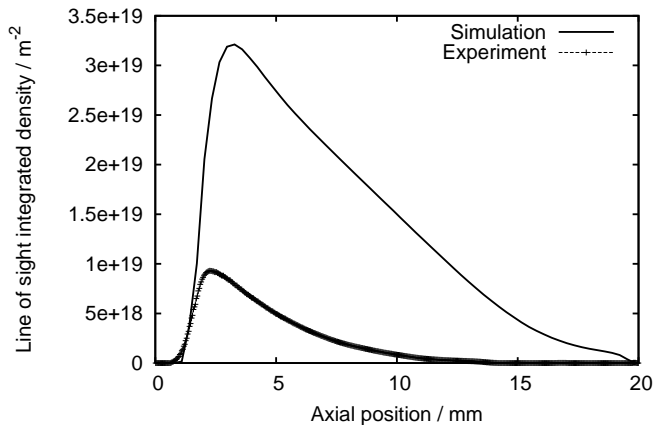
To further investigate the dependence on the cold spot vapour pressure, the model was rerun with dysprosium vapour pressures of 100–400 Pa in steps of 50 Pa. This study revealed that a dysprosium vapour pressure of 150 Pa, corresponding with a temperature of 1100 K, gave the closest match with experimental results. Figure 8.11 shows the ground state line-of-sight integrated densities of the dysprosium atoms at 5 mm from the bottom electrode for vapour pressures between 100 and 250 Pa compared with experimental results. The results with the 150 Pa vapour pressure also match well at other distances from the electrodes, as shown in figure 8.12, which compares lateral ground state densities as predicted by the model with a cold spot vapour pressure of 150 Pa with experiments along a line 2 mm off-axis. A line 2 mm off-axis is chosen as it offers the largest signal, and hence the best signal-to-noise ratio.

Varying the cold spot vapour pressure also allows us to study the effect of the radiation emitted by the additive. In the limit that the cold spot vapour pressure of dysprosium approaches zero the lamp becomes a pure mercury lamp again. Figure 8.13 shows the resulting temperature profiles in the midplane between the electrodes. From this figure it becomes evident that increasing the dysprosium elemental vapour pressure increases the contraction of the arc. This finding is in line with earlier findings and is due to the radiation emitted by dysprosium. By adding more dysprosium to the discharge radiative cooling is increased. The greatest concentration of emitting species is found just off-centre. The radiation emitted by dysprosium is optically open and not reabsorbed near the walls. Thus the radiation cools down the plasma on the flanks. To still allow sufficient current to pass through the plasma the centre has to become hotter. Hence, the observed contraction of the arc.

The hotter centre also results in increased convection, as is shown in figure 8.14. This is simply due to the larger temperature difference. The larger temperature difference translates directly into larger density gradients, which drive the convective flow.



(a) Along the axis



(b) 2 mm off-axis

Figure 8.9: Experimental results for the ground state column densities of dysprosium atoms at $1g$ for a lamp containing 10 mg of mercury compared with the simulations. Results shown are (a) along the axis and (b) 2 mm off-axis.

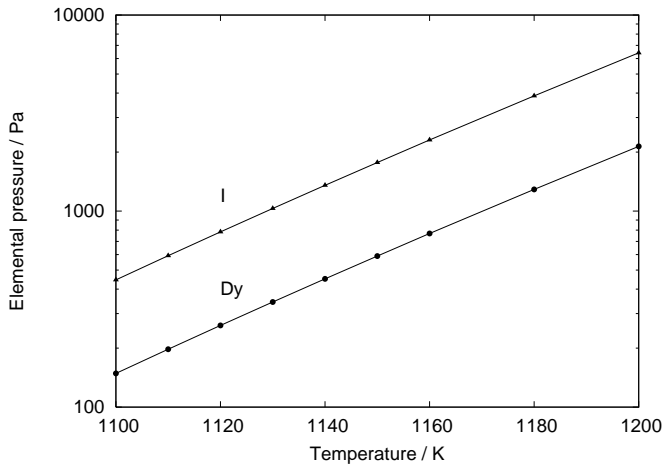


Figure 8.10: Elemental vapour pressure of dysprosium and iodide, as calculated by Gibbs minimization for temperatures between 1100 K and 1200 K.

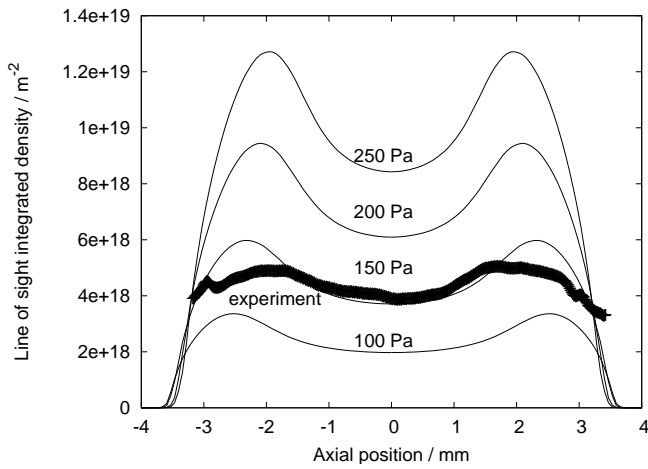


Figure 8.11: Experimental results for the ground state column densities of dysprosium atoms at 1g for a lamp containing 10 mg of mercury compared with the simulations at vapour pressures from 100 to 250 Pa. Results shown are at an axial position of 5 mm from the bottom of the lamp.

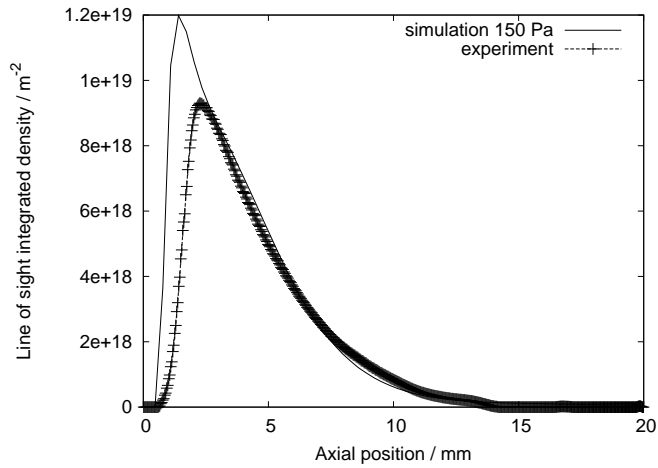


Figure 8.12: Experimental results for the ground state column densities of dysprosium atoms at $1g$ for a lamp containing 10 mg of mercury compared with the simulations at a vapour pressure of 150 Pa.

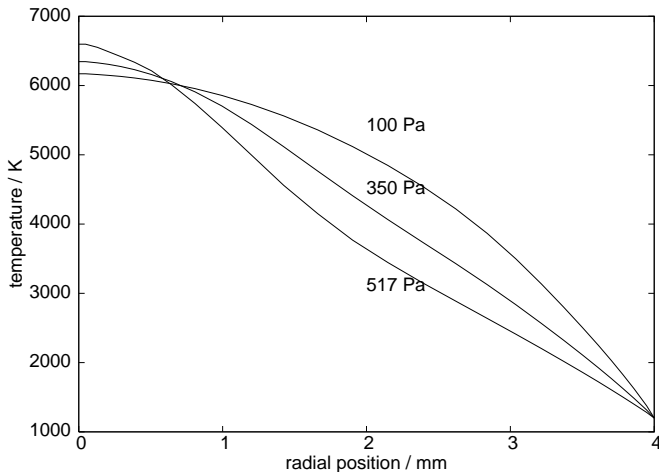


Figure 8.13: Midplane temperature profiles for three different cold spot vapour pressures: 517, 350 and 150 Pa. Adding more dysprosium clearly increases the contraction of the arc.

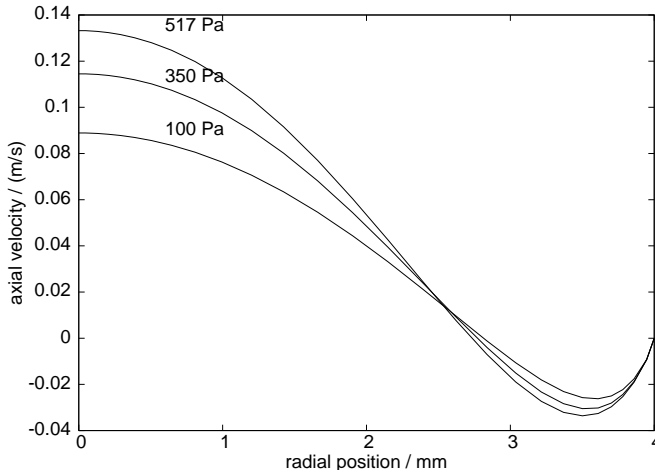


Figure 8.14: Midplane axial velocity profiles for three different cold spot vapour pressures: 517, 350 and 150 Pa. Adding more dysprosium increases the contraction of the arc and thereby increases the axial velocity through the midplane.

8.7.1 Demixing

We studied the demixing by defining the average segregation depth τ_α of element α as

$$\tau = \frac{1}{V} \int_V \tau_H dV, \quad (8.13)$$

with τ_H given by

$$\tau_H = \frac{H}{p_\alpha} \left(\frac{\partial p_\alpha}{\partial z} \right). \quad (8.14)$$

If τ is much smaller than unity the element is homogeneously distributed. Axial demixing occurs if τ is greater than unity.

To compare results with different lamp fillings we examine the segregation as a function of the Peclet number as defined in equation (8.12) (figure 8.15). We use the velocity on the axis halfway between the electrodes. The elemental diffusion coefficient is taken from the same spot. The model was run with a number of different pressures and simulated accelerational conditions. If we plot τ as a function of Peclet number a single curve emerges along which all results lie. The maximum point on this curve lies at $Pe = 1$.

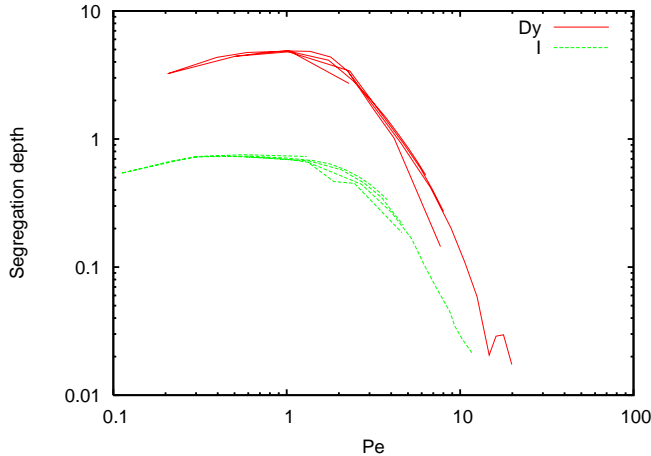


Figure 8.15: Segregation depth as a function of the Peclet number as defined by equation (8.12) obtained from the model. Lamp fillings between 3 and 20 mg and accelerational conditions between $1g$ and $10g$ are shown. Each lamp filling leads to a line in the figure. Note that τ has a maximum at $Pe = 1$. Iodine shows much less demixing than dysprosium.

8.8 Conclusions

A MH lamp with the COST geometry has been placed in a centrifuge to study the effect of the competition between convection and diffusion on the distribution of additives in the lamp. Using the plasma modelling platform PLASIMO, we have simulated the same lamp under different accelerational conditions. The density of dysprosium atoms in the ground state has been measured using the ILAS technique for different lamp fillings and accelerational conditions. These ground state densities show good qualitative agreement with the dysprosium atom densities predicted by the model.

The quantitative agreement between the model and experiments is not so good. One possible reason is the cold spot vapour pressure of the elements. This cold spot vapour pressure depends exponentially on the cold spot temperature. Increasing the temperature by 10 K is enough to raise the vapour pressure by 30%. Using a vapour pressure of 150 Pa rather than the value of 517 Pa measured by x-ray fluorescence (XRF) by Nimalasuriya *et al* [50] on similar lamps yields a better quantitative match between model and experiment.

The study with different vapour pressures also gives insight into the effects of the radiation emitted by the dysprosium additives. Increasing the partial pressure of dysprosium atoms and ions increases the radiation emitted by these species. Most of this radiation is emitted just off-centre from the axis. The radiative cooling by dyspro-

sium causes the arc to contract. Increasing the amount of dysprosium in the discharge increases arc contraction.

The competition between convection and diffusion can be understood quantitatively by introducing a Peclet number defined as the ratio between the rate of radial diffusion and axial convection. A Peclet number of unity leads to the greatest axial segregation. Increasing the convection speed by increasing the acceleration changes the radial profiles from a step-like profile to a more erratic profile with local minima and maxima. Obtaining a homogeneous distribution of additives in the lamp can be achieved by designing a lamp such that the Peclet number is much greater or much smaller than unity.

Acknowledgements

The authors are grateful to Senter-Novem (project EDI 03146), SRON [66], the Dutch Ministries of Research and Education and Economic Affairs as well the Technology Foundation STW, Applied Science Division of NWO for funding the research. We also wish to thank A.F. Meunier and G.M. Thubé (École polytechnique de l'université d'Orléans, France) for their contributions to the experimental results.

8.9 2D images of the metal-halide lamp obtained by experiment and model

Abstract.

The metal-halide lamp shows colour segregation caused by diffusion and convection. Two-dimensional imaging of the arc discharge under varying gravity conditions aids in the understanding of the flow phenomena. We show results obtained by experiments and by numerical simulations in PLASIMO.

The metal-halide (MH) lamp is a compact high-intensity light source with a high luminous efficacy and a good colour rendering index [3]. The arc discharge lamp contains a buffer gas (Hg) and metal additives (for instance Na, Ce, Dy) dosed as metal-halide salts. These metal additives improve the colour rendering. The additive density distribution is determined by convective and diffusive processes (due to the high radial temperature gradient). When these processes are in the same order of magnitude, the competition between them leads to axial segregation of the metal additive, then segregation of colours appears (figure 8.16(a)) [27, 28, 32, 33, 38]. Because the convection is induced by gravity, a centrifuge that can go up to $10g$ was built to vary the amount of convection (chapter 4) [37].

We can look at the plasma of the MH lamp in different ways. Two-dimensional imaging of the plasma in the MH lamp gives insight into the flow phenomena and hence the segregation inside the lamp. Here, we investigate one particular MH lamp at different gravity conditions and present colour pictures taken by an ordinary webcam and 2D metal additive density profiles measured by Imaging Laser Absorption Spectroscopy (ILAS; section 4.3.2) [37]. Besides these experimental results we show several images representing physical quantities in the lamp, obtained by numerical simulations in PLASIMO [70, 86].

The MH lamp is a COST reference lamp (section 1.3.1) [27] and contains 10 mg Hg as buffer gas, 300 mbar Ar/Kr⁸⁵ as starting gas and 4 mg DyI₃ as salt additive. The diameter of the lamp burner is 8 mm and the burner height is 20 mm (electrode distance 16 mm). The input power is 148.4 W.

Figure 8.16 shows a picture of the lamp taken by a digital camera and webcam images taken from $1g$ to $10g$. The directly visible colour segregation is clearly seen at $1g$. The bluish-white light at the bottom originates from Dy atoms. Towards the top the colour is bluish-greenish, which is due to Hg atoms. At higher gravity one sees that the axial colour segregation is diminished: the Dy atoms are more evenly distributed over the lamp, caused by the increased amount of convection.

The line-of-sight ground state atomic Dy density is obtained by ILAS. With ILAS, a laser beam is expanded so that it illuminates the whole lamp burner. A part of the laser light is absorbed by the Dy atoms. After passing the lamp burner the remaining laser light hits a CCD camera. From this remaining intensity, the absorption and hence the

density is calculated at each position in the lamp burner; this gives an indirect image as nonradiative particles are measured. In figure 8.17, the same effect is seen as at the webcam images. At normal gravity ($1g$), the Dy atoms stay mainly at the bottom of the plasma; the maximum is found somewhere between the centre and the wall of the plasma. When gravity is increased, the maximum of the atomic Dy density moves upward and at the same time the Dy atoms are more evenly distributed over the lamp.

In addition to the direct and indirect images of the plasma obtained by experiments, the lamp has been studied by numerical simulations in PLASIMO [70, 86]. This model assumes local thermodynamical equilibrium. The temperature is calculated from the energy balance, whereas the bulk flow follows from the Navier Stokes equation. Figure 8.18 shows the ground state atomic Dy density, the temperature distribution, the axial convection speed and the electron density; all at $1g$ and $2g$. The Dy densities are line-of-sight integrated densities (lateral position on horizontal axis), whereas the other images are radial densities (radial position on horizontal axis). When one compares figure 8.18(a) and (b) with the experimental results in figure 8.17(a) and (b), the same trend is observed: the shape of the Dy density is in agreement and it is seen that at higher gravity the Dy atoms are more evenly distributed over the lamp. Figures 8.18(c) and (d) show the strong radial gradient in temperature. The axial convection speed is shown in figure 8.18(e) and (f); positive values correspond to an upward flow whereas negative values correspond to a downward flow. The convection speed increases linearly with gravity; the figures show that the convection speed at $2g$ is twice as high as at $1g$. Finally figure 8.18(g) and (h) show the electron density distribution over the lamp burner.

In conclusion, the MH lamp can be investigated by different methods, which gives 2D images of the plasma in different ways. The colour segregation that is observed at the webcam images at different gravity is directly correlated to the Dy density images obtained by ILAS. Modelling of the same lamp also offers Dy density images, which are in agreement with the experimental results, and other physical quantities.

The authors are grateful to A.F. Meunier and G.M. Thubé, Philips ADL, Senter-Novem (project EDI 03146), SRON and the Dutch Ministries of Research and Education as well as Economic Affairs for funding the research.

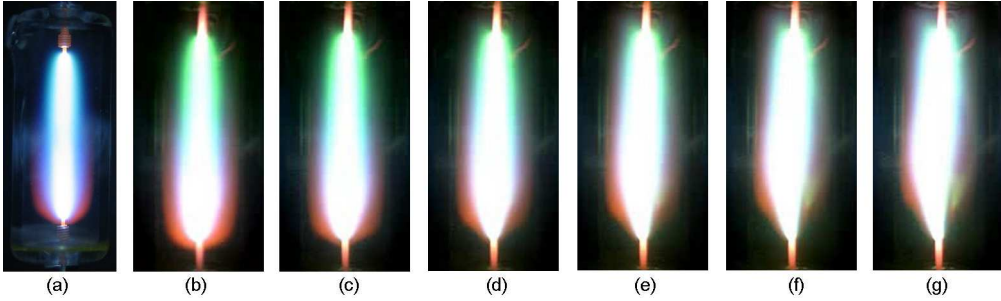


Figure 8.16: (a) Picture of the lamp at 1g; (b)–(g) webcam images at 1g, 2g, 4g, 6g, 8g, 10g.

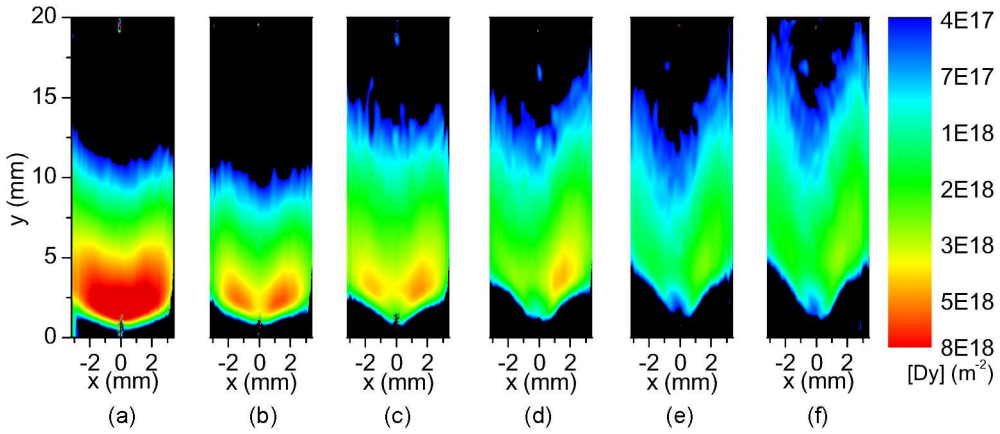


Figure 8.17: Imaging Laser Absorption Spectroscopy (ILAS) images at 1g, 2g, 4g, 6g, 8g, 10g.

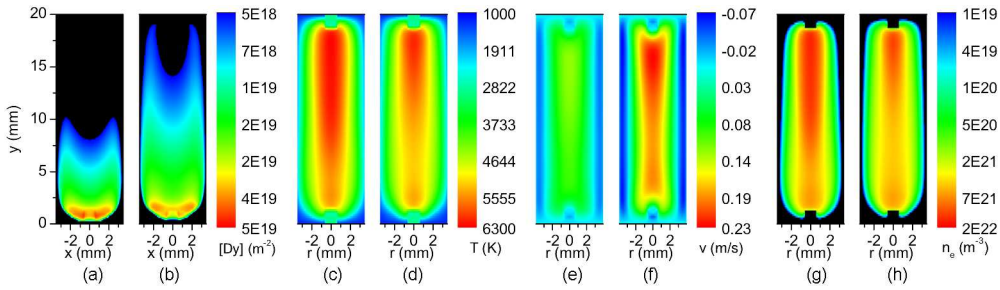


Figure 8.18: Simulations (PLASIMO) at 1g and 2g: (a)–(b) ground state Dy density; (c)–(d) temperature; (e)–(f) axial convection speed; (g)–(h) electron density.

Conclusions

9.1 Introduction

The aim of this thesis is to characterize a well verifiable metal-halide (MH) lamp and obtain a set of reliable measurement data. The experimentally obtained data is used to verify existing numerical models of the MH lamp, which gain a better understanding of the plasma properties and transport phenomena in the metal-halide (MH) lamp. Axial segregation of the additive is caused by the combination of the convective and diffusive phenomena in the lamp. Convection is induced by gravity, hence the measurements under varying gravity conditions: laboratory measurements ($1g$), measurements during parabolic flights ($0-2g$) and measurements in the centrifuge ($0-10g$).

To develop better lamps, the knowledge from the gravitational study can be applied to other parameters that influence the amount of convection. Examples in practice are changing the buffer gas pressure or the ratio between the length and radius of a lamp.

The experiments are used to verify the results obtained by modelling. The model gives insight and aids in the interpretation of the experimental results. In this chapter, an overview of the conclusions of the different chapters is given. Finally a general outlook is given.

9.2 Laser absorption spectroscopy (1D) at $1g$ and $0-2g$

9.2.1 Laboratory measurements at $1g$

The 1D laser absorption spectroscopy technique yields the laterally resolved absolute number density of ground state atomic dysprosium in the metal-halide lamp. These measurements were performed for different axial positions in the MH lamp; a 2D ground state atomic dysprosium density profile was obtained.

The MH lamp with 10 mg Hg and 4 mg DyI₃ showed a hollow density profile of atomic Dy. We observed strong axial segregation, caused by diffusion and convection. The radially averaged Dy density as a function of axial position followed the exponential decay predicted by E. Fischer, except for the regions close to the electrodes. The results show that this lamp is on the right-hand side of the Fischer curve.

9.2.2 Parabolic flights

Convection is induced by gravity, and by changing gravity we could verify the Fischer curve. During the parabolic flights, parabolas were performed with $0g$ and $2g$ phases of about 20 s each. The radially averaged atomic dysprosium density, measured by means of 1D laser absorption spectroscopy, follows the qualitative description presented by Fischer. The measured lamp voltage is a measure for the total amount of dysprosium in the lamp. The integrated light emission decreased when the axial segregation increased. This is in agreement with the Dy density and the lamp voltage measurements.

Three processes with different time constants played a role when switching from hyper-gravity to micro-gravity. The axial diffusion time constant is the slowest time constant (~ 30 s), which is proportional to the amount of mercury. As a result, at the end of the micro-gravity phase the lamp was still not in equilibrium.

9.3 Imaging Laser Absorption Spectroscopy (2D) at 1–10 g

9.3.1 Development of the centrifuge and ILAS

A centrifuge was built to extend the measurements to even higher gravity levels: 1–10 g . In the centrifuge, the gravity level could be maintained long enough to ensure equilibrium in the lamp. The novel Imaging Laser Absorption Spectroscopy (ILAS) in the centrifuge allowed to obtain a 2D ground state atomic dysprosium density distribution in the lamp. The measurements of the Dy density by ILAS clearly showed that the setup and measurement techniques are a useful tool to get more insight into the lamp.

9.3.2 Extended axial segregation model

The Fischer model describes the axial segregation of the metal additives in an infinitely long lamp with a constant axial temperature profile. For our MH lamps this is not true, mainly close to the electrodes and higher g levels. We proposed an extended axial segregation model which takes this into account. Changing the temperature shifts the chemical equilibrium between salt molecules, atoms and ions. The radially integrated density of Dy atoms as a function of axial position was obtained by temperature calculations from numerical modelling.

9.3.3 Analysis

Two parameters were introduced to characterize the lamp. The axial inhomogeneity parameter α is a measure for the non-uniformity of any lamp parameter. We used it to describe the axial inhomogeneity in the additive density. The second parameter, the corrected axial segregation parameter λ_c , is only physically relevant if the temperature influence is not dominant. Two ILAS measurements showed that the temperature influence is much more pronounced for $10g$ (where the amount of convection is increased) than for $1g$. In practice, this means that for lamps with a larger buffer gas pressure the temperature influence is larger.

Various lamps with Hg and DyI₃ were measured by ILAS. The lamps of 20 mm burner length are on the right-hand side of the Fischer curve: increasing the gravity and thus convection, decreases α . The corrected segregation λ follows better the predicted behaviour by Fischer than the uncorrected parameter. For the short lamps (~ 15 mm) at $10g$ the highest density was found at the top of the lamp, due to the dominant temperature effect.

9.4 Emission spectroscopy

9.4.1 Lamps with DyI₃

The ILAS setup is accurate, but has been implemented for a particular geometry of the MH lamp and DyI₃ as salt filling, and can not be easily converted to other lamps. In addition to the ILAS technique, an easy and fast emission spectroscopy method was introduced, which derives axial intensity profiles for any wavelength of interest. From the line intensities the axial intensity inhomogeneity is deduced directly at different gravity conditions. For the lamps of 20 mm height, we are at the right-hand side of the Fischer curve. The short, wide lamps showed that we are more at the left in the Fischer curve. The results for these two lamp geometries are in agreement with ILAS results for lamps with DyI₃. The long, thin lamps showed that we are at the right-hand side of the Fischer curve, which is in agreement with ALI measurements [38]. After this validation, the emission spectroscopy can be used to characterize MH lamps with different salt mixtures.

9.4.2 Commercial lamps

For the commercial Philips CosmoWhite lamp the axial inhomogeneity of the different additives (Ca, Ce, Tl, Na) was obtained. In addition, the NaI density at the wall and the temperature were calculated for these lamps using Wesselink's method [82]. The obtained temperature is too low. Concluding from this result, for our lamp the claim in literature [82] that this method derives the temperature in quantitative is not valid. However, this method is still useful in qualitative terms. The measured intensity of the

additives was the highest and the axial intensity inhomogeneity the lowest at $1g$. The lamp is thus optimized for use at $1g$.

9.5 Comparison with numerical modelling

The competition between convection and diffusion was understood quantitatively by introducing a Peclet number defined as the ratio between the rate of radial diffusion and axial convection. The results from the experiments and those obtained by numerical modelling in PLASIMO showed good agreement. The factor 3 between the experimental obtained and numerical calculated density is explained by the difference in cold spot temperature. The competition between convection and diffusion is understood quantitatively.

2D images of the MH lamp, obtained by experiments and modelling, were shown and compared. The colour segregation that was observed at the webcam images at different gravity is directly correlated to the Dy density images obtained by ILAS. Modelling of the same lamp also offered Dy density images, which were in agreement with the experimental results.

9.6 Overview axial segregation parameters

In this thesis several parameters describing the axial segregation have been introduced. Each parameter has its advantages and disadvantages, and is only applicable under certain conditions.

Axial segregation λ (mm^{-1}), introduced by E. Fischer [28] (equation (2.3))

The model by Fischer assumes an infinitely long lamp without an axial temperature gradient. He obtained an exponential decay of the elemental Dy density as a function of the axial position in the lamp. A larger value of λ means more axial segregation in the lamp. This parameter has been used in earlier publications (e.g. [38, 86]) and chapters 2-4.

Corrected axial segregation λ_c (mm^{-1}), equation (5.13)

For our lamps, which are of finite length and have an axial temperature gradient, λ cannot be used. The change in temperature shifts the chemical equilibrium between Dy atoms and ions and DyI_3 molecules. Since the laser absorption spectroscopy methods presented in this thesis only measure ground state Dy atoms, we have to take this shift into account. For this reason the corrected axial segregation parameter λ_c was introduced. It has a physical meaning only if the temperature influence is not dominant. By

using the corrected parameter, we could extend the claims Fischer made for infinitely long lamps (dependence on pressure, radius etc.) to our situation.

Average segregation depth τ (dimensionless), equation (8.13)

This dimensionless parameter is the normalized Fischer parameter (λH) of an element averaged over the burner volume, where H is the length of the lamp burner. A value of $\tau \ll 1$ means that the element is homogeneously distributed over the lamp, whereas $\tau \gg 1$ corresponds to strong axial demixing. The advantage of this parameter compared with λ is that it is dimensionless and gives an average value over the lamp. This parameter has only been obtained for results from numerical modelling, because the pressure gradient cannot be obtained easily from experimental studies presented in this thesis.

Axial inhomogeneity α (dimensionless), equation (5.10)

The parameter expresses the degree of inhomogeneity in the axial direction for any plasma parameter and does not assume a particular shape for the axial profile. It is generally applicable and dimensionless, in contrast to the parameters λ , λ_c and τ . It is normalized for the length of the lamp burner and can be used to compare different geometries of the same type of lamp. A value of $\alpha = 0$ means the plasma parameter is homogeneous over the lamp axis. In this thesis α is used to describe the axial inhomogeneity in density (ILAS) and intensity (emission spectroscopy). When the temperature influence is not dominant, a relation exists between α and λ_c for ILAS measurements (equation (5.11)): $\alpha^2 \sim \lambda_c$ for $\lambda_c H \gtrsim 1$, where H is the height of the lamp burner.

Peclet number Pe (dimensionless), equation (8.12)

This parameter describes not the axial segregation itself, but the competition between convection and diffusion. A high Peclet number ($Pe \gg 1$) means that convection is dominant, whereas a low number ($Pe \ll 1$) means that diffusion is dominant. In both limiting cases axial segregation does not occur. When $Pe \approx 1$, maximal axial segregation occurs, the parameters λ , λ_c and α have a maximum and τ has a minimum.

9.7 General outlook

In this thesis the metal-halide lamp was investigated under varying gravity conditions using new diagnostics. Together with the thesis of T. Nimalasuriya [35], which deals with a poly-diagnostic (experimental) study of the MH lamp and the thesis of M.L. Beks [42], which is about the modelling of the MH lamp, this thesis has presented a complete

overview of the dominant processes which govern the segregation phenomena in MH lamps.

In addition to the results presented in these theses, it would be interesting to search for molecules in the MH lamp. This can be done by for instance using emission spectroscopy and laser induced fluorescence. Furthermore, lamps with new salt mixtures can be studied. In this thesis the ballast frequency and voltage waveform were fixed, but it might be interesting to change the frequency and waveform of the ballast and to study cataphoresis effects and electron energy distribution in the lamp. Another subject of research is the electrode region in the lamp [94–97].

All these measurements and numerical modelling should lead to a final grand numerical model of the MH lamp. The step to a grand model is not trivial. However, fundamental questions about the segregation phenomena have been solved by these three theses, which puts a grand model within reach. One would like to put the specifications into the model (such as lamp power, Hg pressure, geometry, salt mixture), and to obtain the lamp characteristics (such as light output, spectra) from the model. From the output of the model, the most interesting lamp settings can be selected, and these lamps can be made and investigated further. The ideal lamp should have an improved colour rendering, efficiency, stability and life time. Maintaining these properties, the lamp should have a good homogeneity of the additives, so no colour separation is present. The next step would be a model which requires the lamp power and size as input, and which derives the ideal geometry, pressure and salt mixture for the MH lamp.

Bibliography

- [1] International Energy Agency. *Light's Labour's Cost*. Organisation for Economic Co-operation and Development, 2006. ISBN 92-64-10951-X. <http://www.iea.org>.
- [2] W. W. Stoffels, T. Nimalasuriya, A. J. Flikweert, and H. C. J. Mulders. Discharges for lighting. *Plasma Phys. Control. Fusion*, 49:B505–B512, 2007.
- [3] G. G. Lister, J. E. Lawler, W. P. Lapatovich, and V. A. Godyak. The physics of discharge lamps. *Rev. Mod. Phys.*, 76:541–598, 2004.
- [4] P. Flesch. *Light and Light Sources. High-Intensity Discharge Lamps*. Springer, 2006.
- [5] A. J. Flikweert. Designing a contactless probe for optimization of flexible solar cells by measuring electrical parameters in-situ. Master's thesis, Eindhoven University of Technology, 2004.
- [6] E. A. G. Hamers, M. N. van den Donker, B. Stanowski, R. Schlatmann, and G. J. Jongerden. Helianthos: Roll-to-Roll Deposition of Flexible Solar Cell Modules. *Plasma Processes and Polymers*, 4:275–281, 2007.
- [7] C. Charles and R. W. Boswell. Current-free double-layer formation in a high-density helicon discharge. *Appl. Phys. Lett.*, 82(9):1356–1358, 2003.
- [8] C. Charles. Hydrogen ion beam generated by a current-free double layer in a helicon plasma. *Appl. Phys. Lett.*, 84(3), 2004.
- [9] C. Charles and R. W. Boswell. Time development of a current-free double-layer. *Physics of Plasmas*, 11(8):3808–3812, 2004.
- [10] C. Charles. High source potential upstream of a current-free electric double layer. *Physics of Plasmas*, 12:044508, 2005.
- [11] R. W. Boswell. *A Study of Waves in Gaseous Plasmas*. PhD thesis, School of Physical Sciences, The Flinders University of South Australia, 1970.
- [12] F. F. Chen and R. W. Boswell. Helicons – the past decade. *IEEE Transactions on Plasma Science*, 25(6):1245–1257, 1997.
- [13] A. W. Degeling, C. O. Jung, R. W. Boswell, and A. R. Ellingboe. Plasma production from helicon waves. *Phys. Plasmas*, 3(7):2788–2796, 1996.
- [14] A. R. Ellingboe and R. W. Boswell. Capacitive, inductive and helicon-wave modes of operation of a helicon plasma source. *Phys. Plasmas*, 3(7):2797–2804, 1996.
- [15] A. W. Degeling. *Plasma Production in a Large Volume Helicon Wave Discharge*. PhD thesis, The Australian National University, 1999.

-
- [16] C. M. Franck, O. Grulke, and T. Klinger. Magnetic fluctuation probe design and capacitive pickup rejection. *Rev. Sci. Instr.*, 73(11):3768–3771, 2002.
- [17] T. M. P. Briels. *Exploring streamer variability in experiments*. PhD thesis, Eindhoven University of Technology, 2007.
- [18] I. E. Kieft. *Plasma needle: exploring biomedical applications of non-thermal plasmas*. PhD thesis, Eindhoven University of Technology, 2005.
- [19] R. E. J. Sladek. *Plasma needle: non-thermal atmospherical plasmas in dentistry*. PhD thesis, Eindhoven University of Technology, 2006.
- [20] E. Stoffels, A. J. Flikweert, W. W. Stoffels, and G. M. W. Kroesen. Plasma needle: a non-destructive atmospheric plasma source for fine surface treatment of (bio)materials. *Plasma Sources Sci. Technol.*, 11:383–388, 2002.
- [21] H.-P. Stormberg. Axial and radial segregation in metal halide arcs. *J. Appl. Phys.*, 52:3233–3237, 1981.
- [22] G. L. Rogoff, A. E. Feuersanger, J. P. Drummey, and H. L. Rothwell, Jr. Determination of two-dimensional temperature and additive density distributions in a high-intensity-discharge lamp arc. *J. Appl. Phys.*, 62:4084–4089, 1987.
- [23] R. J. Zollweg. Reducing additive segregation in metal halide high-intensity discharge lamps. *J. IES.*, 5:12–19, 1975.
- [24] J. T. Dakin and W. Shyy. The prediction of convection and additive demixing in vertical metal halide discharge lamps. *J. Electrochem. Soc.*, 136:1210–1214, 1989.
- [25] J. T. Dakin, T. H. Rautenberg, Jr., and E. M. Goldfield. Anatomy of a vertical metal halide discharge. *J. Appl. Phys.*, 66:4074–4088, 1989.
- [26] G. A. Bonvallet and J. E. Lawler. Optical absorption spectroscopy on a metal-halide high intensity discharge arc lamp using synchrotron radiation. *J. Phys. D*, 36:1510–1518, 2003.
- [27] W. W. Stoffels, A. H. F. M. Baede, J. J. A. M. van der Mullen, M. Haverlag, and G. Zissis. Definition of a high intensity metal halide discharge reference lamp. *Meas. Sci. Technol.*, 17:N67, 2006.
- [28] E. Fischer. Axial segregation of additives in mercury-metal-halide arcs. *J. Appl. Phys.*, 47:2954–2960, 1976.
- [29] X. Zhu. *Active spectroscopy on HID lamps - Exploration of various methods*. PhD thesis, Eindhoven University of Technology, 2005.
- [30] M. Yamane and M. Suenaga. Transport of silica in rare earth iodide arc tubes. *J. Appl. Phys.*, 54:107–111, 1982.
- [31] J. J. A. M. van der Mullen. *Excitation equilibria in plasmas - a classification*. PhD thesis, Eindhoven University of Technology, 1986.
- [32] A. J. Flikweert, T. Nimalasuriya, C. H. J. M. Groothuis, G. M. W. Kroesen, and W. W. Stoffels. Axial segregation in high intensity discharge lamps measured by laser absorption spectroscopy. *J. Appl. Phys.*, 98:073301, 2005. **See chapter 2.**
- [33] A. J. Flikweert, M. van Kemenade, T. Nimalasuriya, M. Haverlag, G. M. W. Kroesen, and W. W. Stoffels. Axial segregation in metal-halide lamps under varying gravity conditions during parabolic flights. *J. Phys. D*, 39:1599–1605, 2006. **See chapter 3.**

-
- [34] T. Nimalasuriya, N. B. M. Pupat, A. J. Flikweert, W. W. Stoffels, M. Haverlag, and J. J. A. M. van der Mullen. Optical emission spectroscopy of metal-halide lamps: Radially resolved atomic state distribution functions of dy and hg. *J. Appl. Phys.*, 99:053302, 2006.
- [35] T. Nimalasuriya. *Transport Phenomena in Metal-Halide Lamps – A poly-diagnostic study*. PhD thesis, Eindhoven University of Technology, 2007.
- [36] T. Nimalasuriya, J. J. Curry, C. J. Sansonetti, E. J. Ridderhof, A. J. Flikweert, W. W. Stoffels, M. Haverlag, and J. J. A. M. van der Mullen. X-ray induced fluorescence measurement of the density distribution of Dy and Hg in a metal-halide lamp. *XXVIIIth International Conference on Phenomena in Ionized Gases*, 2005.
- [37] A. J. Flikweert, T. Nimalasuriya, G. M. W. Kroesen, and W. W. Stoffels. Imaging laser absorption spectroscopy of the metal-halide lamp in a centrifuge (1–10g). *Plasma Sources Sci. Technol.*, 16:606–613, 2007. **See chapter 4.**
- [38] T. Nimalasuriya, G. M. Thubé, A. J. Flikweert, M. Haverlag, G. M. W. Kroesen, W. W. Stoffels, and J. J. A. M. van der Mullen. Axial segregation in metal-halide lamps under varying gravity conditions ranging from 1 to 10 g. *J. Phys. D*, 40:2839–2846, 2007.
- [39] A. J. Flikweert, M. L. Beks, T. Nimalasuriya, G. M. W. Kroesen, J. J. A. M. van der Mullen, and W. W. Stoffels. 2-D Images of the Metal-Halide Lamp Obtained by Experiment and Model. *IEEE Transactions on Plasma Science*, 36:1174–1175, 2008. **See chapter 8.**
- [40] European Space Agency. <http://www.esa.int>.
- [41] T. Nimalasuriya, A. J. Flikweert, M. Haverlag, P. C. M. Kemps, G. M. W. Kroesen, W. W. Stoffels, and J. J. A. M. van der Mullen. Metal halide lamps in the international space station ISS. *J. Phys. D*, 39:2993–3001, 2006.
- [42] M. L. Beks. *Modelling Additive Transport in Metal Halide Lamps*. PhD thesis, Eindhoven University of Technology, 2008.
- [43] M. van Kemenade. Axial segregation in high intensity discharge lamps. Master’s thesis, Eindhoven University of Technology, 2004.
- [44] Harvard-Smithsonian Center for Astrophysics. Kurucz Atomic Line Database. <http://cfa-www.harvard.edu/amdata/ampdata/kurucz23/sekur.html>.
- [45] N. V. Gorshkov, V. A. Komarovski, A. L. Osherovich, N. P. Penkin, and R. Khefferlin. *Opt. Spectr.*, 48:362–364, 1980.
- [46] A. P. Thorne. *Spectrophysics*. Chapman and Hall & Science PaperBacks London, 1974.
- [47] E. A. H. Timmermans. *Atomic and Molecular Excitation Processes in Microwave Induced Plasmas*. PhD thesis, Eindhoven University of Technology, 1999.
- [48] M. J. Buie, J. T. P. Pender, J. P. Holloway, T. Vincent, P. L. G. Ventzek, and M. L. Brake. Abel’s inversion applied to experimental spectroscopic data with off axis peaks. *J. Quant. Spectrosc. Radiat. Transfer*, 55:231–243, 1996.
- [49] J. J. Curry, M. Sakai, and J. E. Lawler. Measurement of the Hg distribution in a high-pressure arc lamp by x-ray absorption. *J. Appl. Phys.*, 84:3066–3072, 1998.
- [50] T. Nimalasuriya, J. J. Curry, C. J. Sansonetti, E. J. Ridderhof, S. D. Shastri, A. J. Flikweert, W. W. Stoffels, M. Haverlag, and J. J. A. M. van der Mullen. X-ray induced fluorescence measurement of the segregation in a DyI₃-Hg metal-halide lamp. *J. Phys. D*, 40:2831–2838, 2007.

-
- [51] W. W. Stoffels, P. C. M. Kemps, J. Beckers, G. M. W. Kroesen, and M. Haverlag. Light emission of metal halide lamps under micro- and hypergravity conditions. *Appl. Phys. Lett.*, 87:241501, 2005.
- [52] W. W. Stoffels, A. J. Flikweert, T. Nimalasuriya, J. J. A. M. van der Mullen, G. M. W. Kroesen, and M. Haverlag. Metal Halide Lamps: gravitational influence on color separation. *Pure Appl. Chem.*, 78:1239–1252, 2006.
- [53] W. Elenbaas. *The high pressure mercury vapour discharge*. North-Holland publishing company Amsterdam, 1951.
- [54] A. Hartgers, H. W. P. van der Heijden, M. L. Beks, J. van Dijk, and J. J. A. M. van der Mullen. *J. Phys. D*, 38:3422–3429, 2005.
- [55] M. A. Lieberman and A. J. Lichtenberg. *Principles of plasma discharges and materials processing*. John Wiley and Sons, 1994.
- [56] Philips Research, Aachen (Germany). Thermodynamical database.
- [57] Charles D. Hodgman, Robert C. Weast, and David R. Lide. *Handbook of chemistry and physics*, volume 85. CRC Press, 2004–2005.
- [58] J. Beckers. An experimental study of the integrated light output of high intensity discharge lamps under various gravity conditions. Master’s thesis, Eindhoven University of Technology, 2004.
- [59] Novespace. <http://www.novespace.fr>.
- [60] SBIG Santa Barbara Instrument Group. <http://www.sbig.com>.
- [61] ZEMAX optical design and analysis software. <http://www.zemax.com>.
- [62] L. P. Bakker. *Plasma Control of the Emission Spectrum of Mercury-Noble-gas Discharges*. PhD thesis, Eindhoven University of Technology, 2000.
- [63] G. Pretzler, H. Jäger, T. Neger, H. Philipp, and J. Woisetschläger. Comparison of different methods of Abel inversion using computer simulated and experimental side-on data. *Z. Naturforsch.*, 47a:955–970, 1992.
- [64] S. I. Sudharsanan. *The Abel inversion of noisy data using discrete integral transforms*. PhD thesis, Knoxville: University of Tennessee, 1986.
- [65] Avinash C. Kak and Malcolm Slaney. *Principles of computerized tomographic imaging*. IEEE Press, 1988.
- [66] SRON Netherlands Institute for Space Research. <http://www.sron.nl>.
- [67] A. J. Flikweert, T. Nimalasuriya, G. M. W. Kroesen, M. Haverlag, and W. W. Stoffels. The metal-halide lamp under varying gravity conditions measured by emission and laser absorption spectroscopy. *Submitted to Microgravity Science and Technology*, 2008. **See chapter 1.**
- [68] C. Kenty. *J. Appl. Phys.*, 9:53, 1938.
- [69] R. J. Zollweg. Convection in vertical mercury and metal halide arc lamps. *J. IES.*, 8:126–131, 1979.
- [70] M. L. Beks, A. J. Flikweert, T. Nimalasuriya, W. W. Stoffels, and J. J. A. M. van der Mullen. Competition between convection and diffusion in a metal halide lamp, investigated by numerical simulations and imaging laser absorption spectroscopy. *J. Phys. D*, 41:144025, 2008. **See chapter 8.**

-
- [71] T. Nimalasuriya, M. L. Beks, A. J. Flikweert, M. Haverlag, W. W. Stoffels, G. M. W. Kroesen, and J. J. A. M. van der Mullen. Metal-halide lamps in micro-gravity, experiment and model. *J. Phys. D*, 41:144024, 2008.
- [72] A. J. Flikweert, A. F. Meunier, T. Nimalasuriya, G. M. W. Kroesen, and W. W. Stoffels. Imaging Laser Absorption Spectroscopy of the metal-halide lamp under hyper-gravity conditions ranging from 1–10 g. *Accepted for publication in J. Phys. D*, 41, 2008. **See chapter 6.**
- [73] A. J. Flikweert, M. L. Beks, T. Nimalasuriya, G. M. W. Kroesen, M. Haverlag, J. J. A. M. van der Mullen, and W. W. Stoffels. Semi-empirical model for axial segregation in metal-halide lamps. *Accepted for publication in J. Phys. D*, 41, 2008. **See chapter 5.**
- [74] C. J. Dasch. One-dimensional tomography: a comparison of abel, onion-peeling, and filtered backprojection methods. *Appl. Optics*, 31:1146–1152, 1992.
- [75] N. V. Denisova. Maximum-entropy-based tomography for gas and plasma diagnostics. *J. Phys. D*, 31:1888–1895, 1998.
- [76] NIST Atomic Spectra Database. <http://physics.nist.gov/cgi-bin/ASD/lines-pt.pl>.
- [77] T. Nimalasuriya, X. Zhu, E. J. Ridderhof, M. L. Beks, M. Haverlag, N. Denisova, W. W. Stoffels, and J. J. A. M. van der Mullen. X-ray absorption of the Hg distribution in a commercial metal-halide lamp. *J. Phys. D*, 41:144022, 2008.
- [78] Philips CosmoPolis lamp. <http://www.philips.com/cosmopolis>.
- [79] W. J. van den Hoek, H. C. M. van den Nieuwenhuizen, and H. P. Stormberg. *Philips-Journal-of-Research*, 37:129–144, 1982.
- [80] H. Bartels. Eine neue Methode zur Temperaturmessung an hochtemperierten Bogensäulen, I. Teil. *Z. Phys.*, 127:243–273, 1950.
- [81] H. Bartels. Eine neue Methode zur Temperaturmessung an hochtemperierten Bogensäulen, II. Teil. *Z. Phys.*, 128:546–573, 1950.
- [82] G. Wesselink, D. de Mooy, and M. J. C. van Gemert. Temperature determination of high-pressure optically thick gas discharges by a modified bartels’ method. *J. Phys. D.*, 6:L27–L30, 1973.
- [83] W. Lochte-Holtgreven, editor. *Plasma diagnostics*. North-Holland publishing company Amsterdam, 1968.
- [84] I. S. Fishman, G. G. L’lin, and M. Kh. Salakhov. Temperature determination of an optically thick plasma from self-reversed spectral lines. *J. Phys. D*, 20:728–740, 1986.
- [85] V. Bakshi and W. C. Nunnally. Measurement of Temperatures in Optically Thick Railgun Plasm Armatures. *IEEE Trans. on Magnetics*, 31:673–677, 1995.
- [86] M. L. Beks, A. Hartgers, and J. J. A. M. van der Mullen. Demixing in a metal halide lamp, results from modelling. *J. Phys. D*, 39:4407, 2006.
- [87] M. L. Beks, J. van Dijk, A. Hartgers, and J. J. A. M. van der Mullen. A study on the effects of geometry on demixing in metal-halide lamps. *IEEE Trans. on Plasma Science*, 35:1335–1340, 2007.
- [88] Dale E. Work. Chemistry of metal halide lamps: a review. *Light. Res. Tech.*, 13:143, 1987.
- [89] Plasimo. <http://plasimo.phys.tue.nl/>.

-
- [90] J. A. M. van der Mullen. Excitation equilibria in plasmas; a classification. *Physics Reports*, 2&3(191):109–220, 1990.
- [91] H. van der Heijden and J. J. A. M. van der Mullen. General treatment of the interplay between fluid and radiative transport phenomena in symmetric plasmas: the sulfur lamp as a case study. *J. Phys. D*, 35:2112–2125, 2002.
- [92] C. W. Johnston, H. van der Heijden, G. Janssen, J. van Dijk, and J. J. A. M. van der Mullen. A self consistent lte model of microwave driven high pressure sulfur lamp. *J. Phys. D*, 35:342–351, 2002.
- [93] S. V. Patankar. *Numerical Heat Transfer and Fluid Flow*. New York: McGraw-Hill, 1980.
- [94] S. Lichtenberg, L. Dabringhausen, O. Langenscheidt, and J. Mentel. The plasma boundary layer of HID-cathodes: modelling and numerical results. *J. Phys. D*, 38:3112–3127, 2005.
- [95] L. Dabringhausen, O. Langenscheidt, S. Lichtenberg, M. Redwitz, and J. Mentel. Different modes of arc attachment at HID cathodes: simulation and comparison with measurements. *J. Phys. D*, 38:3128–3142, 2005.
- [96] M. Redwitz, O. Langenscheidt, and J. Mentel. Spectroscopic investigation of the plasma boundary layer in front of HID-electrodes. *J. Phys. D*, 38:3143–3154, 2005.
- [97] G. M. J. F. Luijks, S. Nijdam, and H. van Esveld. Electrode diagnostics and modelling for ceramic metal halide lamps. *J. Phys. D*, 38:3163–3169, 2005.

Summary

Spectroscopy on Metal-Halide Lamps under Varying Gravity Conditions

Worldwide, 20% of all electricity is used for lighting. For this reason, efficient lamps are economically and ecologically important.

High intensity discharge (HID) lamps are efficient lamps. The most common HID lamp these days is the metal-halide (MH) lamp. MH lamps have a good colour rendering index. They are high pressure lamps based on arc emission. These lamps are mainly used for applications where a high light output is desired; examples are shop lighting, street lighting, flood lighting of sport stadiums and city beautification. MH lamps have a high efficiency (up to 40%) and emit white light.

The MH lamp contains a buffer gas (usually mercury) and additives that act as the prime radiator in the visible. These additives increase the efficiency and the colour rendering. The additive is dosed as salt; in this thesis mainly dysprosium iodide (DyI_3) is used as additive.

The aim of this thesis is to characterize a well verifiable MH lamp and obtain a set of reliable measurement data. The experimentally obtained data is used to validate existing numerical models of the MH lamp, which gain a better understanding of the plasma properties and transport phenomena in the MH lamp.

When the lamp is burning vertically, segregation of the additives and colour separation occurs. The non-uniform light output has a bad influence on the efficiency and the colour rendering of the lamp. The distribution of the Dy atoms is determined by convection and diffusion in the lamp.

Convection is induced by gravity and therefore the lamp is measured under varying gravity conditions. Besides laboratory experiments the lamp is investigated during parabolic flights. Here the lamp is measured during periods of about 20 s of micro-gravity ($0g$) and hyper-gravity ($\sim 1.8g$). The lamp is also placed in a centrifuge ($1-10g$). This centrifuge, with a diameter of about 3 m, is used as a tool to vary the (artificial) gravity and thus the amount of convection for a longer time than at the

parabolic flights to assure stable arc conditions.

To develop better lamps, the knowledge from the gravitational study can be applied to other parameters that influence the amount of convection. Examples in practice are changing the buffer gas pressure or the ratio between the length and radius of a lamp.

At $1g$ the radially and axially resolved density of ground state atomic Dy is measured by means of laser absorption spectroscopy. The radially resolved measurements show a hollow density profile with a maximum in the Dy density somewhere between the centre and the wall. In the outer region molecules dominate, while the centre is depleted due to ionization of Dy.

During the parabolic flights, line-of-sight density profiles of atomic ground state dysprosium were obtained at one axial position of the lamp by means of one-dimensional laser absorption spectroscopy. These profiles are a measure for the amount of axial segregation. The measured lamp voltage and integrated light output are in agreement with the results for the dysprosium density. Three processes with different time constants play a role when switching from hyper-gravity to micro-gravity. Axial diffusion is the slowest, and its time constant (~ 30 s) is proportional to the amount of mercury. As a result, at the end of the micro-gravity phase the lamp still is not in equilibrium.

The novel Imaging Laser Absorption Spectroscopy (ILAS) obtains the 2D ground state atomic dysprosium density distribution in the lamp. The measurements of the Dy density by ILAS clearly show that the setup and measurement technique are a useful tool to get more insight into the lamp.

The theory of E. Fischer gives the amount of axial segregation as a function of the amount of convection for an infinitely long lamp. This model is extended for our lamps, which are of finite length and have an axial temperature gradient. A change of temperature shifts the chemical equilibrium between salt molecules, atoms and ions. From this extended model the corrected Fischer parameter λ_c is introduced, which only has physical meaning when the temperature influence is not dominant. The axial inhomogeneity parameter α gives the non-uniformity in axial direction of any lamp property. We use it to describe the axial inhomogeneity in the additive density.

Various lamps with Hg and DyI₃ are measured by ILAS. The corrected segregation parameter λ_c presented in this thesis follows the predicted behaviour by Fischer better than the Fischer parameter λ , which does not take the temperature influence into account. The various lamps are on different positions on the Fischer curve. Furthermore, at $10g$, short lamps show the highest Dy density at the top of the lamp, caused by the dominant temperature effect.

The ILAS setup is accurate, but has been implemented for a particular geometry of the MH lamp and DyI₃ as salt filling, and can not be easily converted to other lamps. In addition, an easy and fast emission spectroscopy method is introduced, which derives axial intensity profiles for any wavelength of interest. From the line intensities the axial intensity inhomogeneity is deduced directly at different gravity conditions. The results obtained by using this technique are in agreement with the ILAS results for lamps with DyI₃, and next applied to the commercial Philips CosmoWhite lamp with a different

salt mixture.

The ILAS measurements are compared with results obtained by numerical modelling with the TU/e plasma modelling platform PLASIMO and show good agreement. The competition between convection and diffusion is understood quantitatively.

In conclusion: the measurements on the MH lamps in this thesis are successful and are a set of reliable and consistent data. The results obtained by experiment and model are in agreement; the set of measurement data can be used for validation of future numerical models.

Samenvatting

Spectroscopie op Metaalhalogenidelampen onder Verschillende Zwaartekrachtcondities

Wereldwijd wordt 20% van de elektriciteit gebruikt voor verlichting. Efficiënte lampen zijn daarom belangrijk, zowel om economische redenen als vanwege de positieve milieuaspecten.

Hoge-intensiteit-gasontladinglampen (high intensity discharge lamps, HID) zijn efficiënte lampen. De meest voorkomende HID-lamp is de metaalhalogenidelamp (MH-lamp). MH-lampen hebben een goede kleurweergave. Het zijn hogedruklampen gebaseerd op de lichtemissie van een elektrische boog (plasma). Ze worden met name toegepast waar een hoge lichtintensiteit gewenst is, zoals in etalageverlichting, straatverlichting, de verlichting van sportstadions en gevelverlichting van gebouwen. MH-lampen zijn erg efficiënt (tot wel 40%) en geven wit licht.

De MH-lamp bevat een buffergas (meestal kwik) en additieven die vooral in het zichtbare deel van het spectrum licht uitzenden. De additieven verhogen de efficiëntie en de kleurweergave. Ze worden als zout toegevoegd. In dit proefschrift gebruiken we vooral dysprosiumjodide (DyI_3) als zoutadditief.

Het doel van dit proefschrift is het karakteriseren van een goed verifieerbare lamp en het verkrijgen van een set betrouwbare meetdata. De experimenteel verkregen data wordt gebruikt om bestaande numerieke modellen van de MH-lamp te verifiëren, zodat we de plasmaeigenschappen en de transportverschijnselen in de lamp beter kunnen gaan begrijpen.

Als de lamp in verticale positie brandt, treedt er segregatie van de additieven op en zien we kleurscheiding. Het niet-uniforme licht verlaagt de efficiëntie en verslechtert de kleurweergave van de lamp. De verdeling van de Dy-atomen wordt bepaald door convectie en diffusie in de lamp.

Convectie wordt geïnduceerd door zwaartekracht en daarom wordt de lamp gemeten onder verschillende zwaartekrachtcondities. De lamp wordt onderzocht in het laboratorium en tijdens paraboolvluchten. Tijdens deze vluchten meten we de lamp tijdens

perioden van ongeveer 20 s van microzwaartekracht ($0g$, waar g de zwaartekracht op aarde is) en hyperzwaartekracht ($\sim 1.8g$). De lamp wordt ook in een centrifuge ($0-10g$) geplaatst. Deze centrifuge, met een diameter van ongeveer 3 m, wordt gebruikt als instrument om de (kunstmatige) zwaartekracht te variëren en hiermee de convectiesnelheid in de lamp te veranderen. De centrifuge kan langdurig op een constant zwaartekrachtniveau blijven, in tegenstelling tot de paraboolvluchten, waar slechts periodes van 20 s beschikbaar zijn. Hierdoor zijn we er in de centrifuge zeker van dat de lamp gestabiliseerd is.

Om betere lampen te kunnen ontwikkelen kan de kennis van de zwaartekrachtstudie worden toegepast op andere parameters die de convectiesnelheid beïnvloeden. Voorbeelden uit de praktijk zijn het veranderen van de druk van het buffergas of het wijzigen van de verhouding tussen de lengte en straal van de lamp.

Bij $1g$ meten we de radiaal en axiaal opgeloste dichtheid van de Dy-atomen in de grondtoestand. Dit wordt gedaan met behulp van laserabsorptiespectroscopie. De radiaal opgeloste metingen laten een hol dichtheidsprofiel zien. Het maximum in de dysprosiumdichtheid ligt ergens tussen het centrum en de wand van de lamp. In het buitenste gebied domineren de moleculen. Verder is in het centrum de atomaire Dy-dichtheid lager doordat er ionisatie optreedt.

Tijdens de paraboolvluchten meten we laterale dichtheidsprofielen van Dy-atomen in de grondtoestand. Dit doen we met behulp van eendimensionale laserabsorptiespectroscopie op één bepaalde axiale positie in de lamp. Uit deze profielen halen we de mate van axiale segregatie. De gemeten lampspanning en de geïntegreerde lichtopbrengst stemmen overeen met de resultaten voor de dysprosiumdichtheid. Drie processen met verschillende tijdconstanten zijn van belang als we van hyperzwaartekracht naar microzwaartekracht gaan. Axiale diffusie is het traagst en de tijdconstante (~ 30 s) is evenredig met de hoeveelheid kwik. Vanwege de tijdschaal van deze constante is de lamp aan het einde van de fase van microzwaartekracht nog niet gestabiliseerd.

De nieuwe meettechniek Beeldvormende Laserabsorptiespectroscopie (Imaging Laser Absorption Spectroscopy, ILAS) meet de 2D-verdeling van de dichtheid van de grondtoestand van het Dy-atoom over de lamp. De metingen van de Dy-dichtheid met behulp van ILAS laten duidelijk zien dat de opstelling en meettechniek een bruikbaar hulpmiddel zijn om meer inzicht in de lamp te verkrijgen.

E. Fischer heeft een theorie ontwikkeld die de mate van axiale segregatie als functie van de hoeveelheid convectie beschrijft, voor een oneindig lange lamp. We breiden dit model uit voor onze lampen, die een eindige lengte en een axiale temperatuurgradiënt hebben. Door het veranderen van de temperatuur verschuift het chemisch evenwicht tussen zoutmoleculen, -atomen en -ionen. Dit nieuwe model geeft de gecorrigeerde Fischerparameter λ_c , die alleen kan worden bepaald als de invloed van de temperatuur niet dominant is. De axiale inhomogeniteitsparameter α is een maat voor de niet-uniformiteit van een willekeurige lampeigenschap in axiale richting. Wij gebruiken de parameter α als maat voor de axiale inhomogeniteit van de dichtheid van het additief.

Diverse lampen met Hg en DyI₃ worden gemeten met behulp van ILAS. De gecor-

rigeerde segregatieparameter λ_c geïntroduceerd in dit proefschrift volgt het gedrag dat voorspeld wordt in het model van Fischer beter dan de oorspronkelijke Fischer parameter λ , omdat deze het temperatuureffect niet meeneemt. De verschillende lampen liggen op andere posities op de Fischercurve. In korte lampen is bij $10g$ de Dy-dichtheid het hoogste bovenin de lamp. Dit wordt veroorzaakt door het dominante temperatuureffect.

De ILAS-techniek is nauwkeurig, maar is geoptimaliseerd voor een bepaalde geometrie van de MH-lamp en DyI₃ als zoutvulling en kan niet eenvoudig aan een andere lamp worden aangepast. Als toevoeging aan deze meettechniek wordt een eenvoudige en snelle methode van emissiespectroscopie geïntroduceerd. Deze methode bepaalt axiale intensiteitsprofielen voor elke gewenste golflengte. Vervolgens wordt uit de lijnintensiteiten direct de inhomogeniteit in de axiale intensiteitverdeling bepaald, onder verschillende zwaartekrachtcondities. De met deze techniek verkregen meetresultaten komen overeen met de resultaten van de ILAS-metingen voor lampen met DyI₃. Vervolgens wordt de techniek toegepast op de commerciële Philips CosmoWhite-lamp met een andere zoutmix.

De ILAS-metingen worden vergeleken met de resultaten die verkregen zijn met numeriek modelleren met TU/e-plasmamodelleringsplatform PLASIMO. De resultaten laten een goede overeenkomst zien. Door de resultaten naast elkaar te leggen, kunnen we de competitie tussen convectie en diffusie kwalitatief begrijpen.

Concluderend: de metingen aan de MH-lampen zijn succesvol en leveren betrouwbare en consistente data. De overeenkomst tussen experiment en model is goed en de set meetdata kan gebruikt worden ter validatie van nieuwe numerieke modellen.

Dankwoord

Ruim vier jaar geleden vroeg professor Gerrit Kroesen aan mij of ik interesse had in een promotieonderzoek op het gebied van gasontladingslampen. Ik kende de groep EPG (Elementaire Processen in Gasontladingen) al van mijn interne stage en hoefde daarom ook niet lang na te denken. Winfred Stoffels zou mijn directe begeleider worden. Het opbouwen van een nieuw experiment was een uitdagende bezigheid en ik wil dan ook Winfred Stoffels en Gerrit Kroesen bedanken voor de ondersteuning en de discussies die hebben geleid tot het totstandkomen van het proefschrift. Mijn tweede promotor Marco Haverlag, tevens werkzaam bij Philips Lighting, wil ik bedanken voor de interessante discussies en de uitgebreide kennis van de lampen. I also would like to thank the other members of PhD committee for the discussions and reviewing of my thesis: the professors Anton Darhuber, Peter Awakowicz, Georges Zissis and Joost van der Mullen.

Het werk zou niet gelukt zijn zonder een goede vakgroep, met interessante discussies en inspiratie. Ik wil hierbij dan ook graag alle (oud-)EPG-ers bedanken. Als eerste wil ik mijn (oud-)kamerogenoten bedanken: Tanya Nimalasuriya, Xiaoyan Zhu, Katia Iordanova en Arij Rijke. Met Tanya Nimalasuriya en Mark Beks had ik hetzelfde onderzoeksobject: de lamp. Met hen heb ik dan ook veel nuttige discussies gehad. Charlotte Groothuis, Loek Baede, Evert Ridderhof en Huib Schouten wil ik bedanken voor alle ondersteuning aan het opbouwen en onderhouden van de opstelling. Joost van der Mullen en Jan van Dijk wil ik ook nog specifiek noemen vanwege de interessante discussies en heldere uitleg. Rina Boom als secretaresse van de groep, voor alle administratieve hulp en informele gesprekken.

In my second year I got the opportunity to carry out a traineeship in Australia. I went to the Space Plasma, Power and Propulsion group of Rod Boswell at the Australian National University in Canberra. I would like to thank the people for the pleasant and valuable time I had, especially Christine Charles for the supervision, Ane Aanesland for a lot of help and Michael West for being my roommate.

Three French students carried out their traineeships and contributed to the experimental results: Gregoire Saget, Anthony Meunier and Laurence Navarro. They contributed a lot to the knowledge about the metal-halide lamps. Voordat ik begon hebben meerdere studenten aan voorbereidende experimenten gewerkt in het Arges-project. Ik

wil Mark van Kemenade bedanken voor de aanzet voor de laserabsorptiemethode en de metingen tijdens de paraboolvluchten in Bordeaux. Het Arges-team bestond uit een grote groep mensen van allerlei disciplines. Ik wil de mensen van de Gemeenschappelijke Technische Dienst en de Bedrijfsgroep Laboratoriumautomatisering bedanken voor het opbouwen van het experiment. In het bijzonder wil ik noemen Jurgen Bulsink, Erwin Dekkers, Toon Gevers, Rob de Kluijver, Patrick de Laat, Jovita Moerel, Wim Peters en Gerard Harkema. Voor kleinere klussen stond de werkplaats van natuurkunde ook altijd ter beschikking: Marius Bogers en de klusjesmannen en -vrouwen.

Philips Lighting heeft ook aan het werk bijgedragen, in de persoon van Marco Haverlag, door het aanleveren van de testlampen en het beschikbaar stellen van meetfaciliteiten. De excursie naar de lampenfabriek van Philips Turnhout was erg indrukwekkend. Pieter Kramer van Laser 2000 en de mensen van Sacher zijn belangrijk geweest voor de laser die in de opstelling gebruikt wordt. Bedankt voor het geduld met de soms moeilijke opstelling en het zoeken van oplossingen voor problemen die we daarbij tegenkwamen.

Tenslotte wil ik al mijn vrienden en mijn familie bedanken. Mijn ouders en zus Willemien voor het geduld en de steun die ik kreeg tijdens de promotieperiode, en mijn neef Johan Flikweert, die naast Willemien mijn tweede paranimf zal zijn.

List of publications

Journals

Emission spectroscopy for characterizing metal-halide lamps

A.J. Flikweert, T. Nimalasuriya, G.M.W. Kroesen, M. Haverlag and W.W. Stoffels, Journal of Physics D-Applied Physics **41** (2008) issue 18

Imaging Laser Absorption Spectroscopy of the metal-halide lamp under hyper-gravity conditions ranging from 1–10 g

A.J. Flikweert, A.F. Meunier, T. Nimalasuriya, G.M.W. Kroesen and W.W. Stoffels, Journal of Physics D-Applied Physics **41** (2008) issue 18

Semi-empirical model for axial segregation in metal-halide lamps

A.J. Flikweert, M.L. Beks, T. Nimalasuriya, G.M.W. Kroesen, M. Haverlag, J.J.A.M. van der Mullen and W.W. Stoffels, Journal of Physics D-Applied Physics **41** (2008) issue 18

2-D Images of the Metal-Halide Lamp Obtained by Experiment and Model

A.J. Flikweert, M.L. Beks, T. Nimalasuriya, G.M.W. Kroesen, J.J.A.M. van der Mullen and W.W. Stoffels, IEEE Transactions on Plasma Science **36(4)** (2008) 1174–1175

The metal-halide lamp under varying gravity conditions measured by emission and laser absorption spectroscopy

A.J. Flikweert, T. Nimalasuriya, G.M.W. Kroesen, M. Haverlag and W.W. Stoffels, submitted to Microgravity - Science and Technology (2008)

Competition between convection and diffusion in a metal halide lamp, investigated by numerical simulations and imaging laser absorption spectroscopy

M.L. Beks, A.J. Flikweert, T. Nimalasuriya, W.W. Stoffels and J.J.A.M. van der Mullen, Journal of Physics D-Applied Physics **41** (2008) 144025

Metal-halide lamps in micro-gravity, experiment and model

T. Nimalasuriya, M.L. Beks, A.J. Flikweert, M. Haverlag, W.W. Stoffels, G.M.W. Kroesen and J.J.A.M. van der Mullen, *Journal of Physics D-Applied Physics* **41** (2008) 144022

Imaging Laser Absorption Spectroscopy of the metal-halide lamp in a centrifuge (1–10g)

A.J. Flikweert, T. Nimalasuriya, G.M.W. Kroesen and W.W. Stoffels, *Plasma Sources Science & Technology* **16(3)** (2007) 606–613

Axial segregation in metal-halide lamps under gravity conditions ranging from 1g to 10g

T. Nimalasuriya, G.M. Thubé, A.J. Flikweert, M. Haverlag, G.M.W. Kroesen, W.W. Stoffels and J.J.A.M. van der Mullen, *Journal of Physics D-Applied Physics* **40** (2007) 2839–2846

Discharges for lighting

W.W. Stoffels, T. Nimalasuriya, A.J. Flikweert and H.C.J. Mulders, *Plasma Physics and Controlled Fusion* **49** (2007) B505–B512

X-ray induced fluorescence measurement of segregation in a DyI₃-Hg metal-halide lamp

T. Nimalasuriya, J.J. Curry, C.J. Sansonetti, E.J. Ridderhof, S.D. Shastri, A.J. Flikweert, W.W. Stoffels, M. Haverlag and J.J.A.M. van der Mullen, *Journal of Physics D-Applied Physics* **40** (2007) 2831–2838

Axial segregation in metal-halide lamps under varying gravity conditions during parabolic flights

A.J. Flikweert, M. van Kemenade, T. Nimalasuriya, M. Haverlag, G.M.W. Kroesen and W.W. Stoffels, *Journal of Physics D-Applied Physics* **39(8)** (2006) 1599–1605 **On the list of best articles published in J. Phys. D. in 2006**

Metal halide lamps in the international space station ISS

T. Nimalasuriya, A.J. Flikweert, M. Haverlag, P. Kemps, G.M.W. Kroesen, W.W. Stoffels and J.J.A.M. van der Mullen, *Journal of Physics D-Applied Physics* **39** (2006) 2993–3001

Metal halide lamps: Gravitational influence on color separation

W.W. Stoffels, A.J. Flikweert, T. Nimalasuriya, J.J.A.M. van der Mullen, G.M.W. Kroesen and M. Haverlag, *Pure Appl. Chem.* **78(6)** (2006) 1239–1252

Optical emission spectroscopy of metal-halide lamps: Radially resolved atomic state distribution functions of Dy and Hg

T. Nimalasuriya, N.B.M. Pupat, A.J. Flikweert, W.W. Stoffels, M. Haverlag and J.J.A.M. van der Mullen, *Journal of Applied Physics* **99** (2006) 053302

Axial segregation in high intensity discharge lamps measured by laser absorption spectroscopy

A.J. Flikweert, T. Nimalasuriya, C.H.J.M. Groothuis, G.M.W. Kroesen and W.W. Stoffels, *Journal of Applied Physics* **98(7)** (2005) 073301

Plasma needle: a non-destructive atmospheric plasma source for fine surface treatment of (bio)materials

E. Stoffels, A.J. Flikweert, W.W. Stoffels and G.M.W. Kroesen, *Plasma Sources Science & Technology* **11** (2002) 383–388

Oral presentations

The metal-halide lamp investigated in the centrifuge (1-10g) by Imaging Laser Absorption Spectroscopy and emission spectroscopy

A.J. Flikweert, Group Seminar Wendelstein, Max-Planck-Institut für Plasmaphysik (30 June 2008), Greifswald, Germany

Axial segregation in a metal-halide lamp at 1-10G measured by emission spectroscopy

A.J. Flikweert, L. Navarro, T. Nimalasuriya, G.M.W. Kroesen, and W.W. Stoffels, 35th IEEE International Conference on Plasma Science (15–19 June 2008), Karlsruhe, Germany

Metal-halide lamps under varying gravity conditions measured by emission and laser absorption spectroscopy

A.J. Flikweert, T. Nimalasuriya, G.M.W. Kroesen and W.W. Stoffels, Microgravity Platform / NL-Gravitybijeekomst (28 March 2008), NIVR TU Delft, The Netherlands

Metal halide lamps between 1 and 10 g in a centrifuge

W.W. Stoffels, [A.J. Flikweert](#), T. Nimalasuriya and G.M.W. Kroesen, Symposium Technology for Artificial Gravity and Microgravity Simulation (10–12 December 2007), ESA, Noordwijk, The Netherlands

Imaging Laser Absorption Spectroscopy of MH lamp under hyper-gravity (1–10g)

A.J. Flikweert, Ruhr Universität Bochum, Allgemeine Elektrotechnik und Plasmatechnik, Research group of Prof. Awakowicz (13 June 2007), Bochum, Germany

2D laser absorption spectroscopy under hyper-gravity (1–10g) of the metal-halide lamp
A.J. Flikweert, T. Nimalasuriya, G.M.W. Kroesen and W.W. Stoffels, 7th Workshop on Frontiers in Low Temperature Plasma Diagnostics (1–5 April 2007), Beverly, United Kingdom

2D laser absorption spectroscopy of the metal-halide lamp in a centrifuge (1–10g)
A.J. Flikweert, T. Nimalasuriya, G.M.W. Kroesen and W.W. Stoffels, 19th Symposium Plasma Physics & Radiation Technology (6–8 March 2007), Lunteren, The Netherlands

Axial segregation in high intensity discharge lamps under varying gravity conditions
A.J. Flikweert, T. Nimalasuriya, M. Haverlag, G.M.W. Kroesen and W.W. Stoffels, 14th Gaseous Electronics Meeting (5–9 February 2006), Murrumarang Resort, Batemans Bay, Australia

Axial and radial segregation in high intensity discharge lamps measured by laser absorption spectroscopy
A.J. Flikweert, COST-Meeting "plasma light generation" 27th International Conference on Phenomena in Ionized Gases, XXVII ICPIG (17 July 2005), Veldhoven, The Netherlands

Axial segregation in metal halide lamps under varying gravity conditions
A.J. Flikweert, T. Nimalasuriya, M. Haverlag, G.M.W. Kroesen and W.W. Stoffels, 8th Euregional WELT-PP, Workshop on the Exploration of Low Temperature Plasma Physics (24–25 November 2005), Kerkrade, The Netherlands

Conference posters

The metal-halide lamp investigated in the centrifuge (1–10g) by emission and Imaging Laser Absorption Spectroscopy
A.J. Flikweert, L. Navarro, T. Nimalasuriya, G.M.W. Kroesen and W.W. Stoffels, 29th Symposium Plasma Physics & Radiation Technology (4–5 March 2008), Lunteren, The Netherlands

3D dysprosium density in the metal-halide lamp measured by emission and laser absorption spectroscopy in a centrifuge at 1–10g
A.J. Flikweert, T. Nimalasuriya, G.M. Thubé, G.M.W. Kroesen and W.W. Stoffels, 11th International Symposium on the Science and Technology of Light Sources (20–24 May 2007), Shanghai, China

Fluctuating magnetic field measurements in a horizontal helicon double layer system
A.J. Flikweert, M.D. West, A. Aanesland, C. Charles and R.W. Boswell, 9th Euregional Workshop on the Exploration of Low Temperature Plasma Physics (23–24 November 2006), Kerkrade, The Netherlands

Search for molecules in the metal halide lamp by emission spectroscopy
G.F.C. Saget, A.J. Flikweert, T. Nimalasuriya and W.W. Stoffels, 9th Euregional Workshop on the Exploration of Low Temperature Plasma Physics (23–24 November 2006), Kerkrade, The Netherlands

The effect of micro- and hyper-gravity (0-10 g) on axial segregation in metal-halide lamps
A.J. Flikweert, T. Nimalasuriya, M. van Kemenade, G.M. Thubé, M. Haverlag, G.M.W. Kroesen and W.W. Stoffels, ESCAMPIG XVIII (12–16 July, 2006), Lecce, Italy

Axial segregation in metal-halide lamps under varying gravity conditions (0–10g)
A.J. Flikweert, M. van Kemenade, T. Nimalasuriya, M. Haverlag, G.M.W. Kroesen and W.W. Stoffels, 18th Symposium Plasma Physics & Radiation Technology (22–23 March 2006), Lunteren, The Netherlands

Axial segregation in high intensity discharge lamps measured by laser absorption spectroscopy
A.J. Flikweert, T. Nimalasuriya, C.H.J.M. Groothuis, M. Haverlag, G.M.W. Kroesen and W.W. Stoffels, 27th International Conference on Phenomena in Ionized Gases, XXVII ICPIG (17–22 July 2005), Veldhoven, The Netherlands

Axial and radial segregation in metal halide lamps measured by absorption spectroscopy
A.J. Flikweert, T. Nimalasuriya, W.W. Stoffels, M. Haverlag and G.M.W. Kroesen, Symposium Plasma Physics & Radiation Technology (1–2 March 2005), Lunteren, The Netherlands

Studying axial segregation in high intensity discharge lamps by means of absorption spectroscopy
A.J. Flikweert, T. Nimalasuriya, W.W. Stoffels, M. van Kemenade, J. Beckers, C.H.J.M. Groothuis, M. Haverlag and G.M.W. Kroesen, 7th Eurogional WELT-PP (25–26 November 2004), Kerkrade, The Netherlands

Non-thermal atmospheric discharge for biomedical purposes
A.J. Flikweert, E. Stoffels, W.W. Stoffels, E.J. Ridderhof, R.P. Dahiya and G.M.W. Kroesen, 4th Euregional Welt-PP, Workshop on the Exploration of Low Temperature Plasma Physics (November 2001), Kerkrade, The Netherlands

Orals and presentations, co-author

Competition between convection and diffusion in metal halide lamps

M.L. Beks, A.J. Flikweert and J.J.A.M. van der Mullen, 29th Symposium Plasma Physics & Radiation Technology (4–5 March 2008), Lunteren, The Netherlands, Oral

Transport phenomena in metal-halide lamps, a poly-diagnostic study

T. Nimalasuriya, A.J. Flikweert, M.L. Beks, W.W. Stoffels, M. Haverlag, G.M.W. Kroesen and J.J.A.M. van der Mullen, 29th Symposium Plasma Physics & Radiation Technology (4–5 March 2008), Lunteren, The Netherlands, Conference Poster

Metal Halide Lamps from 0 to 10 g

W.W. Stoffels, A.J. Flikweert, T. Nimalasuriya, M.L. Beks, A.F. Meunier, J.J.A.M. van der Mullen, M. Haverlag and G.M.W. Kroesen, 18th International Symposium on Plasma Chemistry (26–31 August 2007), Kyoto, Japan, Conference Poster

X-Ray Induced Fluorescence Measurement of the Additive and Hg Densities in a Metal-Halide Lamp

T. Nimalasuriya, J.J. Curry, C.J. Sansonetti, E.J. Ridderhof, A.J. Flikweert, W.W. Stoffels, M. Haverlag and J.J.A.M. van der Mullen, 11th International Symposium on the Science and Technology of Light Sources (20–24 May 2007), Shanghai, China, Conference Poster

Simulating Metal Halide Lamps Under Varying Accelerational Conditions With Plasimo

M.L. Beks, A.J. Flikweert, A. Hartgers and J.J.A.M. van der Mullen, 11th International Symposium on the Science and Technology of Light Sources (20–24 May 2007), Shanghai, China, Conference Poster

Color separation in metal halide lamps

W.W. Stoffels, T. Nimalasuriya, A.J. Flikweert, W.J.M. Brok, J.J.A.M. van der Mullen, G.M.W. Kroesen and M. Haverlag, 59th Annual Gaseous Electronics Conference (GEC) (10–13 October 2006), Columbus, United States, Conference Poster

Additive density distributions and temperature profiles of metal-halide lamps measured in the International Space Station and a centrifuge

T. Nimalasuriya, G.M. Thubé, A.J. Flikweert, W.W. Stoffels, M. Haverlag, G.M.W. Kroesen and J.J.A.M. van der Mullen, ESCAMPIG XVIII (12–16 July, 2006), Lecce, Italy, Conference Poster

Preliminary results from tests of the helicon double layer thruster in the ANU space simulation chamber

M.D. West, A.J. Flikweert, C. Charles and R.W. Boswell, 42nd AIAA/ASME/SAE/ASEE Joint Propulsion Conference & Exhibit (9–12 July 2006), Sacramento, California, United States, Conference Poster

A study of the coupling between the helicon pump wave and instabilities associated with a current-free double layer in Chi Kung

Å. Fredriksen, A. Aanesland, A.J. Flikweert, C. Charles and R.W. Boswell, 8th Asia-Pacific Conference on Plasma Science and Technology and 19th Symposium on Plasma Science for Materials (2–5 July 2006), Cairns, Australia, Oral

Segregation phenomena in metal-halide lamps

W.J.M. Brok, T. Nimalasuriya, A. Hartgers, J. van Dijk, M.L. Beks, A.J. Flikweert, G.M. Thubé, N.B.M. Papat, M. Haverlag, W.W. Stoffels, J.J.A.M. van der Mullen and G.M.W. Kroesen, 9th High Technology Plasma Process (HTPP) Conference (30 May 2006), St. Petersburg, Russian Federation, Invited talk

Optical and X-ray Diagnostics of Metal-Halide Lamps

T. Nimalasuriya, G.M. Thubé, N.B.M. Papat, J.J. Curry, C.J. Sansonetti, E.J. Ridderhof, A.J. Flikweert, W.W. Stoffels, M. Haverlag, G.M.W. Kroesen and J.J.A.M. van der Mullen, COST 529 Meeting (30 March–2 April 2006), Mierlo, The Netherlands, Invited Lecture

Additive Density distributions and Temperature profiles of Metal-Halide lamps from zero to hyper-gravity

T. Nimalasuriya, G.M. Thubé, A.J. Flikweert, W.W. Stoffels, M. Haverlag, G.M.W. Kroesen and J.J.A.M. van der Mullen, 18th Symposium Plasma Physics & Radiation Technology (22–23 March 2006), Lunteren, The Netherlands, Oral

Additive density distributions and temperature profiles of metal-halide lamps in the International Space Station

T. Nimalasuriya, A.J. Flikweert, W.W. Stoffels, M. Haverlag, G.M.W. Kroesen and J.J.A.M. van der Mullen, 8th Euregional WELT-PP, Workshop on the Exploration of Low Temperature Plasma Physics (24–25 November 2005), Kerkrade, The Netherlands, Oral

Absolute line intensity measurements of the density distribution of Dy in a metal-halide lamp

T. Nimalasuriya, N.B.M. Papat, A.J. Flikweert, W.W. Stoffels, M. Haverlag and J.J.A.M. van der Mullen, 27th International Conference on Phenomena in Ionized Gases, XXVII ICPIG (17–22 July 2005), Veldhoven, The Netherlands, Conference Poster

X-ray induced fluorescence measurement of the density distribution of Dy and Hg in a metal-halide lamp

T. Nimalasuriya, J.J. Curry, C.J. Sansonetti, E.J. Ridderhof, A.J. Flikweert, W.W. Stoffels, M. Haverlag and J.J.A.M. van der Mullen, 27th International Conference on Phenomena in Ionized Gases, XXVII ICPIG (17–22 July 2005), Veldhoven, The Netherlands, Conference Poster

Metal Halide Discharge Lamps under Micro Gravity Conditions

W.W. Stoffels, G.M.W. Kroesen, C.H.J.M. Groothuis, A.J. Flikweert, T. Nimalasuriya, M. van Kemenade, P. Kemps, M. Bax, F.H.J. van den Hout, D. van den Akker, G. Schiffelers, J. Beckers, E.C.A. Dekkers, J.G.M. Moerel, P. Brinkgeve, M. Haverlag, R. Keijser and A. Kuipers, 27th International Conference on Phenomena in Ionized Gases, XXVII ICPIG (17–22 July 2005), Veldhoven, The Netherlands, Conference Poster

Emission Spectroscopy of Metal Halide Lamps under Normal and Microgravity conditions

T. Nimalasuriya, A.J. Flikweert, W.W. Stoffels, M. Haverlag, G.M.W. Kroesen and J.J.A.M. van der Mullen, Symposium Plasma Physics & Radiation Technology (1–2 March 2005), Lunteren, The Netherlands, Conference Poster

Emission Spectroscopy of Metal Halide Lamps under Normal and Microgravity conditions

T. Nimalasuriya, A.J. Flikweert, W.W. Stoffels, M. Haverlag, G.M.W. Kroesen and J.J.A.M. van der Mullen, 7th Eurogional WELT-PP (25–26 November 2004), Kerkrade, The Netherlands, Conference Poster

Miscellaneous

Brochure of The Helicon Double Layer Thruster

SP3 group members, The Australian National University, Research School of Physical Sciences & Engineering (2006), Canberra, Australia

Curriculum Vitae

17 July 1980

Born in Gouda, The Netherlands.

1992 – 1998

VWO (Atheneum) Dr. Knippenbergcollege, Helmond, The Netherlands.

1998 – 2004

M.Sc. in Applied Physics at Eindhoven University of Technology, The Netherlands.

- 2003–2004, Graduation project (1 year): Akzo Nobel Chemicals in Arnhem NL, dr.ir. W.M.M. Kessels and prof.dr.ir. M.C.M. van de Sanden (Plasma & Materials Processing, TU/e), dr. E.A.G. Hamers (CSO, Akzo Nobel Chemicals; at present: Helianthos b.v.). Subject: *Designing a contactless probe for optimization of flexible solar cells by measuring electrical parameters in-situ.*
- 2002, External traineeship (3 months): RWTH-Aachen (Germany), Magnetic Resonance Center MARC (prof.dr.dr.h.c. B. Blümich). Subject: *Investigating Rubber Samples with the NMR-MOUSE (R) and Bruker Spectrometers.*
- 2001–2002, Internal traineeship (9 weeks), EPG group (TU/e, Applied Physics), dr.ir. E. Stoffels. Subject: *Plasma needle for medical treatment.*

Several courses about sustainable energy and emphasis on plasma physics (internal traineeship and master's project).

2004 – 2008

PhD study at Eindhoven University of Technology, Elementary Processes in Gas Discharges group, department of Applied Physics. Subject: *Spectroscopy on Metal-Halide Lamps under Varying Gravity Conditions*, supervised by dr.ir. W.W. Stoffels, prof.dr.ir. G.M.W. Kroesen and prof.dr.ir. M. Haverlag.

-
- Traineeship (2006, 3 months) at Space Plasmas & Plasma Propulsion Group, Australian National University, Canberra (Australia), supervisors dr. C. Charles and prof.dr. R.W. Boswell. Subject: *Helicon Double Layer Thruster*.

